

Copernicus Global Land Operations

“Vegetation and Energy”

”CGLOPS-1”

Framework Service Contract N° 199494 (JRC)

SCIENTIFIC QUALITY EVALUATION

CROSS-CUTTING CONSISTENCY

JANUARY - DECEMBER 2018

ISSUE I1.00

Organization name of lead contractor for this deliverable: Meteo-France

Book Captain: Jean-Christophe Calvet (Meteo-France)
Contributing authors: Clément Albergel (Meteo-France)
Bertrand Bonan (Meteo-France)
Catherine Meurey (Meteo-France)
Yonjung Zheng (Meteo-France)

Dissemination Level		
PU	Public	X
PP	Restricted to other programme participants (including the Commission Services)	
RE	Restricted to a group specified by the consortium (including the Commission Services)	
CO	Confidential, only for members of the consortium (including the Commission Services)	

DOCUMENT RELEASE SHEET

Book Captain:	J.-C. Calvet	Date: 13.03.2019	Sign. 
Approval:	R. Lacaze	Date: 28.03.2019	Sign. 
Endorsement:	M. Cherlet	Date:	Sign.
Distribution:	Public		

CHANGE RECORD

Issue/Revision	Date	Page(s)	Description of Change	Release
	13.03.2019	All	Final version	11.00

TABLE OF CONTENT

<i>Executive Summary</i>	18
1 Background	20
1.1 Scope and Objectives	20
1.2 Content of the Document	20
1.3 Related Documents	20
1.3.1 Applicable documents	20
1.3.2 Input documents	20
2 Methods	22
2.1 LDAS-Monde	22
2.2 Input products	23
2.3 Evaluation Metrics	25
2.3.1 Scores	25
2.3.2 Increments	26
3 Results at a global scale	28
4 Results for LAI V1	32
5 Results for FAPAR V1	42
6 Results for Surface Albedo	51
7 Results for SWI-001	60
8 Results for LST	78
9 LDAS statistics	105
9.1 Increments and impacts of the assimilation on water and carbon fluxes	105
9.2 Transition between SPOT-VGT and PROBA-V	116
9.3 LAI Version 1 (GEOV1) vs. LAI Version 2 (GEOV2)	120
9.4 Accuracy assessment	122
9.5 Number of observations	127
10 Conclusions	130
11 References	132

LIST OF FIGURES

Figure 1: Mean observed LAI for 2010-2018 (top) at a global scale, model open-loop vs. observation RMSD (middle), analysis vs. observation RMSD (bottom).29

Figure 2: Continental potential hot spots for droughts and heat waves at a global scale. Regions considered in this report affected by severe conditions in 2018 are indicated: Western Europe, and the Murray-Darling basin in Australia.30

Figure 3: Mean observed monthly (left) SSM and (right) LAI values in 2018 with respect to the minimum, mean and maximum values from 2010 to 2018 over (top) Western Europe (“WEUR”) and (bottom) the Murray-Darling basin (“MUDA”).31

Figure 4: Monthly average values of LAI over Western Europe at 0.25° spatial resolution from January (top) to June 2018 (bottom). From left to right: model, satellite product, analysis, analysis-model difference. The latter shows the impact of assimilating LAI and SWI-001 on the simulated LAI. The color scale range of LAI values is 0 to 4 m²m⁻².32

Figure 5: Monthly average values of LAI over Western Europe at 0.25° spatial resolution July (top) to December 2018 (bottom). From left to right: model, satellite product, analysis, analysis-model difference. The latter shows the impact of assimilating LAI and SWI-001 on the simulated LAI. The color scale range of LAI values is 0 to 4 m²m⁻².33

Figure 6: Monthly average values of LAI over the Murray-Darling basin at 0.25° spatial resolution from January (top) to June 2018 (bottom). From left to right: model, satellite product, analysis, analysis-model difference. The latter shows the impact of assimilating LAI and SWI-001 on the simulated LAI. The color scale range of LAI values is 0 to 4 m²m⁻².34

Figure 7: Monthly average values of LAI over the Murray-Darling basin at 0.25° spatial resolution from July (top) to December 2018 (bottom). From left to right: model, satellite product, analysis, analysis-model difference. The latter shows the impact of assimilating LAI and SWI-001 on the simulated LAI. The color scale range of LAI values is 0 to 4 m²m⁻².35

Figure 8: Monthly average values over Western Europe of LAI (top) and root-zone soil moisture (bottom) from 1 January 2010 to 31 December 2018: model (blue line), satellite product (green circles), analysis (red line). Analysis-Model differences show the impact of assimilating LAI and SWI-001 on the simulated LAI and root-zone soil moisture.36

Figure 9: Monthly average values over the Murray-Darling basin of LAI (top) and root-zone soil moisture (bottom) from 1 January 2010 to 31 December 2018: model (blue line), satellite product (green circles), analysis (red line). Analysis-Model differences show the impact of assimilating LAI and SWI-001 on the simulated LAI and root-zone soil moisture.37

Figure 10: Monthly LAI scores of the model (blue) and analysis (red) when compared to the observations over Western Europe at 0.25° spatial resolution: from 2010 to 2017 (dashed lines), with N ranging from 11,434 in January to 30,739 in April; and for 2018 (solid lines), with N ranging from 250 in December to 3,981 in July. The monthly N values are indicated in the legend Table. Analysis-Model differences show the impact of assimilating LAI and SWI-001 on the simulated LAI. Shaded areas are between minimum and maximum score values recorded from 2010 to 2017.38

Figure 11: Monthly LAI scores of the model (blue) and analysis (red) when compared to the observations over the Murray-Darling basin at 0.25° spatial resolution: from 2010 to 2017 (dashed lines), with N ranging from 41,535 in July to 41,681 in November; and for 2018 (solid lines), with N ranging from 3,474 in December to 5,211. The monthly N values are indicated in the legend Table. Analysis-Model differences show the impact of assimilating LAI and SWI-001 on the simulated LAI. Shaded areas are between minimum and maximum score values recorded from 2010 to 2017.39

Figure 12: Monthly average values of FAPAR over Western Europe at 0.25° spatial resolution from January (top) to June 2018 (bottom). From left to right: model, satellite product, analysis, analysis-model difference. The latter shows the impact of assimilating LAI and SWI-001 on the simulated FAPAR. The color scale range of FAPAR values is 0 to 1.0.....42

Figure 13: Monthly average values of FAPAR over Western Europe at 0.25° spatial resolution July (top) to December 2018 (bottom). From left to right: model, satellite product, analysis, analysis-model difference. The latter shows the impact of assimilating LAI and SWI-001 on the simulated FAPAR. The color scale range of FAPAR values is 0 to 1.0.43

Figure 14: Monthly average values of FAPAR over the Murray-Darling basin at 0.25° resolution January (top) to June 2018 (bottom). From left to right: model, satellite product, analysis, analysis-model difference. The latter shows the impact of assimilating LAI and SWI-001 on the simulated FAPAR. The color scale range of FAPAR values is 0 to 1.0.....44

Figure 15: Monthly average values of FAPAR over the Murray-Darling basin at 0.25° resolution July (top) to December 2018 (bottom). From left to right: model, satellite product, analysis, analysis-model difference. The latter shows the impact of assimilating LAI and SWI-001 on the simulated FAPAR. The color scale range of FAPAR values is 0 to 1.045

Figure 16: Monthly average values of FAPAR over Western Europe (top) from 2010 to 2018, the Murray-Darling basin (bottom) from 2010 to 2018: model (blue line), satellite product (green circles), analysis (red line). Analysis-Model differences show the impact of assimilating LAI and SWI-001 on the simulated FAPAR.46

Figure 17: Monthly FAPAR scores of the model (blue) and analysis (red) when compared to the observations over Western Europe at a 0.25° spatial resolution: from 2010 to 2017 (dashed lines), with N ranging from 11,450 in January to 30,745 in May; and for 2018 (solid lines), with N ranging from 256 in December to 3,983 in May. The monthly N values are indicated in the legend Table. Analysis-Model differences show the impact of assimilating LAI and SWI-001 on the simulated

FAPAR. Shaded areas are between minimum and maximum score values recorded from 2010 to 2017.47

Figure 18: Monthly FAPAR scores of the model (blue) and analysis (red) when compared to the observations over the Murray-Darling basin at 0.25° spatial resolution: from 2010 to 2017 (dashed lines), with N ranging from 41,537 in July to 41,682 in November; and for 2018 (solid lines), with N ranging from 5,093 in July to 5,211. The monthly N values are indicated in the legend Table. Analysis-Model differences show the impact of assimilating LAI and SWI-001 on the simulated FAPAR. Shaded areas are between minimum and maximum score values recorded from 2010 to 2017.48

Figure 19: Monthly average values of Surface Albedo over Western Europe at 0.25° spatial resolution from January (top) to June 2018 (bottom). From left to right: model, satellite product, analysis, analysis-model difference. The latter shows the impact of assimilating LAI and SWI-001 on the simulated SA. The color scale range of SA values is 0 to 0.5.51

Figure 20: Monthly average values of Surface Albedo over Western Europe at 0.25° spatial resolution from July (top) to December 2018 (bottom). From left to right: model, satellite product, analysis, analysis-model difference. The latter shows the impact of assimilating LAI and SWI-001 on the simulated SA. The color scale range of SA values is 0 to 0.5.52

Figure 21: Monthly average values of Surface albedo over the Murray-Darling basin at 0.25° spatial resolution from January (top) to June 2018 (bottom). From left to right: model, satellite product, analysis, analysis-model difference. The latter shows the impact of assimilating LAI and SWI-001 on the simulated SA. The color scale range of SA values is 0 to 0.5.53

Figure 22: Monthly average values of Surface albedo over the Murray-Darling basin at 0.25° spatial resolution from July (top) to December 2018 (bottom). From left to right: model, satellite product, analysis, analysis-model difference. The latter shows the impact of assimilating LAI and SWI-001 on the simulated SA. The color scale range of SA values is 0 to 0.5.54

Figure 23: Monthly average values of SA over Western Europe (top) from 2010 to 2018, the Murray-Darling basin (bottom) from 2010 to 2018: model (blue line), satellite product (green circles), analysis (red line). Analysis-Model differences show the impact of assimilating LAI and SWI-001 on the simulated SA. (Note that spikes in Western Europe correspond to extensive snowfalls. In the analysis, the snow-free seasonal variability is triggered by changes in the fractional cover of crops related to LAI. Model and analysis curves are often superimposed).55

Figure 24: Monthly SA scores of the model (blue) and analysis (red) when compared to the observations over Western Europe at a 0.25° spatial resolution: from 2010 to 2017 (dashed lines), with N ranging from 7255 in January to 258,888 in April; and for January to December 2018 (solid lines), with N ranging from 55 in January to 3,472 in October. The monthly N values are indicated in the legend Table. Analysis-Model differences show the impact of assimilating LAI and SWI-001 on the simulated SA. (Note that model and analysis curves are often superimposed).56

Figure 25: Monthly SA scores of the model (blue) and analysis (red) when compared to the observations over the Murray-Darling basin at 0.25° spatial resolution: from 2010 to 2017 (dashed lines), with N ranging from 32,985 in December to 38,153 in April; and for January to December 2018 (solid lines), with N ranging from 3,472 in November to 4,797 in March. The monthly N values are indicated in the legend Table. Analysis-Model differences show the impact of assimilating LAI and SWI-001 on the simulated SA. (Note that model and analysis curves are often superimposed).57

Figure 26: Monthly average values of SSM over Western Europe at 0.25° spatial resolution from January (top) to June 2018 (bottom). From left to right: model, rescaled satellite product after CDF matching, analysis, analysis-model difference. The latter shows the impact of assimilating LAI and SWI-001 on the simulated SSM. The color scale range of SSM values is 0 to 0.4 m³m⁻³.60

Figure 27: Monthly average values of SSM over Western Europe at 0.25° spatial resolution from July (top) to December 2018 (bottom). From left to right: model, rescaled satellite product after CDF matching, analysis, analysis-model difference. The latter shows the impact of assimilating LAI and SWI-001 on the simulated SSM. The color scale range of SSM values is 0 to 0.4 m³m⁻³.61

Figure 28: Monthly average values of SSM over the Murray-Darling basin at 0.25° spatial resolution from January (top) to June 2018 (bottom). From left to right: model, rescaled satellite product after CDF matching, analysis, analysis-model difference. The latter shows the impact of assimilating LAI and SWI-001 on the simulated SSM. The color scale range of SSM values is 0 to 0.4 m³m⁻³.62

Figure 29: Monthly average values of SSM over the Murray-Darling basin at 0.25° spatial resolution from July (top) to December 2018 (bottom). From left to right: model, rescaled satellite product after CDF matching, analysis, analysis-model difference. The latter shows the impact of assimilating LAI and SWI-001 on the simulated SSM. The color scale range of SSM values is 0 to 0.4 m³m⁻³.63

Figure 30: Monthly correlation maps between the rescaled SWI-001 product time series after CDF matching and the modeled SSM (left), and the analyzed SSM (middle) over Western Europe at 0.25° spatial resolution from January (top) to June 2018 (bottom). Analysis-Model differences show the impact of assimilating LAI and SWI-001 on the simulated SSM. The color scale range of R values is -1.0 to 1.0. Areas with missing data are left blank.64

Figure 31: Monthly correlation maps between the rescaled SWI-001 product time series after CDF matching and the modeled SSM (left), and the analyzed SSM (middle) over Western Europe at 0.25° spatial resolution from July (top) to December 2018 (bottom). Analysis-Model differences show the impact of assimilating LAI and SWI-001 on the simulated SSM. The color scale range of R values is -1.0 to 1.0.65

Figure 32: Monthly correlation maps between the rescaled SWI-001 product time series after CDF matching and the modeled SSM (left), and the analyzed SSM (middle) over the Murray-Darling basin at 0.25° spatial resolution from January (top) to June 2018 (bottom). Analysis-Model differences show the impact of assimilating LAI and SWI-001 on the simulated SSM. The color scale range of R values is -1.0 to 1.0.66

Figure 33: Monthly correlation maps between the rescaled SWI-001 product time series after CDF matching and the modeled SSM (left), and the analyzed SSM (middle) over the Murray-Darling basin at 0.25° spatial resolution from July (top) to December 2018 (bottom). Analysis-Model differences show the impact of assimilating LAI and SWI-001 on the simulated SSM. The color scale range of R values is -1.0 to 1.0.67

Figure 34: Yearly correlation maps between the rescaled SWI-001 product time series after CDF matching and the modeled SSM (left), and the analyzed SSM (middle) over Western Europe at 0.25° resolution from 2010 to 2018. Analysis-Model differences show the impact of assimilating LAI and SWI-001 on the simulated SSM. The color scale range of R values is -1.0 to 1.0.68

Figure 35: Yearly correlation maps between the rescaled SWI-001 product time series after CDF matching and the modeled SSM (left), and the analyzed SSM (middle) over the Murray-Darling basin at 0.25° resolution from 2010 to 2018. Analysis-Model differences show the impact of assimilating LAI and SWI-001 on the simulated SSM. The color scale range of R values is -1.0 to 1.0.69

Figure 36: Monthly average values of SSM over Western Europe from 2010 to 2018. Top panel: original SWI-001 (red), model SSM used for CDF-matching (blue), rescaled SWI-001 product (green). Bottom panel: model (blue, same as on the top graph), rescaled SWI-001 observations (green), analysis (red). Analysis-Model differences show the impact of assimilating LAI and SWI-001 on the simulated SSM.70

Figure 37: Monthly average values of SSM over the Murray-Darling basin from 2010 to 2018. Top panel: original SWI-001 (red), model SSM used for CDF-matching (blue), rescaled SWI-001 product (green). Bottom panel: model (blue, same as on the top graph), rescaled SWI-001 observations (green), analysis (red). Analysis-Model differences show the impact of assimilating LAI and SWI-001 on the simulated SSM.71

Figure 38: Monthly SSM scores of the model (blue) and analysis (red) when compared to the rescaled SWI-001 over Western Europe at 0.25° spatial resolution: for all data from 2010 to 2017 (dashed lines), with N ranging from 39,163 in January to 2,448,876 in August, and for data in 2018 (solid lines), with N ranging from 1,530 in February to 41,868 in July. The monthly N values are indicated in the legend Table. Analysis-Model differences show the impact of assimilating LAI and SWI-001 on the simulated SSM. Shaded areas are between minimum and maximum score values recorded from 2010 to 2017.72

Figure 39: Monthly scores of the model (blue) and analysis (red) when compared to the rescaled SWI-001 over the Murray-Darling basin at 0.25° spatial resolution: for all data from 2010 to 2017 (dashed lines), with N ranging from 118,513 in February to 169,957 in November, and for data in 2018 (solid lines), with N ranging from 39,454 in February to 44,720 in October. The monthly N values are indicated in the legend Table. Analysis-Model differences show the impact of assimilating LAI and SWI-001 on the simulated SSM. Shaded areas are between minimum and maximum score values recorded from 2010 to 2017.73

Figure 40: Annual scores of the model (blue) and analysis (red) when compared to the rescaled SWI-001 over Western Europe at 0.25° spatial resolution, with N ranging from 164,456 in 2010 to 355,061 in 2018. The yearly N values are indicated in the legend Table. Analysis-Model differences show the impact of assimilating LAI and SWI-001 on the simulated SSM.....74

Figure 41: Annual scores of the model (blue) and analysis (red) when compared to the rescaled SWI-001 over the Murray-Darling basin at 0.25° spatial resolution, with N ranging from 82,588 in 2014 to 511,044 in 2018. The yearly N values are indicated in the legend Table. Analysis-Model differences show the impact of assimilating LAI and SWI-001 on the simulated SSM.75

Figure 42: Monthly average values of LST at 1200 UTC over Western Europe at 0.25° spatial resolution from January to June 2018. From left to right: model, satellite product, analysis, analysis-model difference. The latter shows the impact of assimilating LAI and SWI-001 on the simulated LST. The color scale range of LST values is -5 to 30 °C.78

Figure 43: Monthly average values of LST at 1200 UTC over Western Europe at 0.25° spatial resolution from July to December 2018. From left to right: model, satellite product, analysis, analysis-model difference. The latter shows the impact of assimilating LAI and SWI-001 on the simulated LST. The color scale range of LST values is -5 to 30 °C.79

Figure 44: Monthly average values of LST at 0600 UTC over Western Europe at 0.25° spatial resolution from January to June 2018. From left to right: model, satellite product, analysis, analysis-model difference. The latter shows the impact of assimilating LAI and SWI-001 on the simulated LST. The color scale range of LST values is -5 to 30 °C.80

Figure 45: Monthly average values of LST at 0600 UTC over Western Europe at 0.25° spatial resolution from July to December 2018. From left to right: model, satellite product, analysis, analysis-model difference. The latter shows the impact of assimilating LAI and SWI-001 on the simulated LST. The color scale range of LST values is -5 to 30 °C.81

Figure 46: Monthly average values of LST at 0300 UTC (~noon) over the Murray-Darling basin at 0.25° spatial resolution from January to June 2018: model (left), satellite (middle) product, and analysis (right). Analysis-Model differences show the impact of assimilating LAI and SWI-001 on the simulated LST. The color scale range of LST values is 0 to 60 °C.82

Figure 47: Monthly average values of LST at 0300 UTC (~noon) over the Murray-Darling basin at 0.25° spatial resolution from July to December 2018: model (left), satellite (middle) product, and analysis (right). Analysis-Model differences show the impact of assimilating LAI and SWI-001 on the simulated LST. The color scale range of LST values is 0 to 60 °C.83

Figure 48: Monthly average values of LST at 2100 UTC (~dawn) over the Murray-Darling basin at 0.25° spatial resolution from January to June 2018: model (left), satellite (middle) product, and analysis (right). Analysis-Model differences show the impact of assimilating LAI and SWI-001 on the simulated LST. The color scale range of LST values is 0 to 60 °C.84

Figure 49: Monthly average values of LST at 2100 UTC (~dawn) over the Murray-Darling basin at 0.25° spatial resolution from July to December 2018: model (left), satellite (middle) product, and analysis (right). Analysis-Model differences show the impact of assimilating LAI and SWI-001 on the simulated LST. The color scale range of LST values is 0 to 60 °C.85

Figure 50: Monthly bias for LST at 1200 UTC over Western Europe at 0.25° spatial resolution from January to December 2018. From left to right: model, analysis, analysis-model difference. The latter shows the impact of assimilating LAI and SWI-001 on the simulated LST. The color scale range of LST bias values is -7 to 7 °C.86

Figure 51: Monthly bias for LST at 0600 UTC over Western Europe at 0.25° spatial resolution from January to December 2018. From left to right: model, analysis, analysis-model difference. The latter shows the impact of assimilating LAI and SWI-001 on the simulated LST. The color scale range of LST bias values is -2.8 to 2.8 °C.87

Figure 52: Monthly bias for LST at 0300 UTC (~noon) over the Murray-Darling basin at 0.25° spatial resolution from January to December 2018. From left to right: model, analysis, analysis-model difference. The latter shows the impact of assimilating LAI and SWI-001 on the simulated LST. The color scale range of LST bias values is -12 to 12 °C.88

Figure 53: Monthly bias for LST at 2100 UTC (~dawn) over the Murray-Darling basin at 0.25° spatial resolution from January to December 2018. From left to right: model, analysis, analysis-model difference. The latter shows the impact of assimilating LAI and SWI-001 on the simulated LST. The color scale range of LST bias values is -4.7 to 4.7 °C.89

Figure 54: Monthly correlation for LST at 1200 UTC over Western Europe at 0.25° spatial resolution from January to December 2018. From left to right: model, analysis, analysis-model difference. The latter shows the impact of assimilating LAI and SWI-001 on the simulated LST.90

Figure 55: Monthly correlation for LST at 0600 UTC over Western Europe at 0.25° spatial resolution from January to December 2018. From left to right: model, analysis, analysis-model difference. The latter shows the impact of assimilating LAI and SWI-001 on the simulated LST.91

Figure 56: Monthly correlation for LST at 0300 UTC (~noon) over the Murray-Darling basin at 0.25° spatial resolution from January to December 2018. From left to right: model, analysis, analysis-model difference. The latter shows the impact of assimilating LAI and SWI-001 on the simulated LST.92

Figure 57: Monthly correlation for LST at 2100 UTC (~dawn) over the Murray-Darling basin at 0.25° spatial resolution from January to December 2018. From left to right: model, analysis, analysis-model difference. The latter shows the impact of assimilating LAI and SWI-001 on the simulated LST.93

Figure 58: Monthly LST scores at 1200 UTC of the model (blue) and analysis (red) when compared to observations over Western Europe at 0.25° spatial resolution: from 2010 to 2017 (dashed lines), with N ranging from 46,003 in December to 89,644 in March; and 2018 (solid lines), with N ranging from 3,518 in January to 15,793 in May. The monthly N values are indicated in the legend Table. Analysis-

Model differences show the impact of assimilating LAI and SWI-001 on the simulated LST. Shaded areas are between minimum and maximum score values recorded from 2010 to 2017.94

Figure 59: Monthly LST scores at 0600 UTC of the model (blue) and analysis (red) when compared to observations over Western Europe at 0.25° spatial resolution: from 2010 to 2017 (dashed lines), with N ranging from 65,939 in November to 121,511 in March; and 2018 (solid lines), with N ranging from 4,617 in January to 23,143 in July. The monthly N values are indicated in the legend Table. Analysis-Model differences show the impact of assimilating LAI and SWI-001 on the simulated LST. Shaded areas are between minimum and maximum score values recorded from 2010 to 2017.95

Figure 60: Monthly LST scores at 0300 UTC (~noon) of the model (blue) and analysis (red) when compared to observations over the Murray-Darling basin at 0.25° spatial resolution: from 2010 to 2017 (dashed lines), with N ranging from 238,774 in February to 328,607 in August; and 2018 (solid lines), with N ranging from 31,525 in January to 46,979 in July. The monthly N values are indicated in the legend Table. Analysis-Model differences show the impact of assimilating LAI and SWI-001 on the simulated LST. Shaded areas are between minimum and maximum score values recorded from 2010 to 2017.96

Figure 61: Monthly LST scores at 2100 UTC (~dawn) of the model (blue) and analysis (red) when compared to observations over the Murray-Darling basin at 0.25° spatial resolution: from 2010 to 2017 (dashed lines), with N ranging from 208,626 in November to 274,567 in August; and 2018 (solid lines), with N ranging from 30,402 in October to 43,894 in July. The monthly N values are indicated in the legend Table. Analysis-Model differences show the impact of assimilating LAI and SWI-001 on the simulated LST. Shaded areas are between minimum and maximum score values recorded from 2010 to 2017.97

Figure 62: LST 3-hourly bias of the analysis over Western Europe at 0.25° spatial resolution from January to June from 2010 to 2017 (green line) and for 2018 (blue line).98

Figure 63: LST 3-hourly bias of the analysis over Western Europe at 0.25° spatial resolution from July to December from 2010 to 2017 (green line) and for 2018 (blue line).99

Figure 64: LST 3-hourly bias of the analysis over the Murray-Darling basin at 0.25° spatial resolution from January to June from 2010 to 2017 (green line) and for 2018 (blue line). [Note that 0300 UTC is close to noon at these longitudes.] 100

Figure 65: LST 3-hourly bias of the analysis over the Murray-Darling basin at 0.25° spatial resolution from July to December from 2010 to 2017 (green line) and for 2018 (blue line). [Note that 0300 UTC is close to noon at these longitudes.] 101

Figure 66: Monthly maps over Western Europe from January to June of LAI (1st column), root-zone soil moisture (2nd column) increments: averages over 2010–2017 (left), and for 2018 (right). 105

Figure 67: Monthly maps over Western Europe from July to December of LAI (1st column), root-zone soil moisture (2nd column) increments: averages over 2010–2017 (left), and for 2018 (right). 106

Figure 68: Monthly maps over Western Europe from January to June of the differences (Analysis-Model) for evapotranspiration (ET, 1st column) and drainage fluxes (2nd column): averages over 2010–2017 (left), and for 2018 (right). 107

Figure 69: Monthly maps over Western Europe from July to December of the differences (Analysis-Model) for evapotranspiration (ET, 1st column) and drainage fluxes (2nd column): averages over 2010–2017 (left), and for 2018 (right). 108

Figure 70: Monthly maps over Western Europe from January to December of the differences (Analysis-Model) for NEE (1st column), GPP (2nd column) and Reco fluxes (3rd column): averages over 2010–2017 (left), and for 2018 (right). 109

Figure 71: Monthly maps over the Murray-Darling basin from January to June of LAI (1st column), root-zone soil moisture (2nd column) increments: averages over 2010–2017 (left), and for 2018 (right). 110

Figure 72: Monthly maps over the Murray-Darling basin from July to December of LAI (1st column), root-zone soil moisture (2nd column) increments: averages over 2010–2017 (left), and for 2018 (right). 111

Figure 73: Monthly maps over the Murray-Darling basin from January to June of the differences (Analysis-Model) for evapotranspiration (ET, 1st column) and drainage fluxes (2nd column): averages over 2010–2017 (left), and for 2018 (right). 112

Figure 74: Monthly maps over the Murray-Darling basin from July to December of the differences (Analysis-Model) for evapotranspiration (ET, 1st column) and drainage fluxes (2nd column): averages over 2010–2017 (left), and for 2018 (right). 113

Figure 75: Monthly maps over the Murray-Darling basin from January to December of the differences (Analysis-Model) for NEE (1st column), GPP (2nd column) and Reco fluxes (3rd column): averages over 2010–2017 (left), and for 2018 (right). 114

Figure 76: RZSM and LAI mean increments which result from the assimilation of both SWI-001 and LAI observations over Western Europe (top) from 2010 to 2018, over the Murray-Darling basin (bottom) from 2010 to 2018. 115

Figure 77: LAI scores for the time periods of SPOT-VGT observations over Western Europe (top) (2010-2013, dashed lines) and the Murray-Darling basin (bottom) (2010-2013, dashed lines) and of PROBA-V observations (2015-2018, solid lines). Model performances are in blue and analysis performances are in red w.r.t. the appropriate observations. [NB: 2014 was not considered since it was the year of transition between the two instruments]..... 118

Figure 78: SA scores for the time periods of SPOT-VGT observations over Western Europe (top) (2010-2013, dashed lines) and the Murray-Darling basin (bottom) (2010-2013, dashed lines) and of PROBA-V observations (2015-2018, solid lines). Model performances are in blue and analysis

performances are in red w.r.t. the appropriate observations. [NB: 2014 was not considered since it was the year of transition between the two instruments]..... 119

Figure 79: LAI GEOV2 vs. GEOV1 yearly RMSD score over Western Europe for each year from 2010 to 2018. Year 2018 is indicated...... 120

Figure 80: LAI GEOV2 vs. GEOV1 yearly RMSD score over the Murray-Darling basin for each year from 2010 to 2018. Year 2018 is indicated. 121

Figure 81: Relative analysis RMSD (RMSD divided by value) (top) and analysis RMSD (bottom) of LAI (left) and FAPAR (right) on average over Western Europe. Dashed red line indicates the target accuracies: $\max(20\%,0.5)$ for LAI and $\max(10\%,0.05)$ for FAPAR. Shaded areas indicate 1 standard deviation...... 123

Figure 82: Relative analysis RMSD (RMSD divided by value) (top) and analysis RMSD (bottom) of LAI (left) and FAPAR (right) on average over the Murray-Darling basin. Dashed red line indicates the target accuracies: $\max(20\%,0.5)$ for LAI and $\max(10\%,0.05)$ for FAPAR. Shaded areas indicate 1 standard deviation. 124

Figure 83: Maps over Western Europe showing (in green) where GCOS accuracy requirements could be met (LAI: $\max(20\%,0.5)$, FAPAR: $\max(10\%,0.05)$) or may have not be met (in red) for 2018. ... 125

Figure 84: Maps over the Murray-Darling basin showing (in green) where GCOS accuracy requirements could be met (LAI: $\max(20\%,0.5)$, FAPAR: $\max(10\%,0.05)$) or may have not be met (in red) for 2018. 126

Figure 85: Annual number of SWI-001 observations available over Western Europe (only METOP-A until July 20, 2015; after July 21, 2015 both METOP-A and B are used) 128

Figure 86: Annual number of SWI-001 observations available over the Murray-Darling basin (only METOP-A until July 20, 2015; after July 21, 2015 both METOP-A and B are used) 129

LIST OF TABLES

<i>Table 1: Surface State Flag values of the SWI product.....</i>	24
<i>Table 2: Continental hot spots for droughts and heat waves and number of monthly low SSM and LAI records in 2018 with respect to the 2010-2018 period</i>	30
<i>Table 3: Model and analysis LAI scores from 2010 to 2017 and for 2018 over Western Europe (top), from 2010 to 2017 and for 2018 over the Murray-Darling basin (bottom). Analysis-Model differences show the impact of assimilating LAI and SWI-001 on the simulated LAI. Mean bias, RMSD and SDD are in m^2m^{-2}.....</i>	40
<i>Table 4: Model and analysis FAPAR scores from 2010 to 2017 and for 2018 over Western Europe (top), from 2010 to 2017 and for 2018 over the Murray-Darling basin (bottom). Analysis-Model differences show the impact of assimilating LAI and SWI-001 on the simulated FAPAR.....</i>	49
<i>Table 5: Model and analysis SA scores from 2010 to 2017 and for 2018 over Western Europe (top), the Murray-Darling basin (bottom). Analysis-Model differences show the impact of assimilating LAI and SWI-001 on the simulated SA.</i>	58
<i>Table 6: Annual score values of the model and analysis w.r.t. the rescaled SWI-001 over Western Europe (top) from 2010 to 2018, the Murray-Darling basin (bottom) from 2010 to 2018. Model-analysis differences show the impact of assimilating LAI and SWI-001 on the simulated SSM.</i>	76
<i>Table 7: LST annual scores of the model and analysis w.r.t. the LST observations at 1200 UTC (top) and 0600 UTC (bottom) over Western Europe. Analysis-Model differences show the impact of assimilating LAI and SWI-001 on the simulated LST. The relatively unbiased average LST at 0600 UTC hides marked spatial and seasonal patterns (Figure 51 and Figure 59).</i>	102
<i>Table 8: LST annual scores of the model and analysis w.r.t. the LST observations at 0300 UTC (~noon) (top) and at 2100 UTC (~dawn) (bottom) over the Murray-Darling basin. Analysis-Model differences show the impact of assimilating LAI and SWI-001 on the simulated LST. The relatively unbiased average LST at 0600 UTC hides marked spatial and seasonal patterns (Figure 53 and Figure 61).</i>	103

ACRONYM LIST

ALBH	Bi-hemispherical albedo
ASCAT	Advanced Scatterometer
C3S	Copernicus Climate Change Service
CCR	Cross-cutting Consistency Report
CDF	Cumulative Distribution Function
CGLS	Copernicus Global Land Service
ECMWF	European Centre for Medium-Range Weather Forecasts
ERA	ECMWF Reanalysis
ET	Evapotranspiration
FAPAR	Fraction of Absorbed Photosynthetically Active Radiation
GCOS	Global Climate Observing System
GPP	Gross Primary Production (photosynthesis)
ISBA	Interactions between Soil, Biosphere, and Atmosphere
LAI	Leaf Area Index
LDAS	Land Data Assimilation System
LSM	Land Surface Model
LST	Land Surface Temperature
MODIS	Moderate Resolution Imaging Spectroradiometer
NEE	Net Ecosystem Exchange of CO ₂
PROBA-V	Project for On-Board Autonomy – Vegetation
QF	Quality flag
R	Pearson correlation coefficient
Reco	Ecocystem respiration
RMSD	Root Means Square Difference
RZSM	Root Zone Soil Moisture
SA	Surface Albedo
SDD	Standard Deviation of Differences
SSM	Surface Soil Moisture
SPOT	Satellite Pour l'Observation de la Terre
SQE	Scientific Quality Evaluation
SSF	Surface State Flag
SURFEX	Surface Externalisée (externalized surface models)
SWI	Soil Water Index
UTC	Universal Time Coordinated
VGT	Vegetation sensor on SPOT satellite

EXECUTIVE SUMMARY

The Copernicus Global Land Service (CGLS) is earmarked as a component of the Land service to operate “a *multi-purpose service component*” that provides a series of biogeophysical products on the status and evolution of land surface at global scale. Production and delivery of the parameters take place in a timely manner and are complemented by the constitution of long-term time series.

The most advanced indirect validation technique consists in integrating the products into a land surface model (LSM) using a data assimilation scheme. The obtained reanalysis accounts for the synergies of the various upstream products and provides statistics which can be used to monitor the quality of the assimilated observations.

Meteo-France develops the ISBA-A-gs generic LSM, able to represent the diurnal cycle of the surface fluxes together with the seasonal, inter-annual and decadal variability of the vegetation biomass. The LSM is embedded in the SURFEX modeling platform together with a simplified extended Kalman filter. These tools form a Land Data Assimilation System (LDAS). The current version of the LDAS (LDAS-Monde) is able to assimilate SPOT-VGT and PROBA-V Leaf Area Index (LAI) and ASCAT surface soil moisture (SSM) satellite products at a global scale at a spatial resolution of at least $0.25^\circ \times 0.25^\circ$. This permits the active monitoring of LAI and SSM variables. A passive monitoring of Surface Albedo (SA), Fraction of Absorbed Photosynthetically Active Radiation (FAPAR) and Land Surface Temperature (LST) is performed (i.e., the simulated values are compared with the satellite products), as these quantities are not assimilated yet. The LDAS generates statistics whose trends can be analyzed in order to detect possible drifts in the quality of the products: (1) for LAI and SSM, metrics derived from the active monitoring (i.e. assimilation) such as innovations (observations vs. model), residuals (observations vs. analysis), and increments (analysis vs. model); (2) for SA, FAPAR and LST, metrics derived from the passive monitoring. In both cases, the Pearson correlation coefficient (R), the root mean square difference (RMSD), the standard deviation of difference (SDD), and mean bias skill scores are used.

In this report, results are presented for the **January-December 2018** period over Western Europe and over the Murray-Darling basin. Note that the last data from SPOT-VGT were used on 13th May 2014. After this date, new LAI / FAPAR / SA products from PROBA-V are used.

For **LAI**, over both Western Europe and the Murray-Darling basin, the scores tend to present better values during the dry spells of 2018 than during previous years from 2010 to 2017. The RMSD scores of consolidated estimate of LAI Version 2 and LAI Version 1 are

comparable in 2018. The impact on analyzed LAI of transitioning from SPOT-VGT to PROBA-V is small.

For **FAPAR**, over both Western Europe and the Murray-Darling basin, the scores tend to present slightly better values during the dry spells of 2018 than during previous years from 2010 to 2017. Overall conclusions for FAPAR are similar to those for LAI.

For **SA**, a striking result is that a very large increase in the mean bias value is observed after the transition from SPOT-VGT to PROBA-V, of about 0.02 and 0.04 for Western Europe and for the Murray-Darling basin, respectively. There is a clear discontinuity in the SA time series, not observed for LAI nor for FAPAR.

For **SWI-001**, the impact of the seasonal SSM CDF-matching performed prior the assimilation is particularly striking for Western Europe. Without a seasonal CDF-matching, the original SSM information would be misleading over Western Europe.

For **LST**, the model tends to underestimate LST at daytime and to overestimate LST at dawn. Over the Murray-Darling basin, the mean yearly bias is about -8°C in 2018 (a dry year), against -4°C in 2010 (a wet year). This result shows that daytime LST biases are more pronounced in dry conditions. Possible causes of the spatial, diurnal and seasonal patterns of the LST bias are hot-spot phenomenon (more sunlit than shaded elements are seen by the satellite), biases in the incoming solar and infrared radiation data used to force the model.

LDAS analyses were also used to assess the accuracy of LAI and FAPAR observations, with respect to GCOS requirements. It is showed that small values of LAI observations tend to meet the GCOS requirements more often than large values of LAI observations and of FAPAR observations, for both Western Europe and the Murray-Darling basin. Overall, low FAPAR values present more uncertainties than low LAI values.

1 BACKGROUND

1.1 SCOPE AND OBJECTIVES

The objective of this report is to present an evaluation of the consistency of LAI, SSM (SWI-001), SA, FAPAR and LST over Western Europe and the Murray-Darling basin for the **January-December 2018** period, with respect to past years (2010-2017). This task was performed by Meteo-France, using the LDAS-Monde tool (Albergel et al., 2017).

1.2 CONTENT OF THE DOCUMENT

The cross-cutting validation method is described in Chapter 2 together with the input products. Chapter 3 presents results at a global scale and the selection of two regions for this report. Chapters 4 to 8 present the results for LAI V1, FAPAR V1, SA, SWI-001, and LST, respectively. Chapter 9 presents the LDAS statistics from **January to December 2018**, vs. past periods of time (2010-2017), together with the impact on LAI and SA scores of switching from SPOT-VGT to PROBA-V in 2014, and with a comparison between consolidated estimate (RT6) of Version 2 LAI and the NRT Version 1 LAI. Chapter 10 summarizes the main conclusions. The references are listed in Chapter 11.

1.3 RELATED DOCUMENTS

1.3.1 *Applicable documents*

AD1: Annex I – Technical Specifications JRC/IPR/2015/H.5/0026/OC to Contract Notice 2015/S 151-277962 of 7th August 2015

AD2: Appendix 1 – Copernicus Global land Component Product and Service Detailed Technical requirements to Technical Annex to Contract Notice 2015/S 151-277962 of 7th August 2015

AD3: GIO Copernicus Global Land – Technical User Group – Service Specification and Product Requirements Proposal – SPB-GIO-3017-TUG-SS-004 – Issue I1.0 – 26 May 2015.

1.3.2 *Input documents*

CGLOPS1_SVP : Service Validation Plan of the Copernicus Global Land Service

GIOGL1_ATBD_SWIV3 Algorithm Theoretical Basis Document of the Soil Water

	Index Version 3 derived from Metop/ASCAT.
CGLOPS1_ATBD_SA1km-V1	Algorithm Theoretical Basis Document of the Surface Albedo Collection 1km Version 1
GIOGL1_ATBD_FAPAR1km-V1	Algorithm Theoretical Basis Document of the FAPAR Collection 1km Version 1
GIOGL1_ATBD_LAI1km-V1	Algorithm Theoretical Basis Document of the LAI Collection 1km Version 1
CGLOPS1_ATBD_FAPAR1km-V2	Algorithm Theoretical Basis Document of the FAPAR Collection 1km Version 2
CGLOPS1_ATBD_LAI1km-V2	Algorithm Theoretical Basis Document of the LAI Collection 1km Version 2
CGLOPS1_ATBD_LST	Algorithm Theoretical Basis Document of the LST derived from geostationary sensors
CGLOPS1_PUM_LAI1km-V1	Product User Manual of LAI Collection 1km Version 1
CGLOPS1_PUM_FAPAR1km-V1	Product User Manual of FAPAR Collection 1km Version 1
CGLOPS1_PUM_SA1km-V1	Product User Manual of Surface Albedo Collection 1km Version 1
CGLOPS1_PUM_LAI1km-V2	Product User Manual of LAI Collection 1km Version 2
CGLOPS1_PUM_FAPAR1km-V2	Product User Manual of FAPAR Collection 1km Version 2
CGLOPS1_PUM_SWI3-SWI10-SWI-TS	Product User Manual of Soil Water Index Version 3
CGLOPS1_PUM_LST	Product User Manual of Land Surface Temperature

All these documents are available on the Copernicus Global Land Service website (<http://land.copernicus.eu/global>) under the respective products pages.

2 METHODS

2.1 LDAS-MONDE

The LDAS-Monde platform was initially developed over France at a spatial resolution of 8 km × 8 km (Barbu et al., 2014). The extension of the LDAS at the global scale was implemented by Albergel et al. (2017) and results from LDAS-Monde over Western Europe and over the Murray-Darling basin (2°N-23°N, 18°W-25°E) are showed here.

The LDAS-Monde platform is able to jointly assimilate remotely sensed surface soil moisture (SWI-001) derived from ASCAT backscatter data [GIOGL1_ATBD_SWIV3] and the LAI Collection 1km V1 [GIOGL1_ATBD_LAI1km-V1] provided by the Copernicus Global Land service, into the ISBA-A-gs land surface model (LSM) within the SURFEX modelling platform. ISBA-A-gs is a version of the ISBA model able to simulate photosynthesis and plant growth. In this report, the new global ERA-5 analysis (Hersbach and Dee, 2016) was used to force LSM simulations over Western Europe and over the Murray-Darling basin, at 0.25° x 0.25° spatial resolution, from 2010 to 2018. ERA-5 is developed through the Copernicus Climate Change Service (C3S). ERA-5 uses one of the most recent versions of the Earth system model and data assimilation methods applied at ECMWF, which makes it able to use modern parameterizations of Earth processes compared to older versions used in ERA-Interim. Two other important features of ERA-5 are the improved temporal and spatial resolution, from 6-hourly in ERA-Interim to hourly analysis in ERA-5, and from 79 km in the horizontal dimension and 60 levels in the vertical, to 31 km and 137 levels in ERA-5.

The Copernicus Global Land Service ASCAT **SWI-001** product is used, as it is equivalent to SSM. The SWI-001 product is generated using an exponential filter with a characteristic time length of one day [GIOGL1_ATBD_SWIV3]. Since (1) soil moisture is a model-dependent variable, (2) the SWI-001 product ranges between 0 (dry) and 1 (saturated), the SWI-001 data need to be bias corrected with respect to the model climatology. A seasonal-based CDF (Cumulative Distribution Function) matching technique is used. It consists of a linear transformation (2 parameters) and produces model equivalent volumetric SSM in m³m⁻³. **The two CDF matching parameters are calculated monthly using a three-month moving window from 2010 to 2017, for each model grid-cell. Therefore, a single set of 12 pairs of parameters is obtained for the whole 2010-2017 period. Moreover, only points with more than 30 observations for each three-month-period were considered so that the CDF matching is assumed to be reliable.** The set of parameters is used to rescale and bias-correct the whole SWI-001 time series from 2010 to 2018.

A major difference with Barbu et al. (2014) is that a new version of the ISBA-A-gs model is used (SURFEX version 8.1 instead of version 7.2). This new version allows the prognostic

simulation of FAPAR, thanks to an enhanced radiative transfer model within the vegetation canopy (Carrer et al., 2013). Another difference is that the snow-free surface albedo values used in the model are now based on a more realistic climatology derived from the MODIS albedo product (MCD43GF) over a 10-year period. A spatially complete albedo is produced using an ecosystem-reliant temporal interpolation technique that retrieves missing data with 3–8% error (Carrer et al., 2014). While the old albedo of a given biome consisted of a constant value (Faroux et al., 2013), the new snow-free albedo has a seasonal component related to the vegetation cover fraction of crops. The vegetation cover fraction of forests and grasslands is constant through time.

In the SURFEX version 8.1 used in this report, the standard deviation of errors of LAI Collection 1km V1 is assumed to be 20% of LAI. The same assumption is made for the standard deviation of errors of the modelled LAI (20% of modelled LAI) for modelled LAI values higher than $2 \text{ m}^2 \text{ m}^{-2}$. For modelled LAI values lower than $2 \text{ m}^2 \text{ m}^{-2}$, a constant error of $0.4 \text{ m}^2 \text{ m}^{-2}$ is assumed. This error configuration was found best in Barbu et al., 2011 (option 3).

Note that the simulated FAPAR and Surface Albedo (SA) are instantaneous values at 09:00 UTC and include the direct and diffuse solar radiation (“blue-sky”). The satellite-derived observations may differ from these conditions. In particular, the CGLS FAPAR corresponds to direct solar radiation conditions (“black-sky”) at 10:00 UTC.

2.2 INPUT PRODUCTS

The following Copernicus Global Land Service products are considered, over the 2010-2018 period:

- Leaf Area Index (LAI), 10 days updates, 1 km, version 1.4 from SPOT-VGT and version 1.5 from PROBA-V, NRT, used in all LAI Figures and Tables of this report
- Leaf Area Index (LAI), 10 days updates, 1 km, version 2, consolidated after 60 days (RT6), used for comparison with version 1
- Fraction of Absorbed Photosynthetically Active Radiation (FAPAR), 10 days updates, 1 km, version 1.4 from SPOT-VGT and version 1.5 from PROBA-V, NRT
- Soil Water Index (SWI), daily, 0.1° , version 3.02, only the SWI-001 field
- Land Surface Temperature (LST), hourly, 5 km, version 1.2
- Surface albedo (SA), broadband bi-hemispheric reflectance over total spectrum (ALBH extracted from the SA product), 10 days updates, 1 km, version 1.4 from SPOT-VGT and version 1.5 from PROBA-V, NRT

The LAI, FAPAR and SA data are provided at a temporal resolution of 10 days. A quality check based on the Quality Flag fields is performed. The data are kept only if all the quality flags are set to 0 (flags for land/water detection, snow presence, aerosol contamination) [CGLOPS1_PUM_LAI1km-V1, CGLOPS1_PUM_FAPAR1km-V1, CGLOPS1_PUM_SA1km-V1].

For the SWI product, a quality flag (QF) related to the number of available SSM measurements used for calculation of Soil Water Index (SWI) is given for each time scale (T). The Surface State Flag (SSF) is provided as in Table 1 [CGLOPS1_PUM_SWIV3].

Table 1: Surface State Flag values of the SWI product

SSF value	Detected surface state
0	unknown
1	unfrozen
2	frozen
3	temporary melting / water on the surface
255	missing value

Before projecting the SWI-001 data onto the ERA5 grid, the observations are screened to remove the observations with a quality flag (QF) lower than 80% and only the data flagged SSF=0 or SSF=1 are used. The 80% QF threshold value is chosen in order to avoid any persistence effect (i.e. the same value being automatically prescribed when observations are missing). The chosen QF threshold value has an impact on the number of used observations, especially at low latitudes, but it was checked that changes in this value have little impact on the scores given in this report. After projection, additional masks for urban regions, steep mountainous terrain, and frozen instances indicated by the model simulations but not detected by ASCAT, are applied.

For LST product, the GLOBE netcdf files are used. Only the LST values corresponding to a QF indicating cloud free pixels (clear sky > 90%) are processed [CGLOPS1_PUM_LST].

After screening for quality flags, the remaining data are projected onto a 0.25° grid, for all the products. The observations are then aggregated over the model grid cell (using a simple arithmetic average) when, at least, half of the observation grid points are present. For 1 km LAI, FAPAR and SA products, this represents at least 312 observations; for the 0.044° LST product, this represents at least 16 observations; for the 0.1° SWI product, this represents at least 3 observations.

We downloaded the products through a subscription on the Copernicus Global Land Service access portal (<https://land.copernicus.vgt.vito.be/PDF/portal/Application.html#Home>).

2.3 EVALUATION METRICS

The LDAS performs the active monitoring of SSM and LAI (these quantities are assimilated into the model), and the passive monitoring of SA, FAPAR, and LST (these quantities are not assimilated into the model). For the five considered variables, the observations are compared to the model simulations after the integration of LAI and SSM observations (i.e. the analysis), and to the model without assimilation (i.e. the open-loop). Several scores are calculated. For the actively monitored variables (SSM and LAI) other LDAS statistics such as the assimilation increments of the analyzed variables (root-zone soil moisture (RZSM) and LAI) can be considered.

2.3.1 Scores

In this report, an indirect validation is made. In a direct validation, in situ reference observations are used as a ground truth. Instead, we use independent model simulations, together with model and observation uncertainty estimates, to monitor the consistency between the seasonal and inter-annual variability of the products and the model.

The LAI and SWI-001 products are assimilated into the ISBA-A-gs model using the LDAS-Monde infrastructure described in Sect. 2.1. Numerical models contain errors that increase with time due to model imperfections and uncertainties in initial and boundary conditions. Data assimilation minimizes these errors by correcting the model statistics using new observations. Integrating observations into a land surface model is also a way to assess and monitor the observation errors. The result of the assimilation is an analysis, i.e. a new model simulation incorporating the information brought by the LAI and SWI-001 products. A rather small impact of the assimilation is observed on SSM. On the other hand, the assimilation has a marked impact on the simulated LAI and on the simulated root-zone soil moisture (RZSM). All the products (the rescaled SWI-001, LAI, FAPAR, SA, LST) are compared with the open-loop model simulation and with the analysis. The impact of the assimilation on RZSM is assessed comparing the open-loop simulation to the analyzed RZSM.

Four metrics are used to compare the satellite products (*sat*) with the model simulations or analyses (*mod*):

- Correlation Coefficient
- Bias
- Standard Deviation of Differences (SDD)

- Root Mean Square Difference (RMSD)

These quantities are defined as:

$$CC = \frac{\sum_{k=1}^N (sat_k - \overline{sat})(mod_k - \overline{mod})}{\sqrt{\sum_{k=1}^N (sat_k - \overline{sat})^2 \sum_{k=1}^N (mod_k - \overline{mod})^2}}$$

$$\text{with } \overline{sat} = \frac{1}{N} \sum_{k=1}^N sat_k ; \quad \overline{mod} = \frac{1}{N} \sum_{k=1}^N mod_k ;$$

N represents the number of gridded observations (equal to the number of different gridded model estimates) used in the calculation of the scores at several dates.

$$Bias = \frac{1}{N} \sum_{k=1}^N (mod_k - sat_k)$$

$$SDD = \sqrt{\frac{1}{N} \sum_{k=1}^N (mod_k - sat_k - Bias)^2}$$

$$RMSD = \sqrt{\frac{1}{N} \sum_{k=1}^N (mod_k - sat_k)^2}$$

2.3.2 Increments

Increments are defined by Eq. (2) in Barbu et al. (2014). They correspond to the difference between the analyzed variables (i.e. after the assimilation of satellite observations) and the model prediction (prior the assimilation):

$$\Delta x = \mathbf{K} [y^0 - H(x)]$$

where x is the state vector (RZSM and LAI), y^0 the observation vector (SSM and LAI), H is the linearized observation operator, and \mathbf{K} is the Kalman gain. The $y = H(x)$ term represents the model counterpart (SSM and LAI) of the observations.

The increments on the state variables impact several key variables such as the carbon (photosynthesis through Gross Primary Production (GPP), net ecosystem exchange (NEE), ecosystem respiration (Reco)) and water (evapotranspiration (ET), drainage) fluxes.

3 RESULTS AT A GLOBAL SCALE

LDAS-Monde was operated at a global scale, at $0.25^\circ \times 0.25^\circ$ spatial resolution, from 2010 to 2018. Figure 1 presents the mean observed LAI V1 (hereafter called GEOV1) values together with the RMSD between the observations and the model (open-loop and analysis). Because LAI observations are integrated into the model, the assimilation tends to reduce the LAI RMSD values. Rather large LAI RMSD values ($> 1.5 \text{ m}^2\text{m}^{-2}$) can remain after the assimilation, especially in forested areas.

In order to perform the cross-cutting evaluation over contrasting areas, 19 regions across the globe known for being potential hot spots for droughts and heat waves were selected. They are listed in Table 2 and presented in Figure 2.

Not all regions can be considered in detail in this report. We select regions affected by severe conditions in 2018 using the SSM and LAI observations. Namely, we focus on regions tending to present smallest values of monthly mean SSM and LAI observations in 2018, rather than in previous years (2010-2017). For each region, Table 2 shows the number of monthly SSM and LAI low records in 2018.

The Western Europe area presents 4 SSM low monthly records and 5 LAI low monthly records in 2018 (Table 2). This result can be related to the late spring and summer European heatwave of 2018 (<https://www.ecmwf.int/en/newsletter/157/news/forecasting-2018-european-heatwave>).

It appears that the Murray-Darling basin in Australia experienced severe conditions in 2018, with 7 SSM low monthly records and 7 LAI low monthly records (Table 2). The Australian Bureau of Meteorology repeatedly reported low records of precipitation for this area (see for example the water bulletin for July 2018, <http://www.bom.gov.au/water/monthly-water-update/IDA30006.2018-07/murray-darling-basin/>). This drought event was also marked by high temperatures (<http://www.agriculture.gov.au/abares/Documents/climate-weekly/weekly20180607.pdf>).

Therefore in this report, the Western Europe and the Murray-Darling regions are considered. Figure 3 illustrates the SSM and LAI records observed in these areas with respect to previous years.

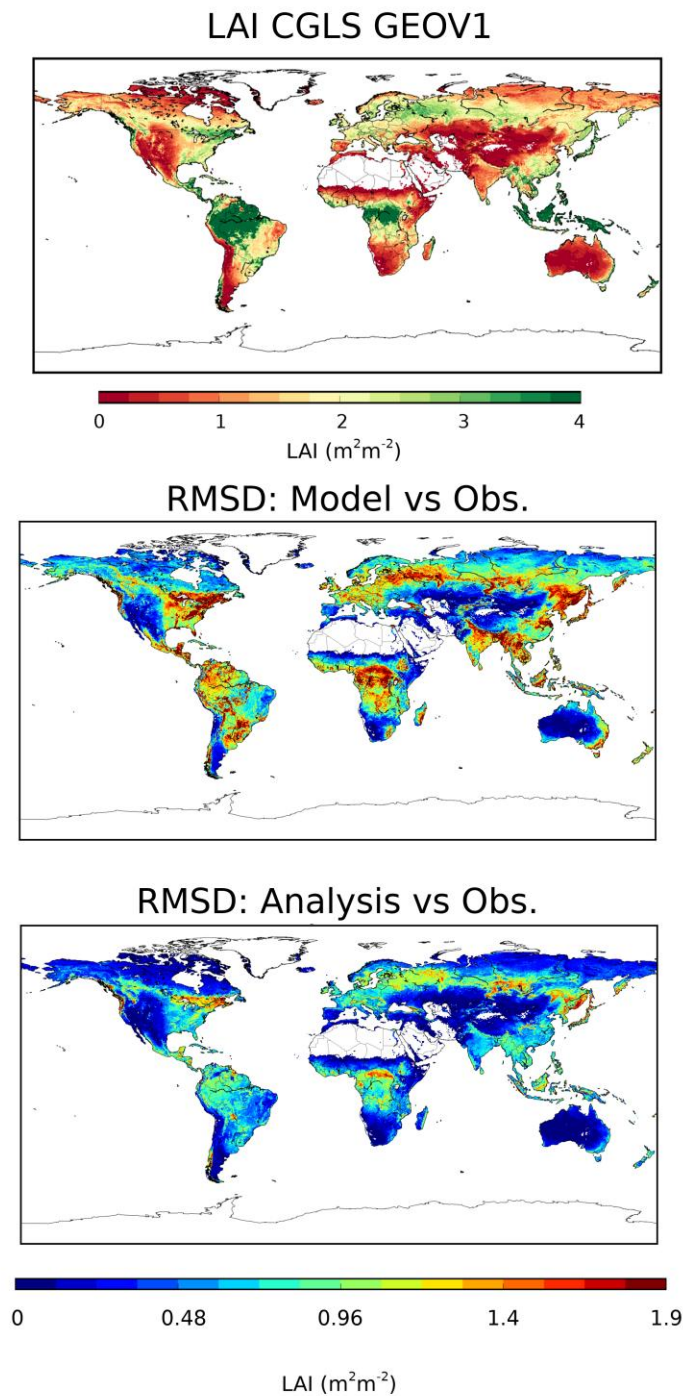


Figure 1: Mean observed LAI for 2010-2018 (top) at a global scale, model open-loop vs. observation RMSD (middle), analysis vs. observation RMSD (bottom).

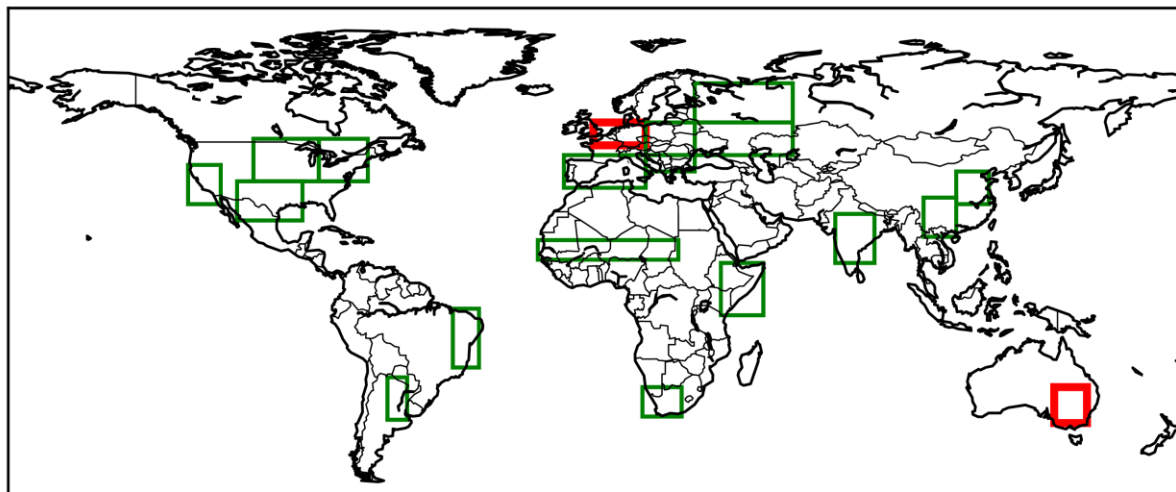


Figure 2: Continental potential hot spots for droughts and heat waves at a global scale. Regions considered in this report affected by severe conditions in 2018 are indicated: Western Europe, and the Murray-Darling basin in Australia.

Table 2: Continental hot spots for droughts and heat waves and number of monthly low SSM and LAI records in 2018 with respect to the 2010-2018 period

Region name	Abbrev.	LON-W	LON-E	LAT-S	LAT-N	Number of monthly low SSM record	Number of monthly low LAI record
Western Europe	WEUR	-1	15	48	55	4	5
Western Mediterranean	WMED	-10	15	35	45	0	1
Eastern Europe	EEUR	15	30	45	55	0	2
Balkans	BALK	15	30	40	45	0	1
Western Russia	WRUS	30	60	55	67	0	0
Lower Volga	LVOL	30	60	45	55	0	0
India	INDI	73	85	12	27	0	0
Southwestern China	SWCH	100	110	20	32	0	0
Northern China	NRCH	110	120	30	40	0	0
Murray-Darling	MUDA	140	150	-37	-26	7	7
California	CALF	-125	-115	30	42	0	4
Southern Plains	SPLN	-110	-90	25	37	0	0
Midwest	MIDW	-105	-85	37	50	1	0
Eastern North	ENRT	-85	-70	37	50	0	0
Nordeste	NDST	-44	-36	-20	-2	0	0
Pampas	PAMP	-64	-58	-36	-23	1	1
Sahel	SAHL	-18	25	13	19	0	1
East Africa	EAFR	38	51	-4	12	1	0
Southern Africa	SAFR	14	26	-35	-26	0	1

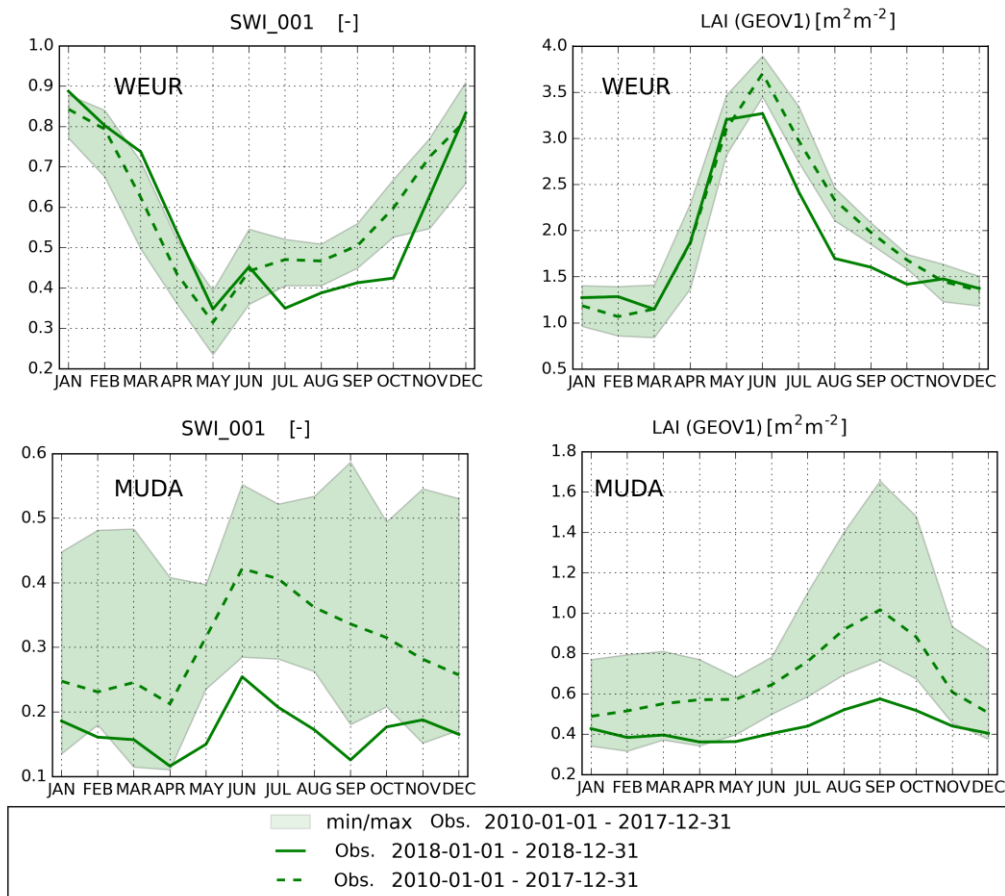


Figure 3: Mean observed monthly (left) SSM and (right) LAI values in 2018 with respect to the minimum, mean and maximum values from 2010 to 2018 over (top) Western Europe (“WEUR”) and (bottom) the Murray-Darling basin (“MUDA”).

Conclusion for results at a global scale:

LDAS-Monde was operated at a global scale from 2010 to 2018 and particularly severe conditions were identified in 2018 over two regions: Western Europe, and the Murray-Darling basin in Australia. Figure 3 shows that LAI values were smaller than previous years from June to October in Western Europe, and from May to October in the Murray-Darling basin. The SSM values were smaller than previous years from July to October in Western Europe, and from May to October in the Murray-Darling basin.

4 RESULTS FOR LAI V1

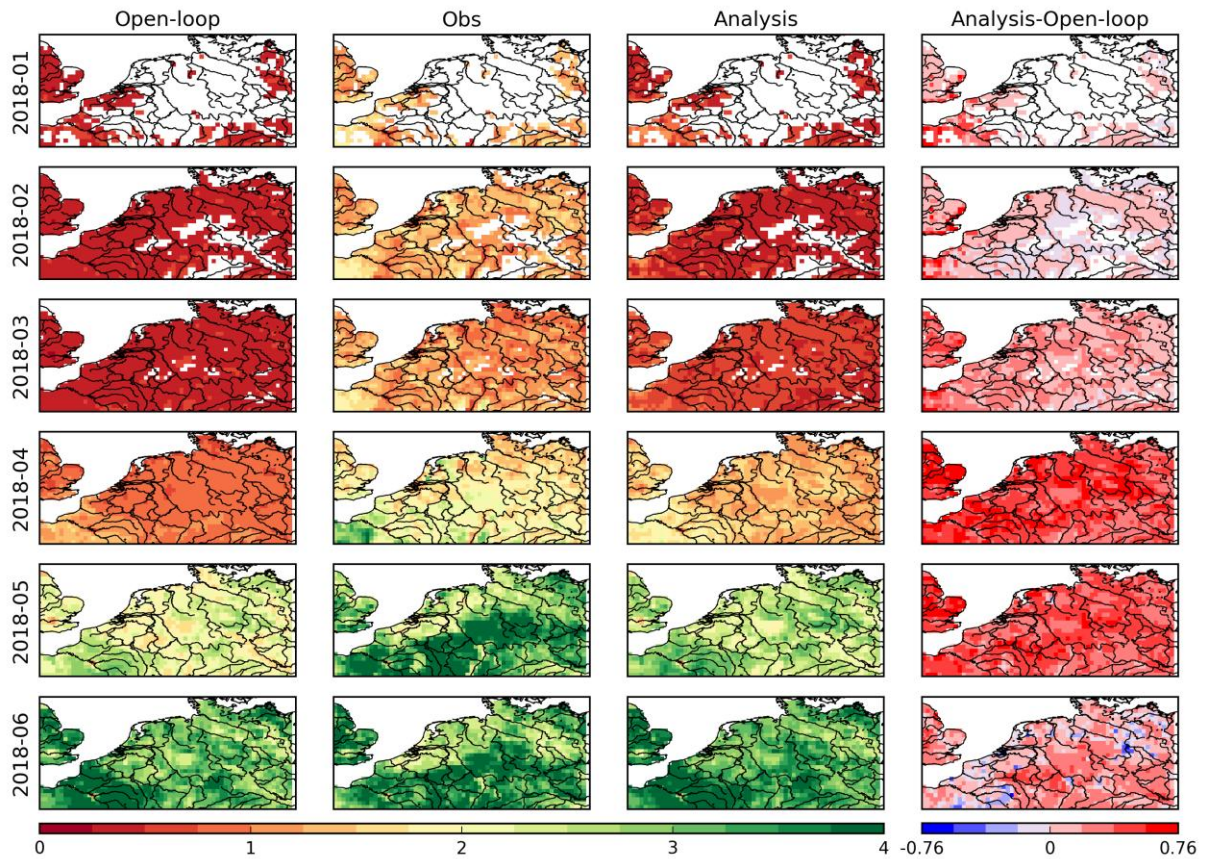


Figure 4: Monthly average values of LAI over Western Europe at 0.25° spatial resolution from January (top) to June 2018 (bottom). From left to right: model, satellite product, analysis, analysis-model difference. The latter shows the impact of assimilating LAI and SWI-001 on the simulated LAI. The color scale range of LAI values is 0 to 4 m²m⁻².

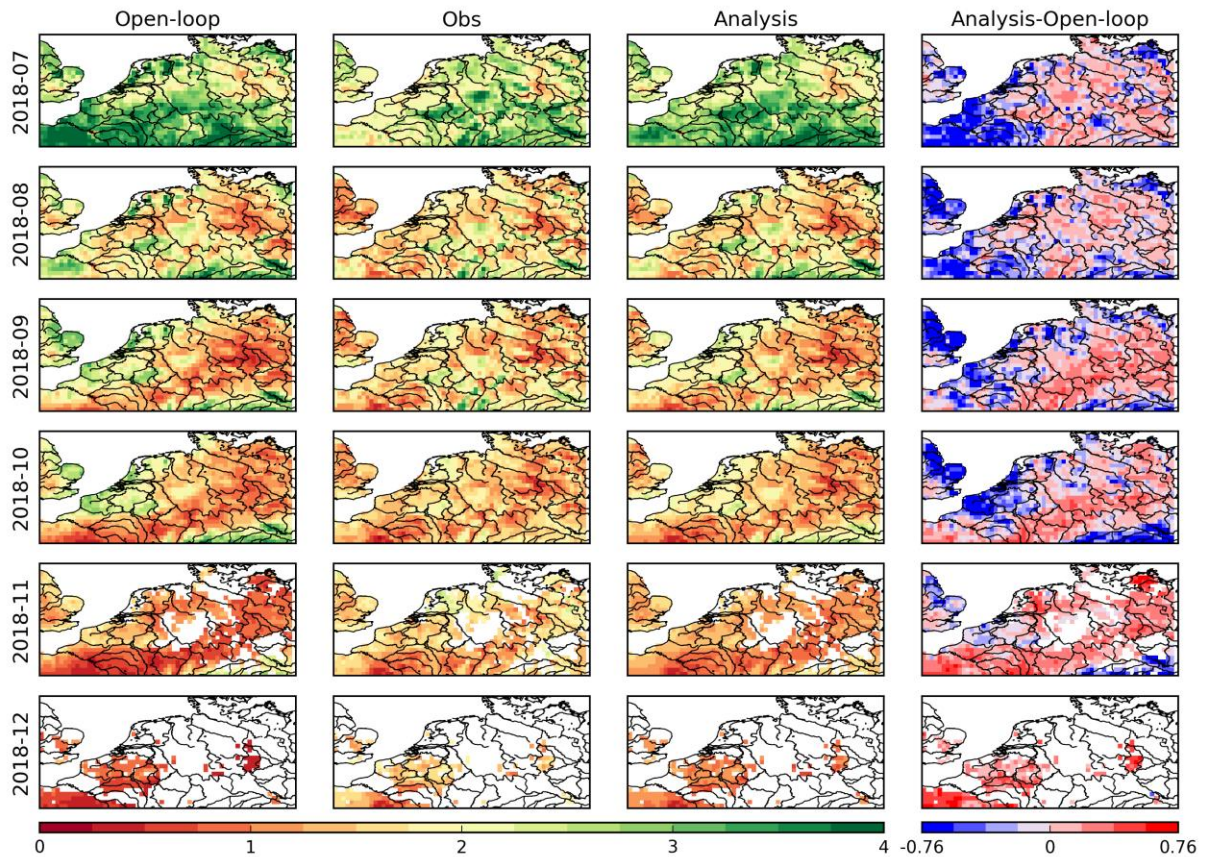


Figure 5: Monthly average values of LAI over Western Europe at 0.25° spatial resolution July (top) to December 2018 (bottom). From left to right: model, satellite product, analysis, analysis-model difference. The latter shows the impact of assimilating LAI and SWI-001 on the simulated LAI. The color scale range of LAI values is 0 to 4 m²m⁻².

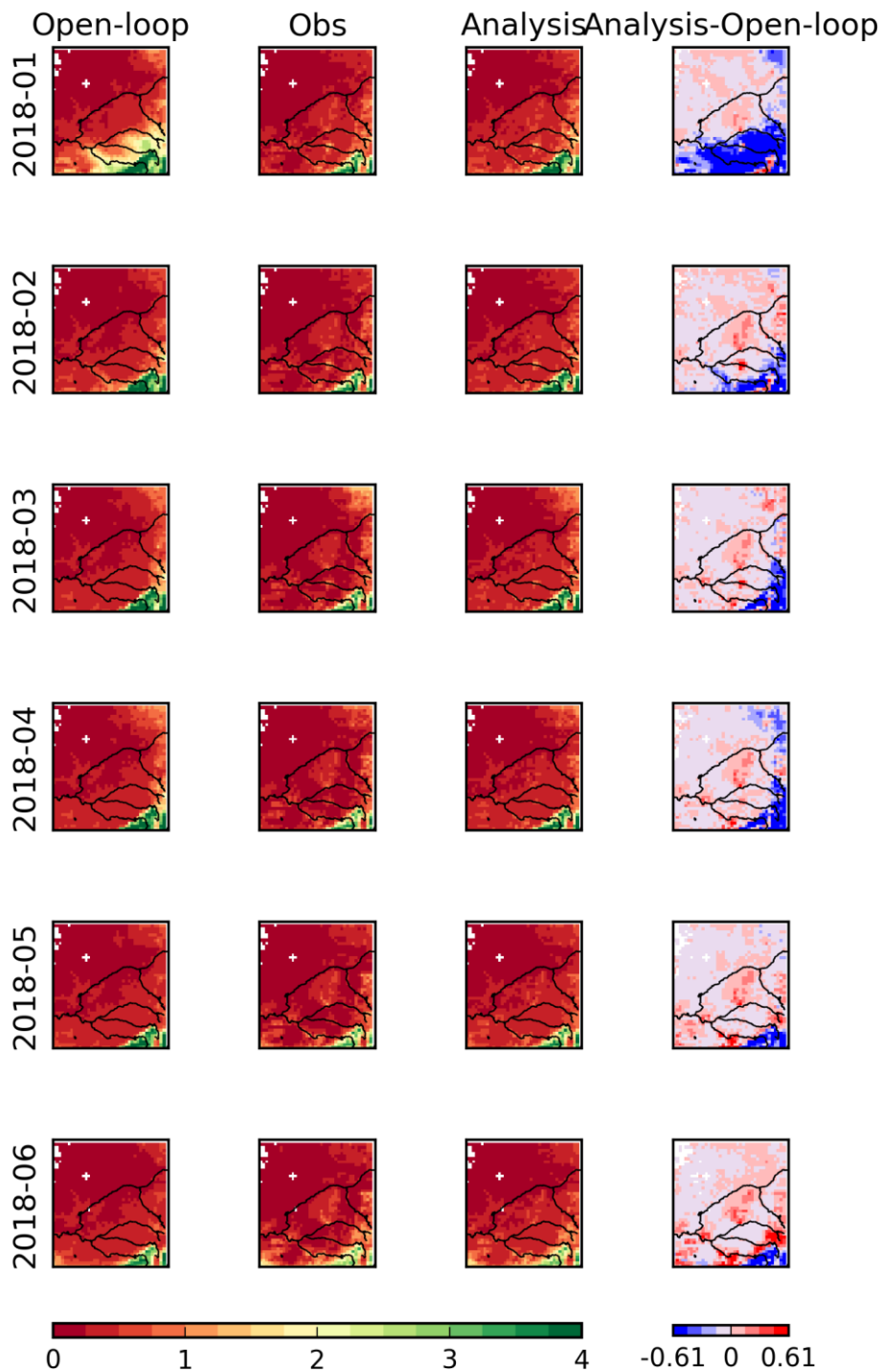


Figure 6: Monthly average values of LAI over the Murray-Darling basin at 0.25° spatial resolution from January (top) to June 2018 (bottom). From left to right: model, satellite product, analysis, analysis-model difference. The latter shows the impact of assimilating LAI and SWI-001 on the simulated LAI. The color scale range of LAI values is 0 to 4 m²m⁻².

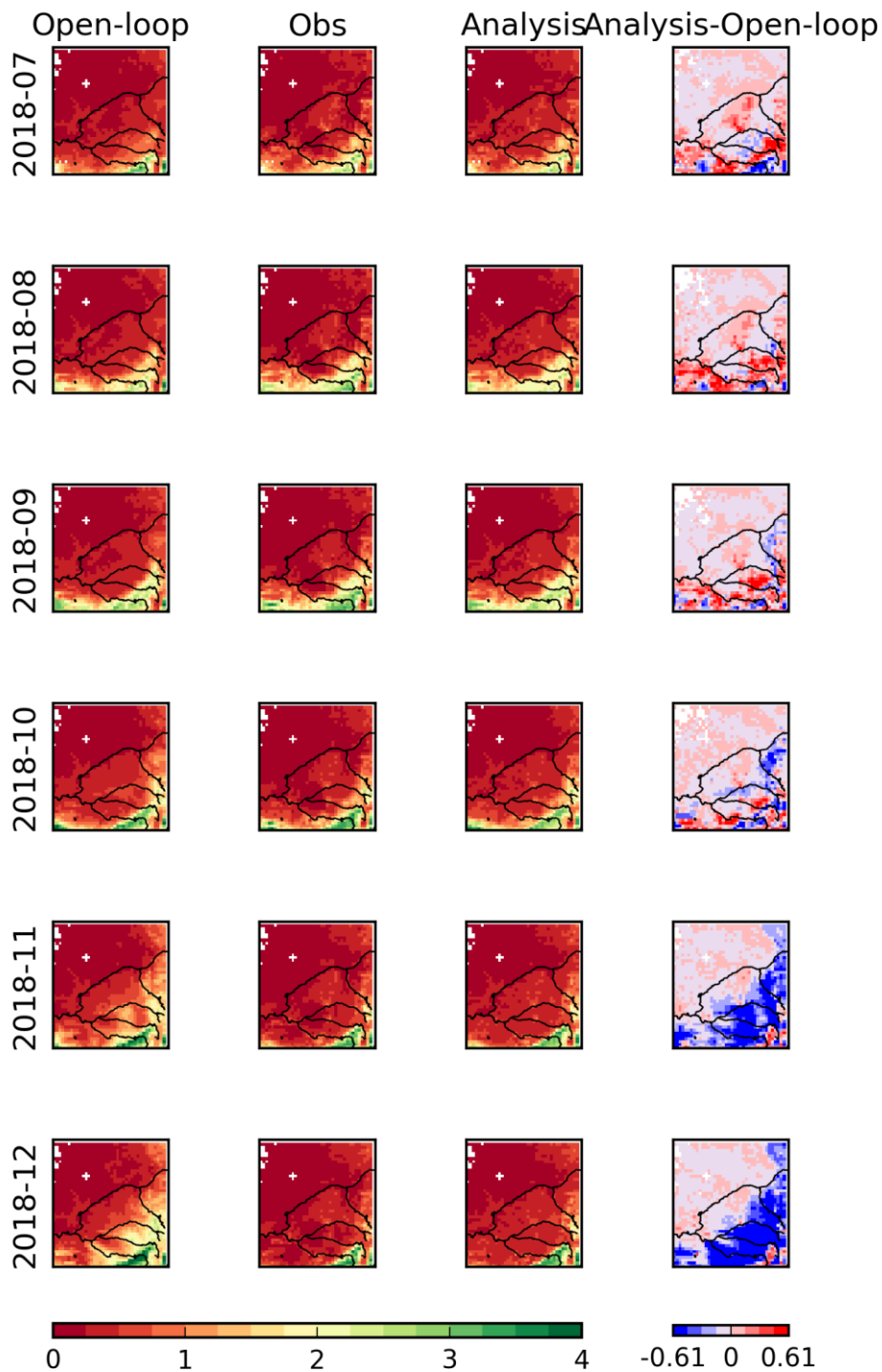


Figure 7: Monthly average values of LAI over the Murray-Darling basin at 0.25° spatial resolution from July (top) to December 2018 (bottom). From left to right: model, satellite product, analysis, analysis-model difference. The latter shows the impact of assimilating LAI and SWI-001 on the simulated LAI. The color scale range of LAI values is 0 to 4 m^2m^{-2} .

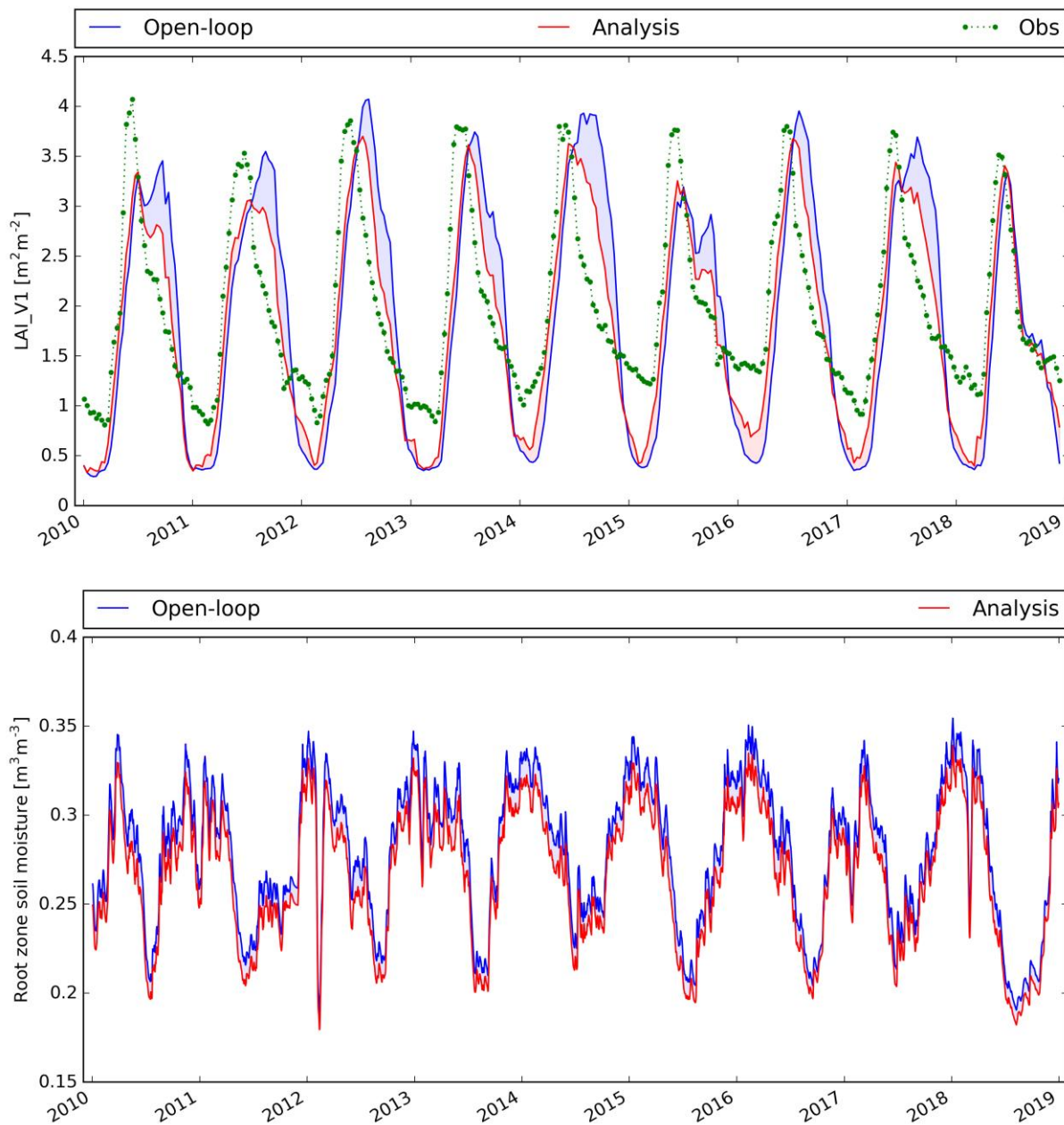


Figure 8: Monthly average values over Western Europe of LAI (top) and root-zone soil moisture (bottom) from 1 January 2010 to 31 December 2018: model (blue line), satellite product (green circles), analysis (red line). Analysis-Model differences show the impact of assimilating LAI and SWI-001 on the simulated LAI and root-zone soil moisture.

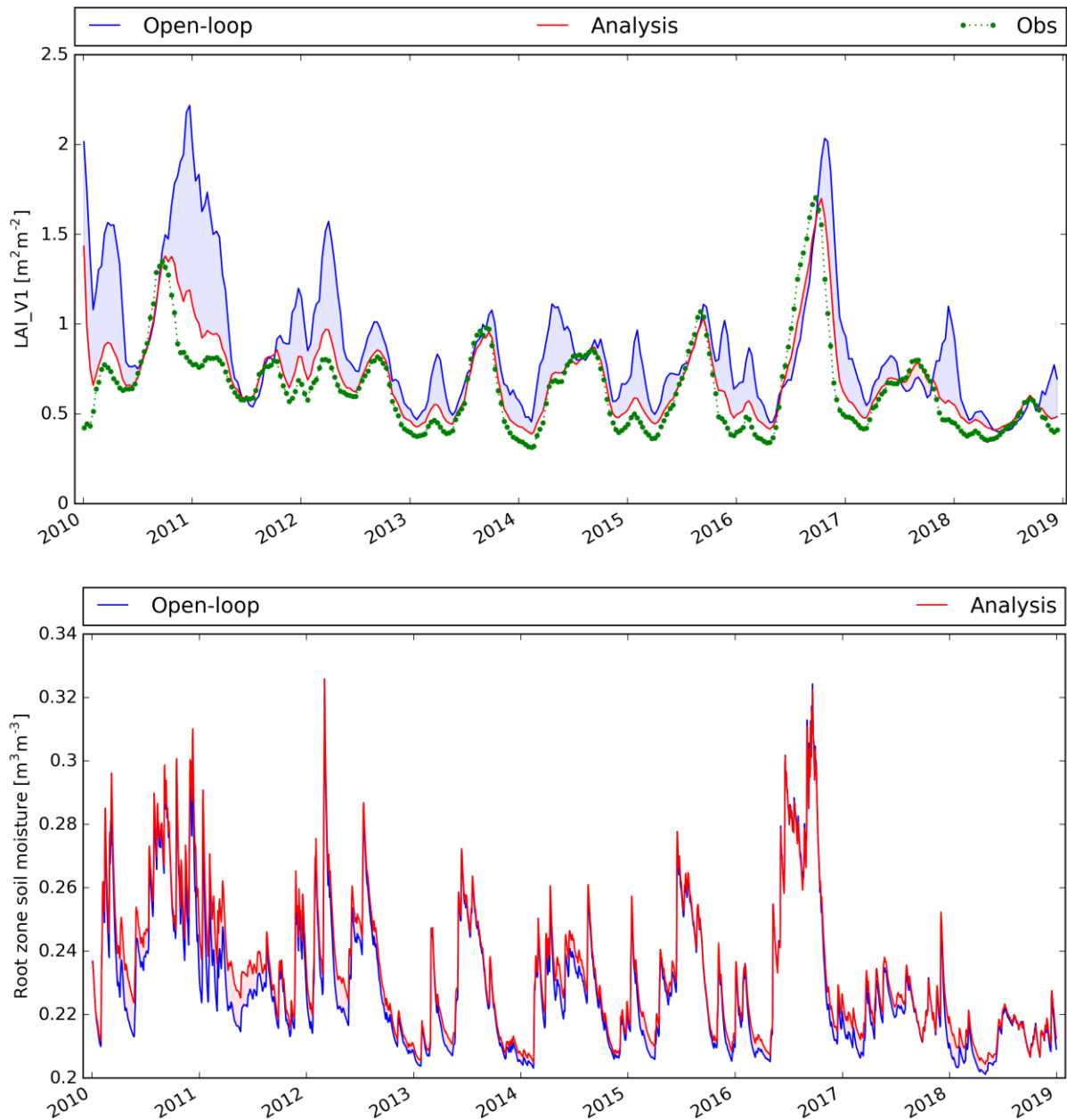
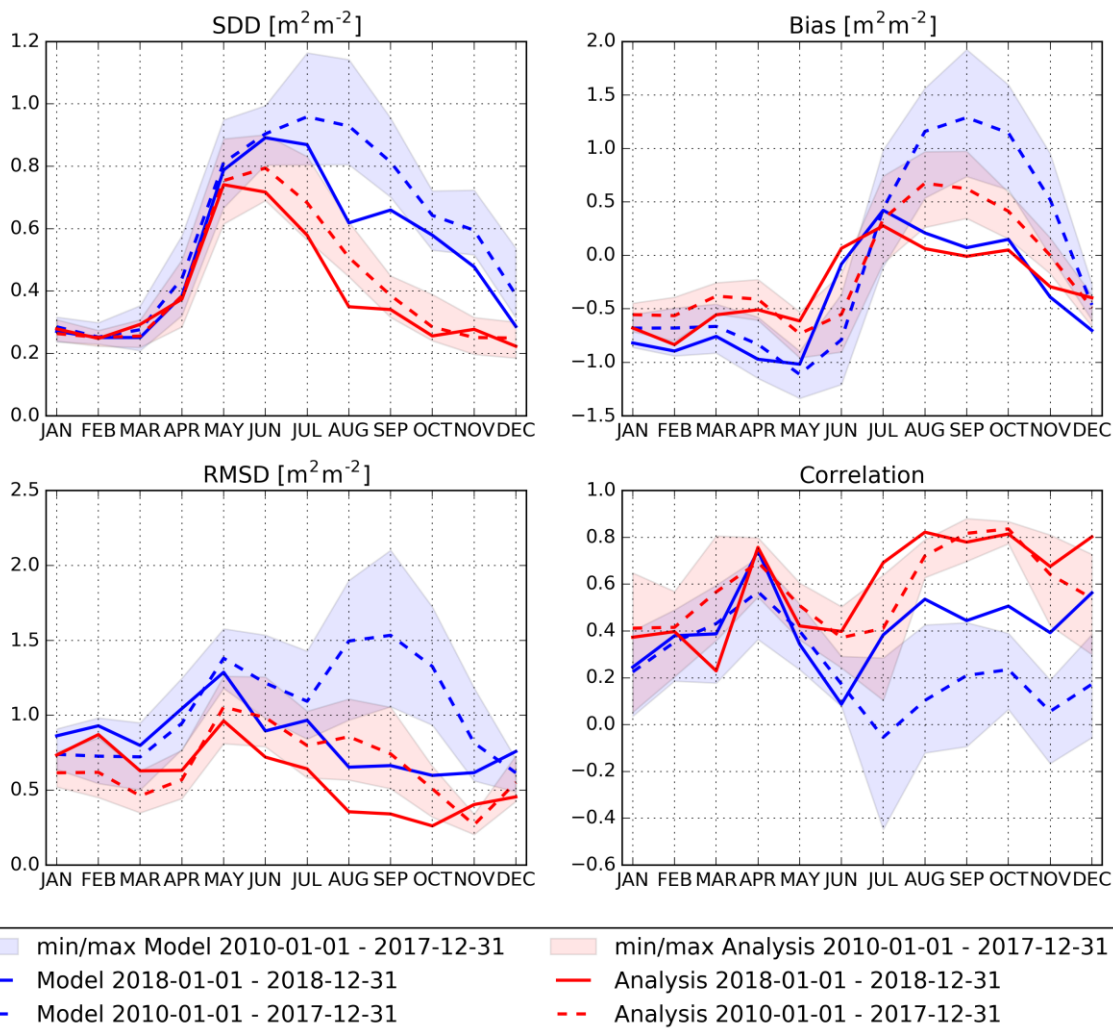
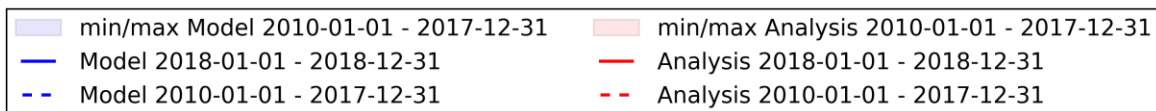
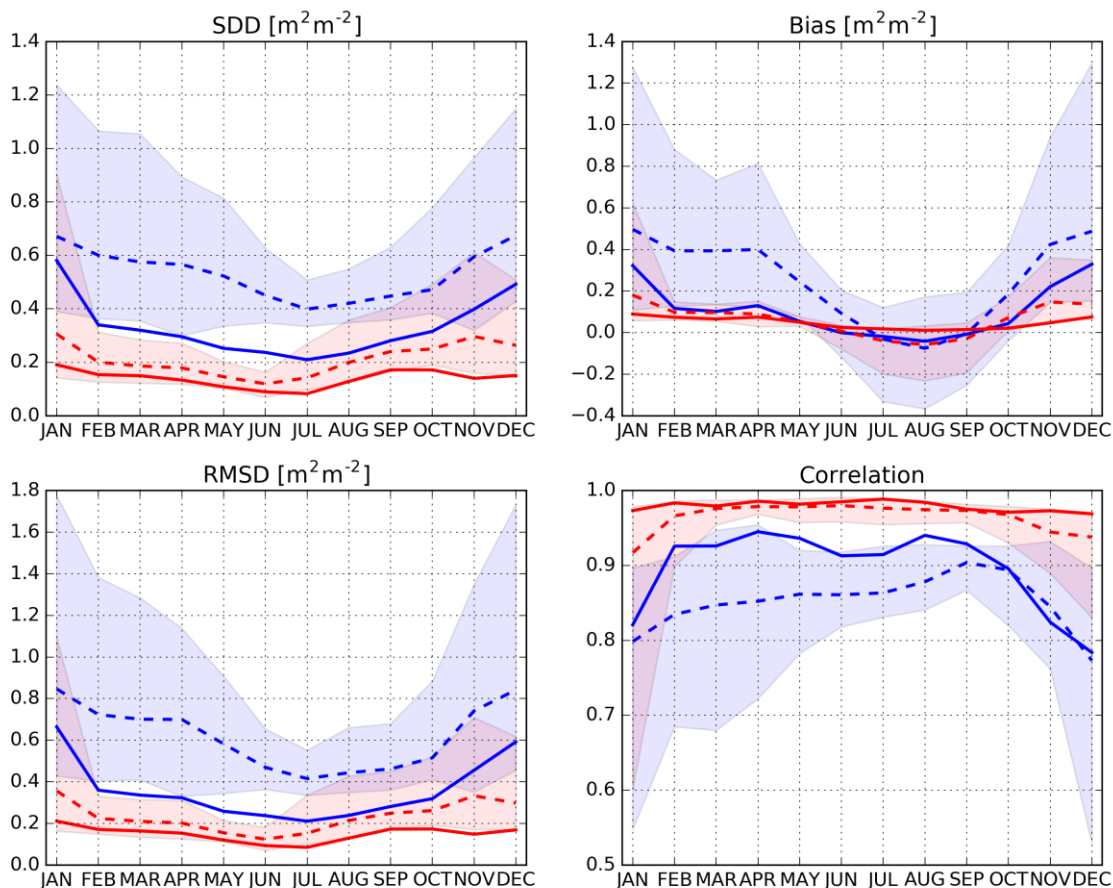


Figure 9: Monthly average values over the Murray-Darling basin of LAI (top) and root-zone soil moisture (bottom) from 1 January 2010 to 31 December 2018: model (blue line), satellite product (green circles), analysis (red line). Analysis-Model differences show the impact of assimilating LAI and SWI-001 on the simulated LAI and root-zone soil moisture.



	JAN	FEB	MAR	APR	MAY	JUN	JUL	AUG	SEP	OCT	NOV	DEC	min	max
2010-01-01 - 2017-12-31	11434	19664	29146	30739	30520	30503	30215	28770	30098	30566	26105	14187	11434	30739
2018-01-01 - 2018-12-31	657	2802	3167	3851	3981	3963	3981	3954	3919	3978	2487	250	250	3981

Figure 10: Monthly LAI scores of the model (blue) and analysis (red) when compared to the observations over Western Europe at 0.25° spatial resolution: from 2010 to 2017 (dashed lines), with N ranging from 11,434 in January to 30,739 in April; and for 2018 (solid lines), with N ranging from 250 in December to 3,981 in July. The monthly N values are indicated in the legend Table. Analysis-Model differences show the impact of assimilating LAI and SWI-001 on the simulated LAI. Shaded areas are between minimum and maximum score values recorded from 2010 to 2017.



	JAN	FEB	MAR	APR	MAY	JUN	JUL	AUG	SEP	OCT	NOV	DEC	min	max
2010-01-01 - 2017-12-31	41677	41675	41661	41669	41667	41656	41535	41594	41625	41672	41681	41675	41535	41681
2018-01-01 - 2018-12-31	5211	5211	5211	5211	5204	5185	5092	5154	5204	5210	5211	3474	3474	5211

Figure 11: Monthly LAI scores of the model (blue) and analysis (red) when compared to the observations over the Murray-Darling basin at 0.25° spatial resolution: from 2010 to 2017 (dashed lines), with N ranging from 41,535 in July to 41,681 in November; and for 2018 (solid lines), with N ranging from 3,474 in December to 5,211. The monthly N values are indicated in the legend Table. Analysis-Model differences show the impact of assimilating LAI and SWI-001 on the simulated LAI. Shaded areas are between minimum and maximum score values recorded from 2010 to 2017.

Table 3: Model and analysis LAI scores from 2010 to 2017 and for 2018 over Western Europe (top), from 2010 to 2017 and for 2018 over the Murray-Darling basin (bottom). Analysis-Model differences show the impact of assimilating LAI and SWI-001 on the simulated LAI. Mean bias, RMSD and SDD are in m^2m^{-2} .

	Version	Bias	Correlation	RMSD	SDD	Nb_pts
2010-01-01 - 2017-12-31	Model	0.005	0.509	1.162	1.162	311947
2010-01-01 - 2017-12-31	Analysis	-0.084	0.765	0.730	0.725	311947
2018-01-01 - 2018-12-31	Model	-0.306	0.667	0.878	0.823	36990
2018-01-01 - 2018-12-31	Analysis	-0.216	0.819	0.622	0.583	36990

	Version	Bias	Correlation	RMSD	SDD	Nb_pts
2010-01-01 - 2017-12-31	Model	0.250	0.781	0.694	0.648	499787
2010-01-01 - 2017-12-31	Analysis	0.063	0.943	0.273	0.266	499787
2018-01-01 - 2018-12-31	Model	0.098	0.865	0.374	0.361	60578
2018-01-01 - 2018-12-31	Analysis	0.046	0.972	0.152	0.145	60578

Conclusion for LAI:

During the drought period over Western Europe from August to October, both modelled and analyzed LAI present better SDD and RMSD scores values than those observed during the 2010-2017 reference period of time (Figure 10). Time series in Figure 8 show that modelled and analyzed LAI are closer to observations than for previous years. Over the Murray-Darling basin, all scores present better values during the 2018 dry spell than those observed during the 2010-2017 reference period of time, especially from May to September (Figure 11).

For both Western Europe and Murray-Darling basin, all annual scores (apart from the mean bias over Western Europe) present better values in 2018 than those observed during the 2010-2017 reference period of time (Table 3).

The model bias presents a marked seasonality over Western Europe (Figure 10). This is caused by a delayed peak LAI date in the model simulations (Figure 8). This could be attributed to biases in the ERA5 radiation forcing of the model (Urraca et al., 2018). However, the LAI bias is much reduced in 2018 with respect to previous years. A bias seasonality can also be observed over the Murray-Darling basin, much reduced in 2018 with respect to previous years. The analyzed LAI hardly presents any bias (Figure 11).

Over Western Europe, the model LAI bias presents a marked seasonality (Figure 10). This is caused by a delayed peak LAI date in the model simulations that could be caused by remaining biases in the ERA5 incoming solar radiation (Urraca et al., 2018). The LAI bias seasonality is present to some extent over the Murray-Darling basin (Figure 11) but is almost completely suppressed by the assimilation.

Figure 4 and Figure 5 show that the assimilation of SSM and LAI observations tends to reinforce the drought signal over Western Europe, with smaller LAI values in the analysis over northern France from July to October, eastern England from August to October, the Netherlands and Belgium in October, Bavaria from August to November. Figure 6 and Figure 7 show that the assimilation of SSM and LAI observations markedly reduces LAI values over the southwestern part of the Murray-Darling basin, in January, November, and December.

5 RESULTS FOR FAPAR V1

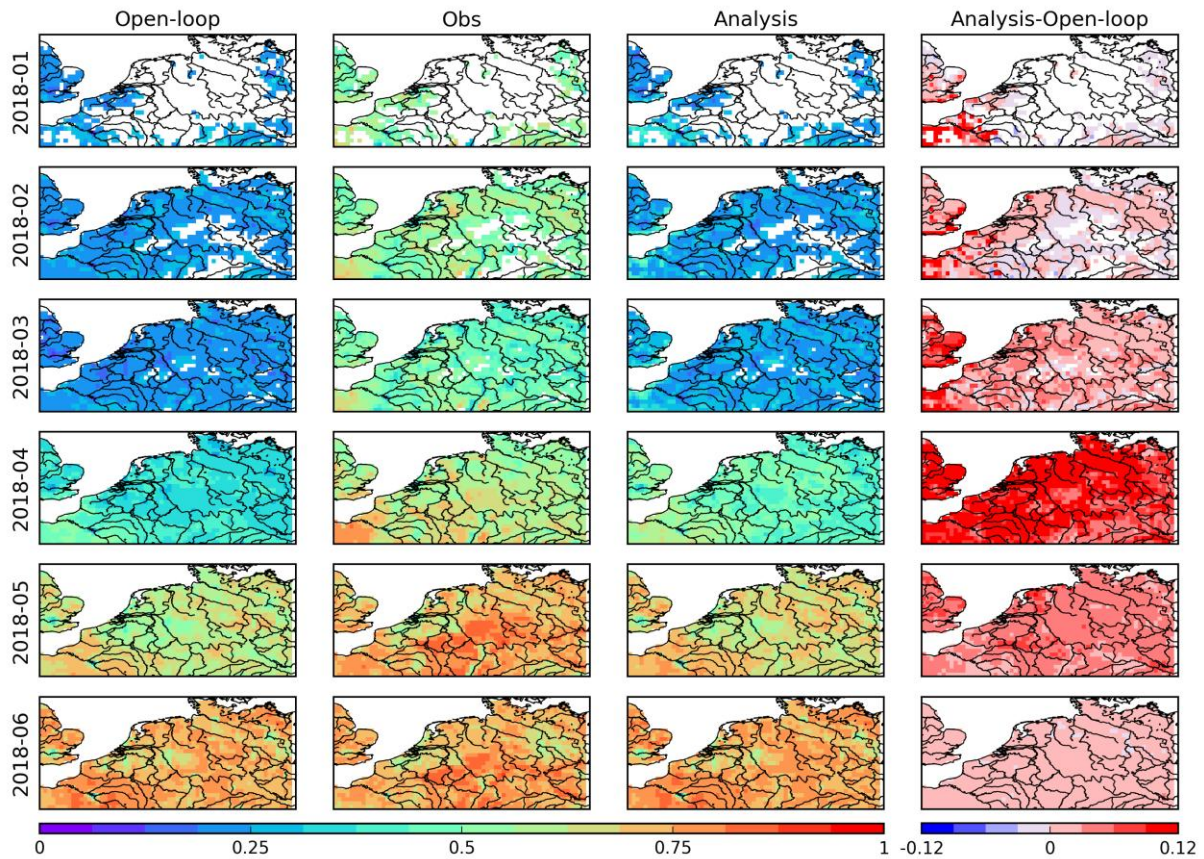


Figure 12: Monthly average values of FAPAR over Western Europe at 0.25° spatial resolution from January (top) to June 2018 (bottom). From left to right: model, satellite product, analysis, analysis-model difference. The latter shows the impact of assimilating LAI and SWI-001 on the simulated FAPAR. The color scale range of FAPAR values is 0 to 1.0.

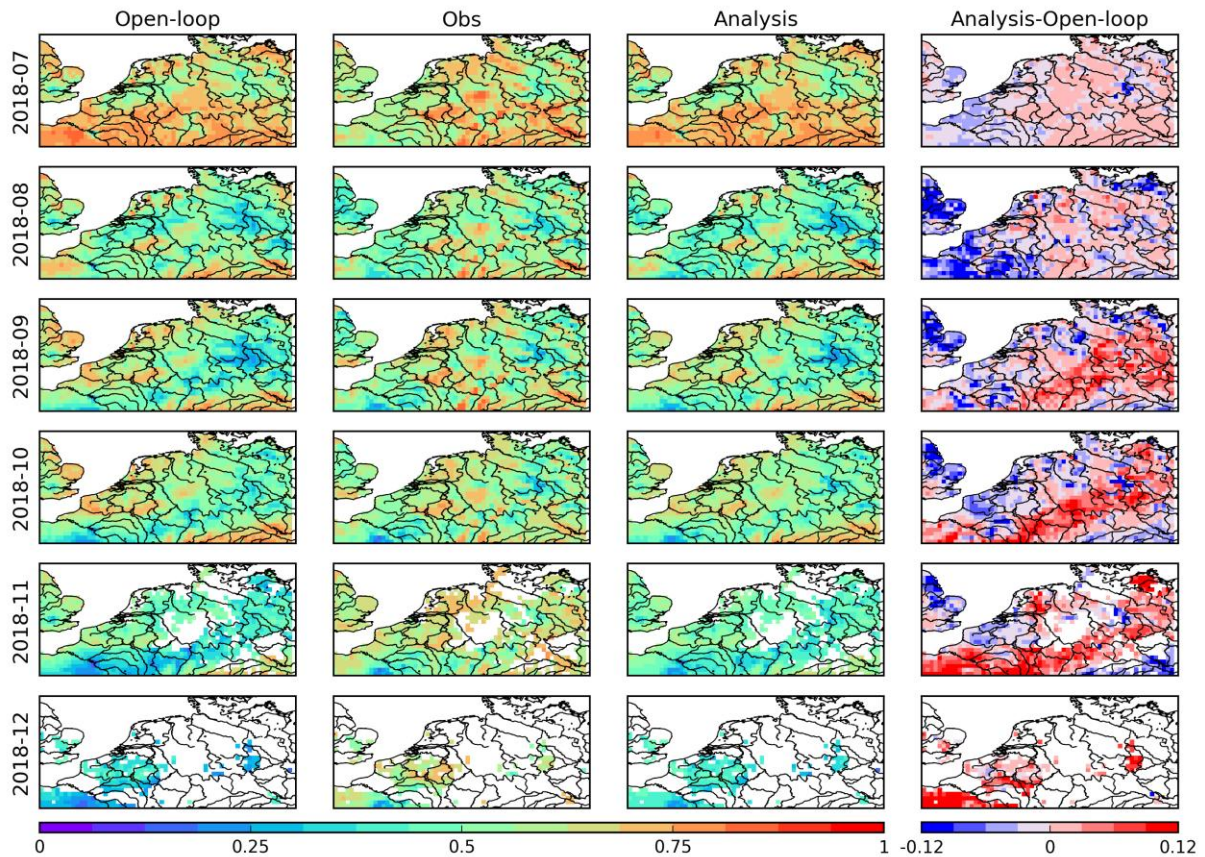


Figure 13: Monthly average values of FAPAR over Western Europe at 0.25° spatial resolution July (top) to December 2018 (bottom). From left to right: model, satellite product, analysis, analysis-model difference. The latter shows the impact of assimilating LAI and SWI-001 on the simulated FAPAR. The color scale range of FAPAR values is 0 to 1.0.

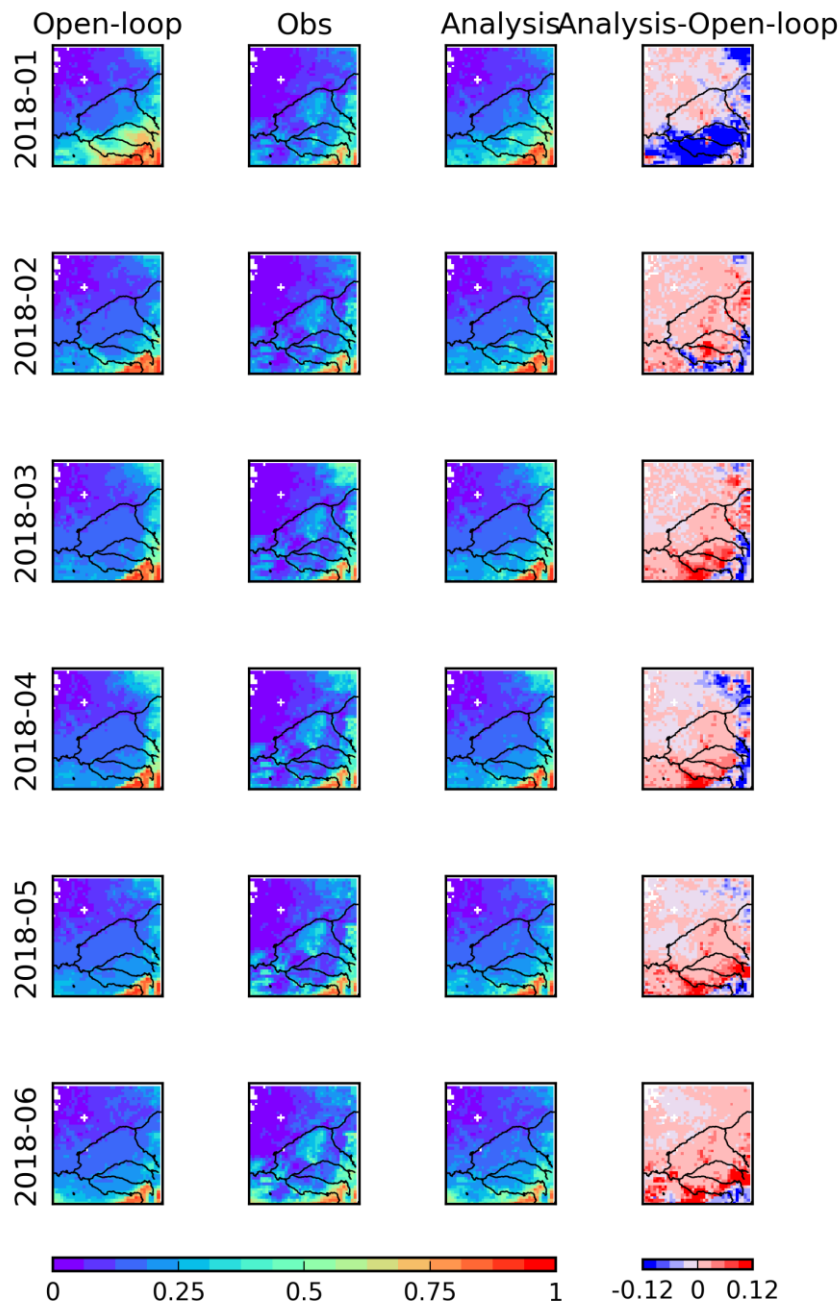


Figure 14: Monthly average values of FAPAR over the Murray-Darling basin at 0.25° resolution January (top) to June 2018 (bottom). From left to right: model, satellite product, analysis, analysis-model difference. The latter shows the impact of assimilating LAI and SWI-001 on the simulated FAPAR. The color scale range of FAPAR values is 0 to 1.0

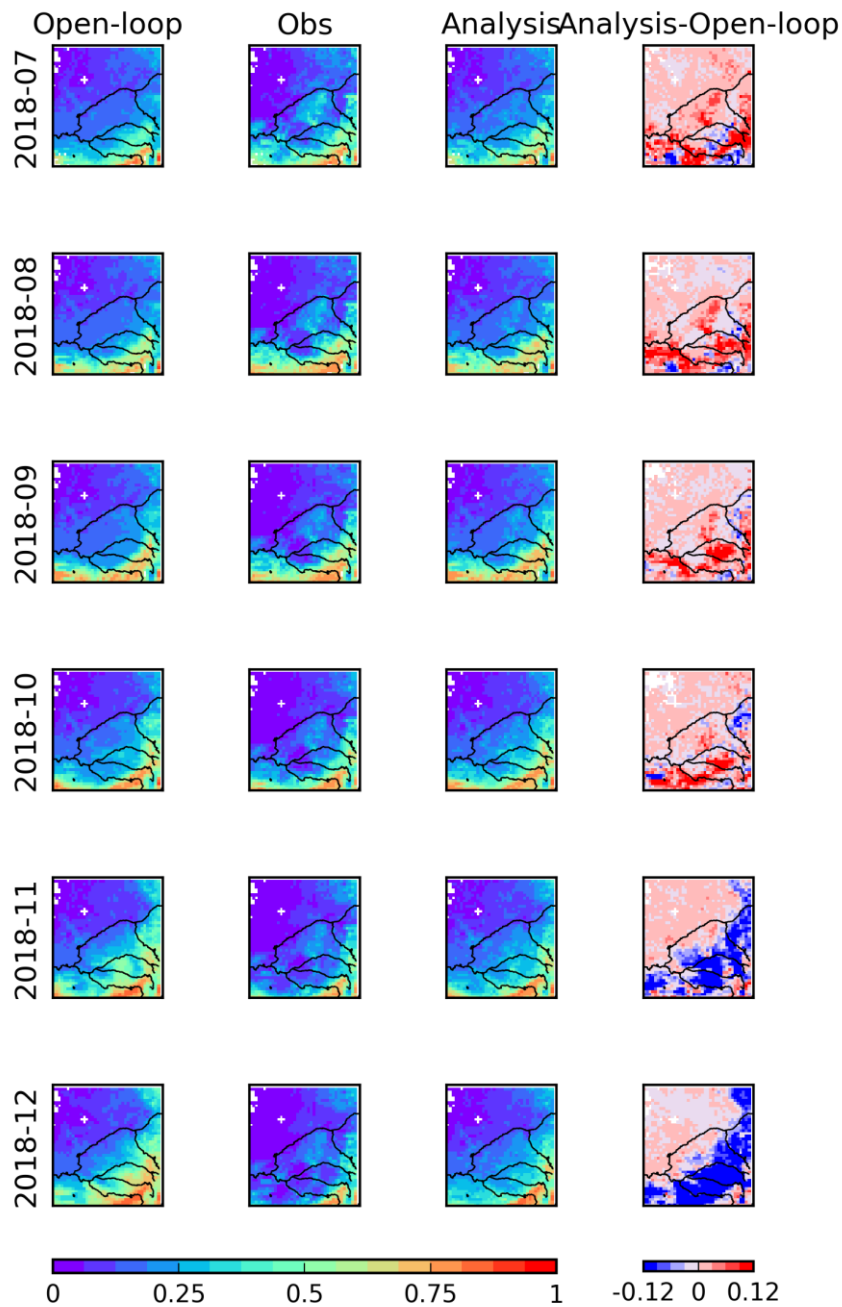


Figure 15: Monthly average values of FAPAR over the Murray-Darling basin at 0.25° resolution July (top) to December 2018 (bottom). From left to right: model, satellite product, analysis, analysis-model difference. The latter shows the impact of assimilating LAI and SWI-001 on the simulated FAPAR. The color scale range of FAPAR values is 0 to 1.0

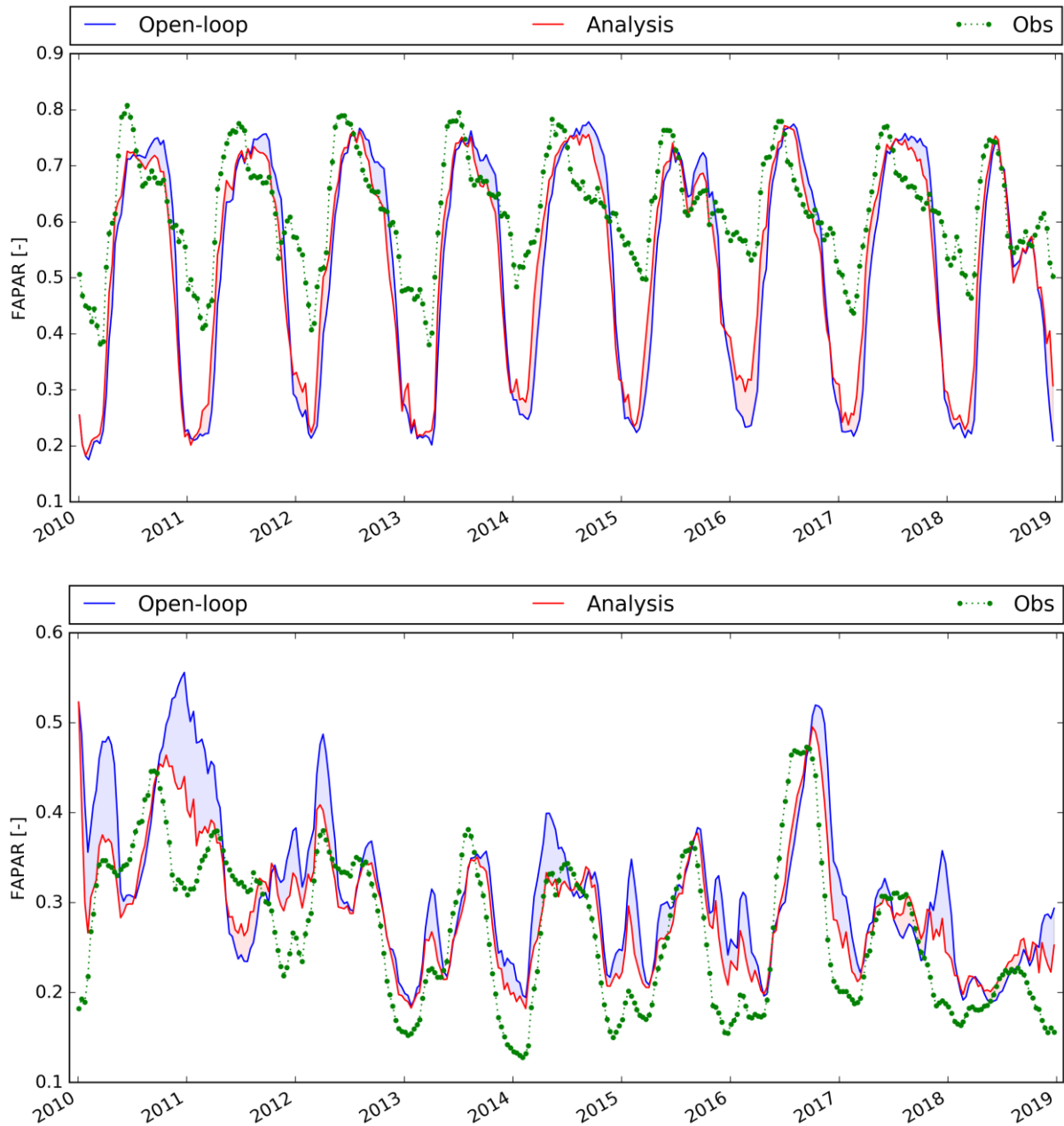
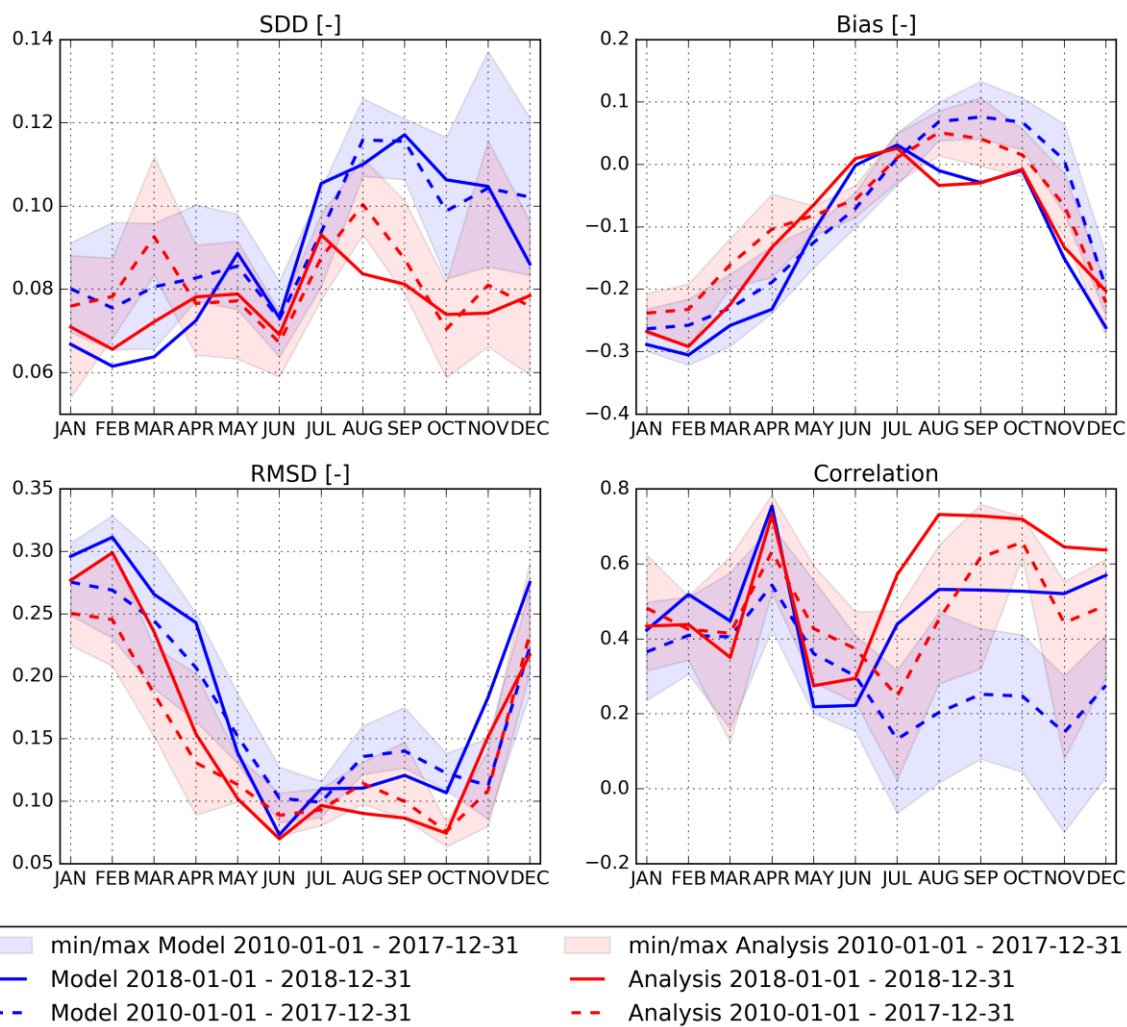
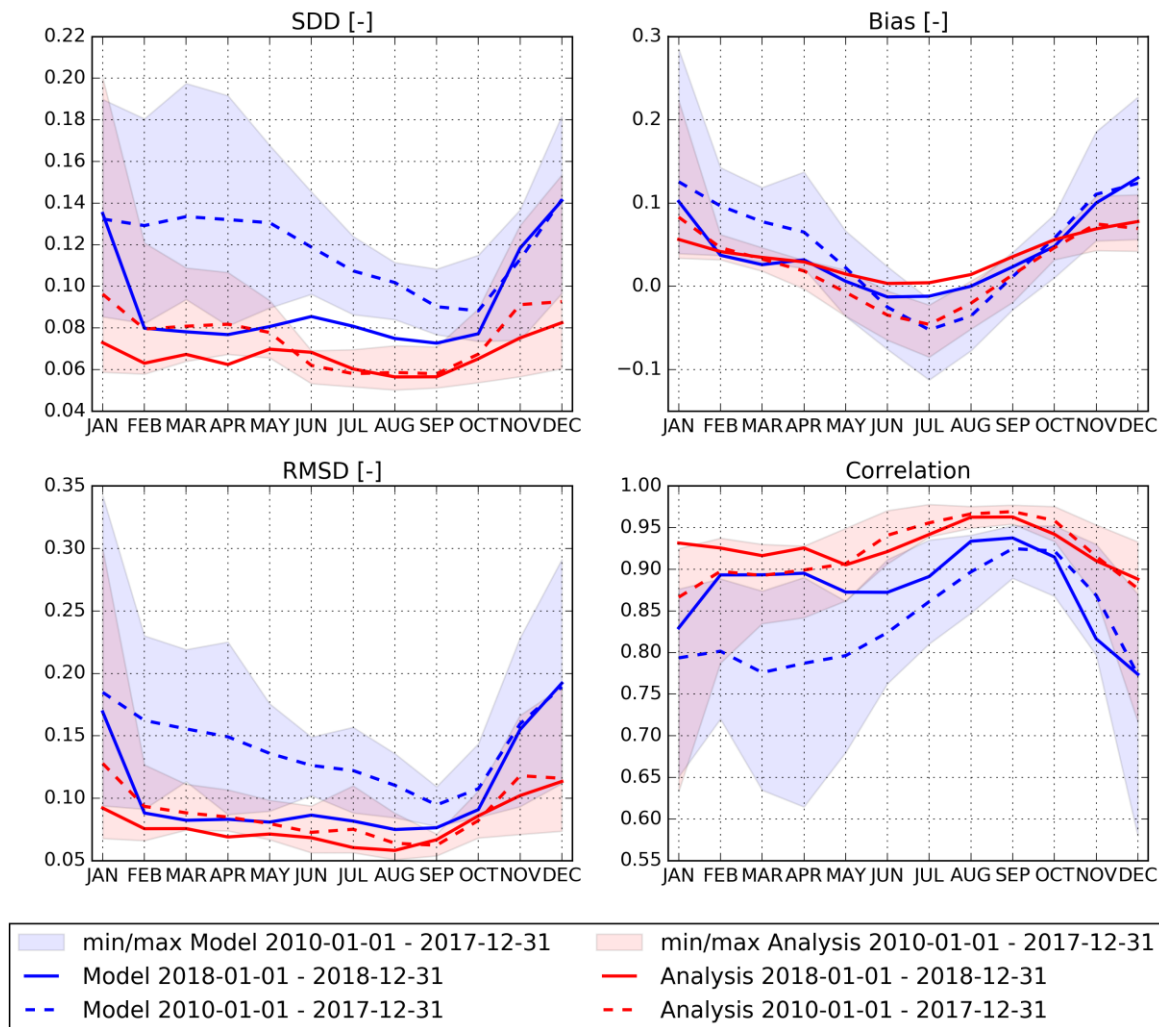


Figure 16: Monthly average values of FAPAR over Western Europe (top) from 2010 to 2018, the Murray-Darling basin (bottom) from 2010 to 2018: model (blue line), satellite product (green circles), analysis (red line). Analysis-Model differences show the impact of assimilating LAI and SWI-001 on the simulated FAPAR.



	JAN	FEB	MAR	APR	MAY	JUN	JUL	AUG	SEP	OCT	NOV	DEC	min	max
2010-01-01 - 2017-12-31	11450	19674	29149	30745	30577	30634	30253	28771	30100	30581	26143	14211	11450	30745
2018-01-01 - 2018-12-31	657	2802	3167	3851	3983	3964	3982	3954	3919	3978	2487	256	256	3983

Figure 17: Monthly FAPAR scores of the model (blue) and analysis (red) when compared to the observations over Western Europe at a 0.25° spatial resolution: from 2010 to 2017 (dashed lines), with N ranging from 11,450 in January to 30,745 in May; and for 2018 (solid lines), with N ranging from 256 in December to 3,983 in May. The monthly N values are indicated in the legend Table. Analysis-Model differences show the impact of assimilating LAI and SWI-001 on the simulated FAPAR. Shaded areas are between minimum and maximum score values recorded from 2010 to 2017.



	JAN	FEB	MAR	APR	MAY	JUN	JUL	AUG	SEP	OCT	NOV	DEC	min	max
2010-01-01 - 2017-12-31	41678	41679	41668	41673	41668	41656	41537	41597	41625	41672	41682	41675	41537	41682
2018-01-01 - 2018-12-31	5211	5211	5211	5211	5204	5185	5093	5154	5204	5210	5211	5211	5093	5211

Figure 18: Monthly FAPAR scores of the model (blue) and analysis (red) when compared to the observations over the Murray-Darling basin at 0.25° spatial resolution: from 2010 to 2017 (dashed lines), with N ranging from 41,537 in July to 41,682 in November; and for 2018 (solid lines), with N ranging from 5,093 in July to 5,211. The monthly N values are indicated in the legend Table. Analysis-Model differences show the impact of assimilating LAI and SWI-001 on the simulated FAPAR. Shaded areas are between the minimum and maximum score values recorded from 2010 to 2017.

Table 4: Model and analysis FAPAR scores from 2010 to 2017 and for 2018 over Western Europe (top), from 2010 to 2017 and for 2018 over the Murray-Darling basin (bottom). Analysis-Model differences show the impact of assimilating LAI and SWI-001 on the simulated FAPAR.

	Version	Bias	Correlation	RMSD	SDD	Nb_pts
2010-01-01 - 2017-12-31	Model	-0.073	0.632	0.174	0.158	312288
2010-01-01 - 2017-12-31	Analysis	-0.066	0.733	0.142	0.126	312288
2018-01-01 - 2018-12-31	Model	-0.100	0.624	0.179	0.148	37000
2018-01-01 - 2018-12-31	Analysis	-0.081	0.714	0.149	0.125	37000

	Version	Bias	Correlation	RMSD	SDD	Nb_pts
2010-01-01 - 2017-12-31	Model	0.048	0.800	0.150	0.142	499810
2010-01-01 - 2017-12-31	Analysis	0.023	0.902	0.095	0.092	499810
2018-01-01 - 2018-12-31	Model	0.040	0.833	0.112	0.105	62316
2018-01-01 - 2018-12-31	Analysis	0.037	0.917	0.080	0.071	62316

Conclusion for FAPAR:

Overall conclusions for FAPAR are similar to those for LAI, but the impact of the heat wave over Western Europe on observed and analyzed FAPAR and on FAPAR scores is less pronounced than for LAI.

During the drought period over Western Europe from August to October, both modelled and analyzed FAPAR present better correlation, SDD and RMSD scores values than those observed during the 2010-2017 reference period of time (Figure 17). Time series in Figure 16 show that modelled and analyzed FAPAR are closer to observations than for previous years. Over the Murray-Darling basin, model scores present better values during the 2018 dry spell than those observed during the 2010-2017 reference period of time, from March to September (Figure 18).

For the Murray-Darling basin, all annual scores present slightly better values in 2018 than those observed during the 2010-2017 reference period of time (Table 4).

The model bias presents a marked seasonality over Western Europe (Figure 17). This is caused by a delayed peak LAI date in the model simulations that could be caused by remaining biases in the ERA5 incoming solar radiation (Urraca et al., 2018). A slight bias seasonality can also be observed over the Murray-Darling basin, much reduced in 2018 with respect to previous years (Figure 18).

Figure 12 and Figure 13 show that the assimilation of SSM and LAI observations tends to slightly reinforce the drought signal over Western Europe, with smaller FAPAR values in the analysis over northern France in August, eastern England from August to November, Bavaria in November.

Figure 14 and Figure 15 show that the assimilation of SSM and LAI observations markedly reduces FAPAR values over the southwestern part of the Murray-Darling basin, in January, November, and December.

6 RESULTS FOR SURFACE ALBEDO

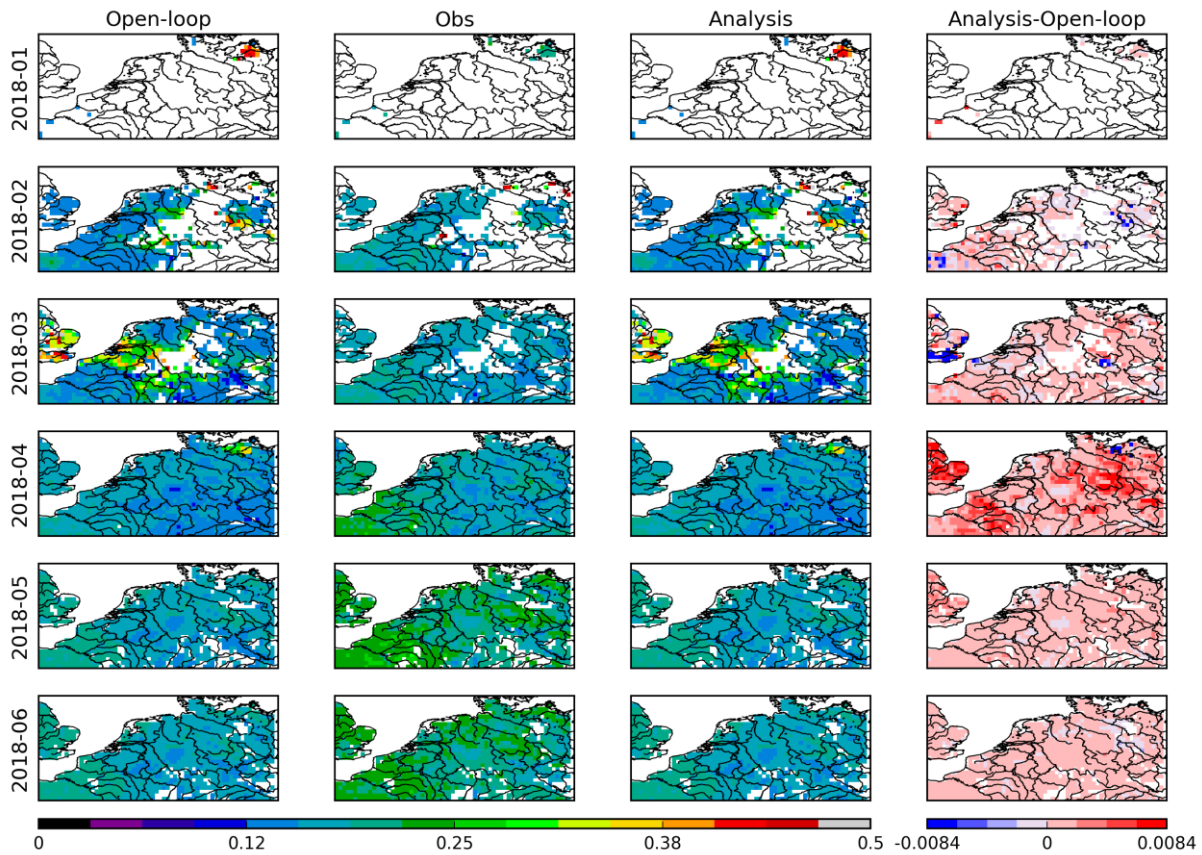


Figure 19: Monthly average values of Surface Albedo over Western Europe at 0.25° spatial resolution from January (top) to June 2018 (bottom). From left to right: model, satellite product, analysis, analysis-model difference. The latter shows the impact of assimilating LAI and SWI-001 on the simulated SA. The color scale range of SA values is 0 to 0.5.

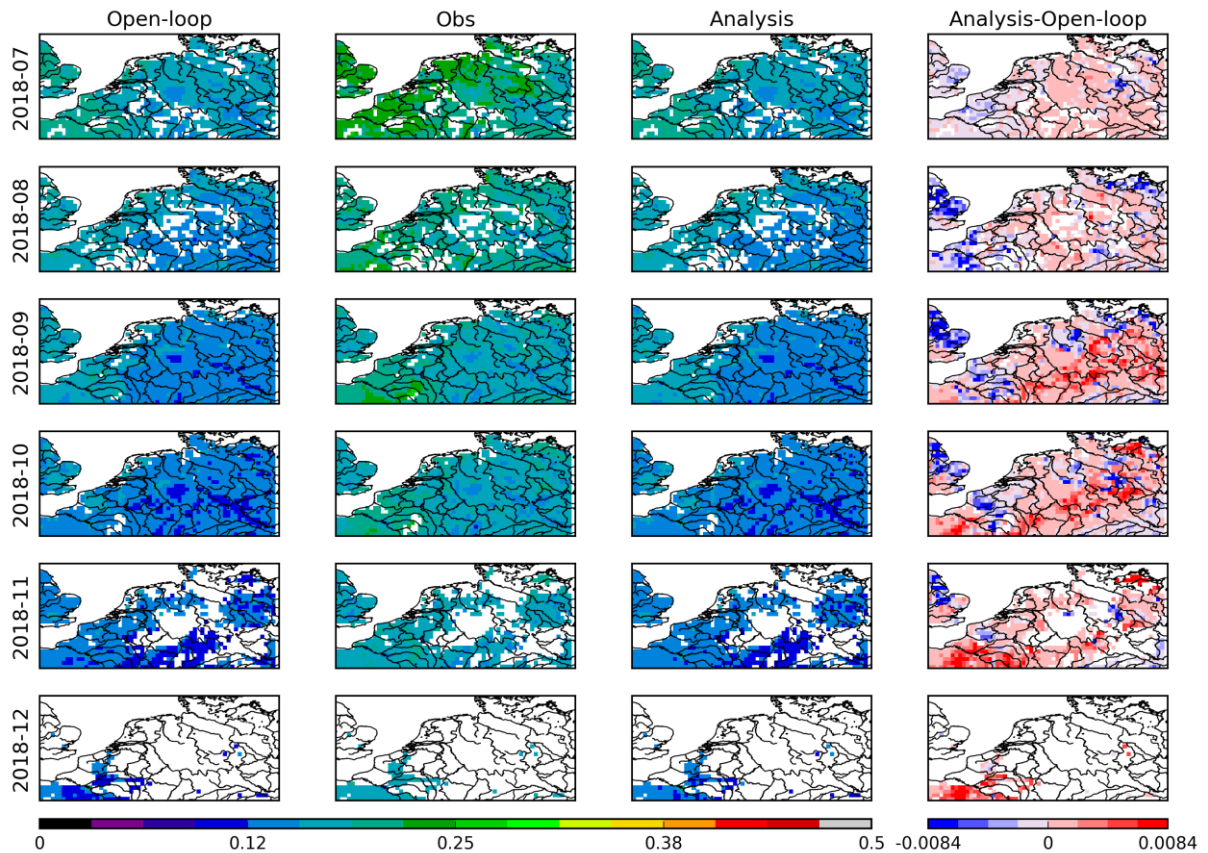


Figure 20: Monthly average values of Surface Albedo over Western Europe at 0.25° spatial resolution from July (top) to December 2018 (bottom). From left to right: model, satellite product, analysis, analysis-model difference. The latter shows the impact of assimilating LAI and SWI-001 on the simulated SA. The color scale range of SA values is 0 to 0.5.

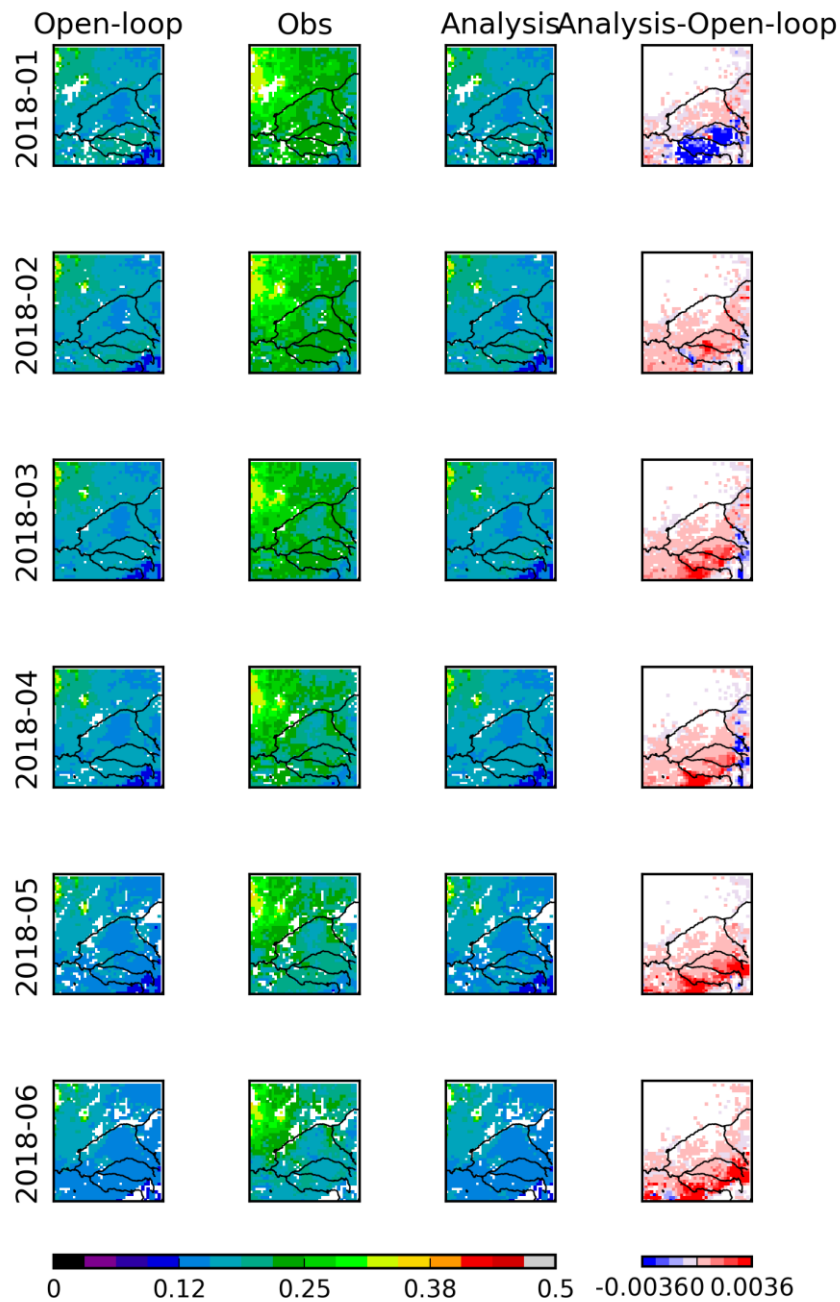


Figure 21: Monthly average values of Surface albedo over the Murray-Darling basin at 0.25° spatial resolution from January (top) to June 2018 (bottom). From left to right: model, satellite product, analysis, analysis-model difference. The latter shows the impact of assimilating LAI and SWI-001 on the simulated SA. The color scale range of SA values is 0 to 0.5.

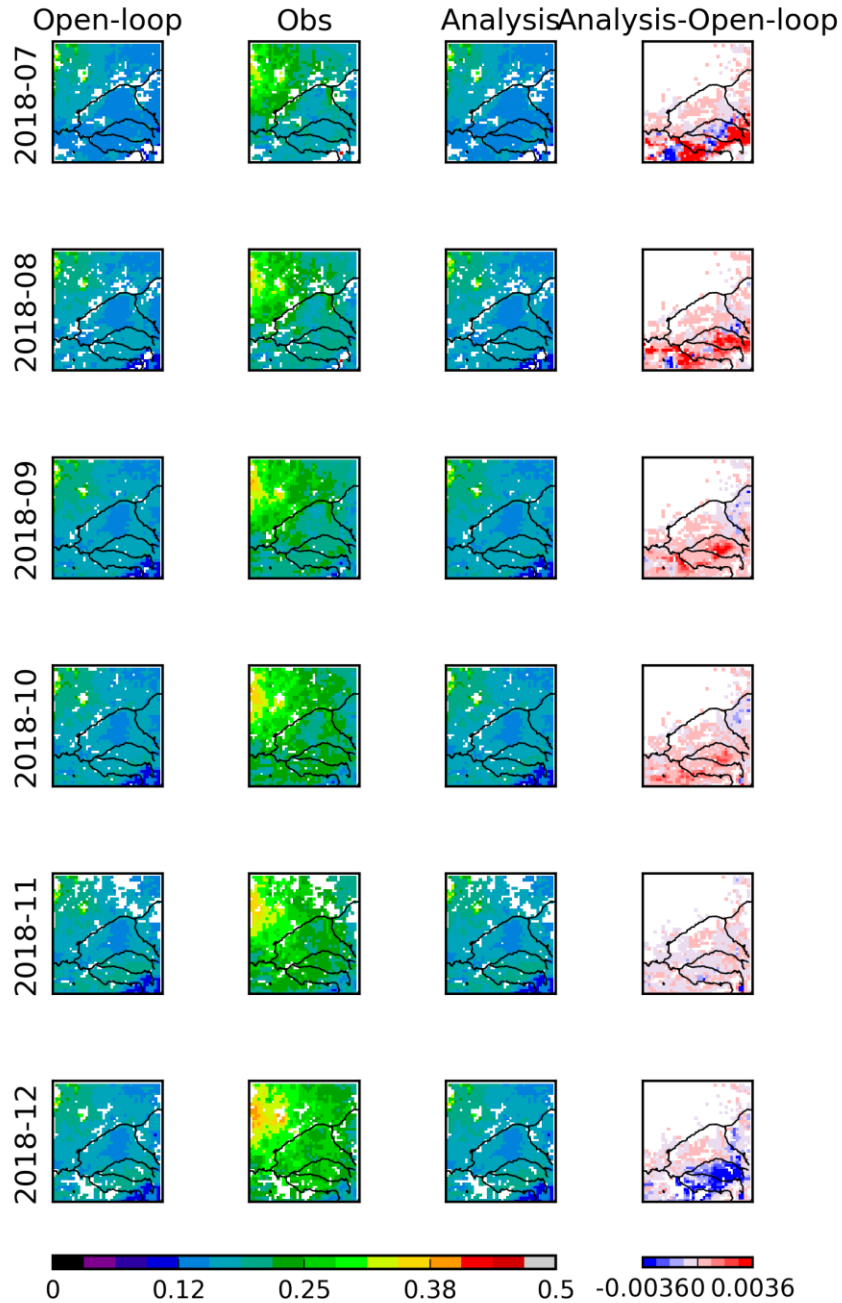


Figure 22: Monthly average values of Surface albedo over the Murray-Darling basin at 0.25° spatial resolution from July (top) to December 2018 (bottom). From left to right: model, satellite product, analysis, analysis-model difference. The latter shows the impact of assimilating LAI and SWI-001 on the simulated SA. The color scale range of SA values is 0 to 0.5.

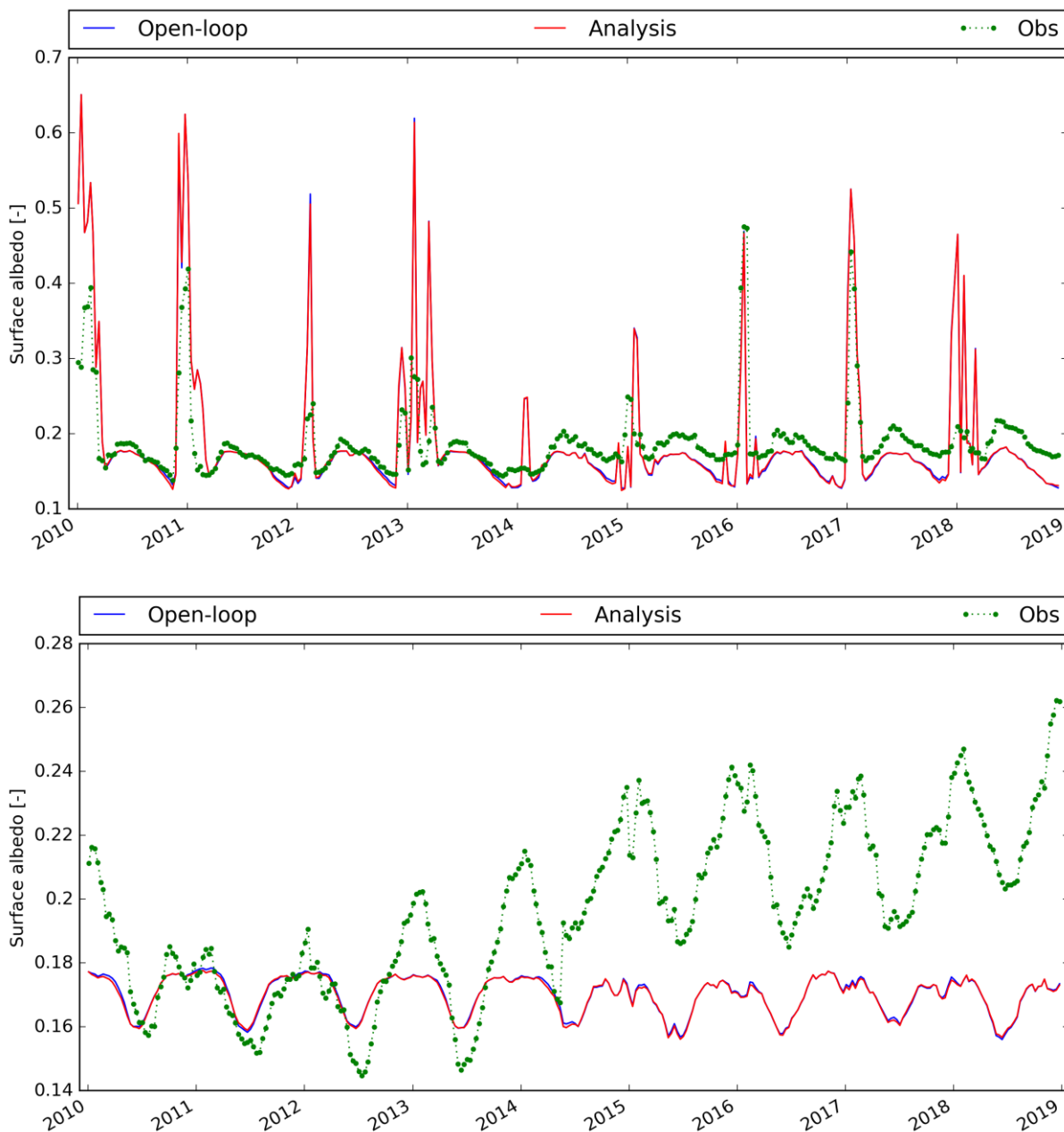
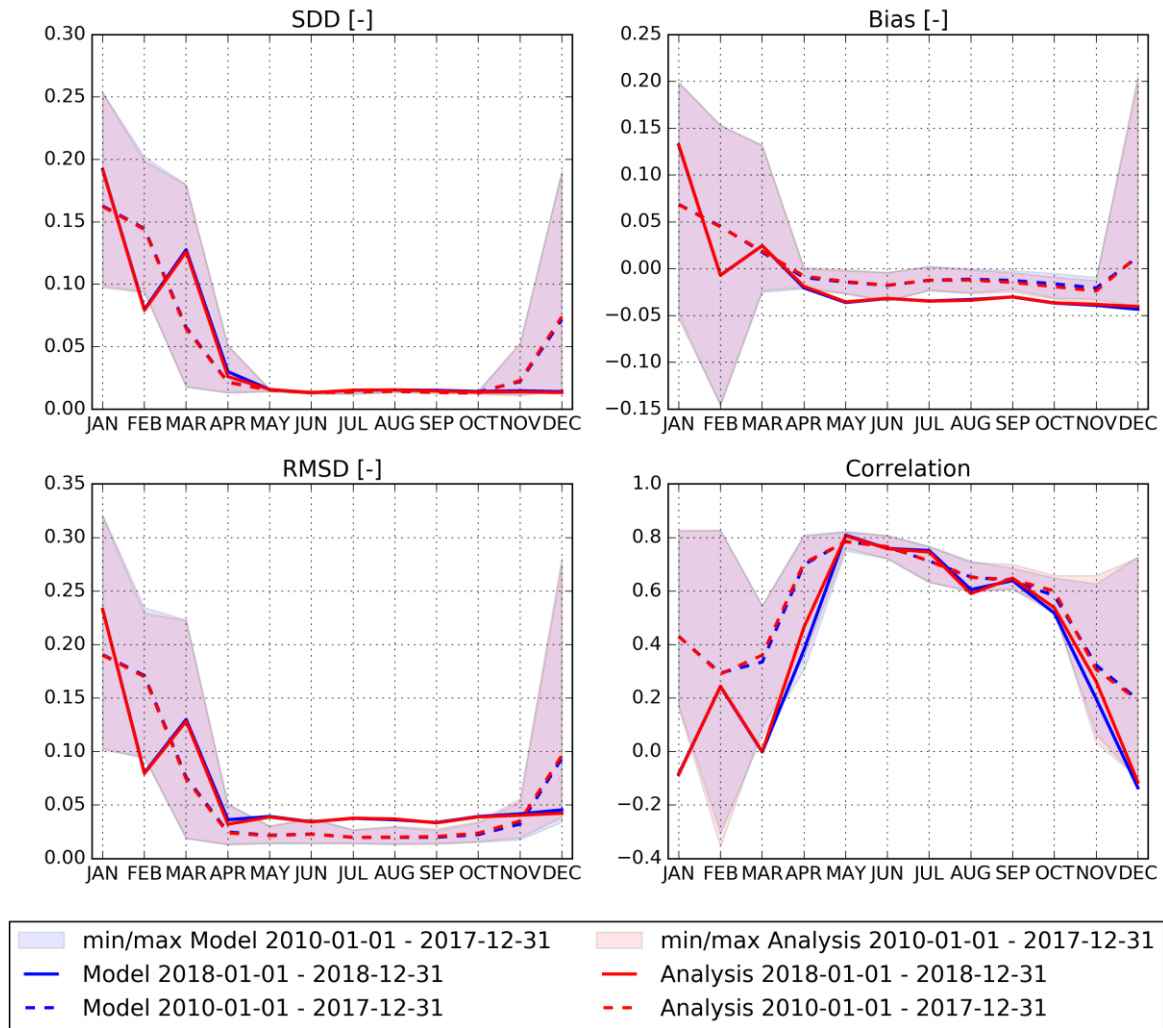
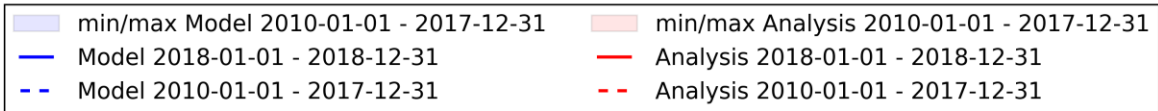
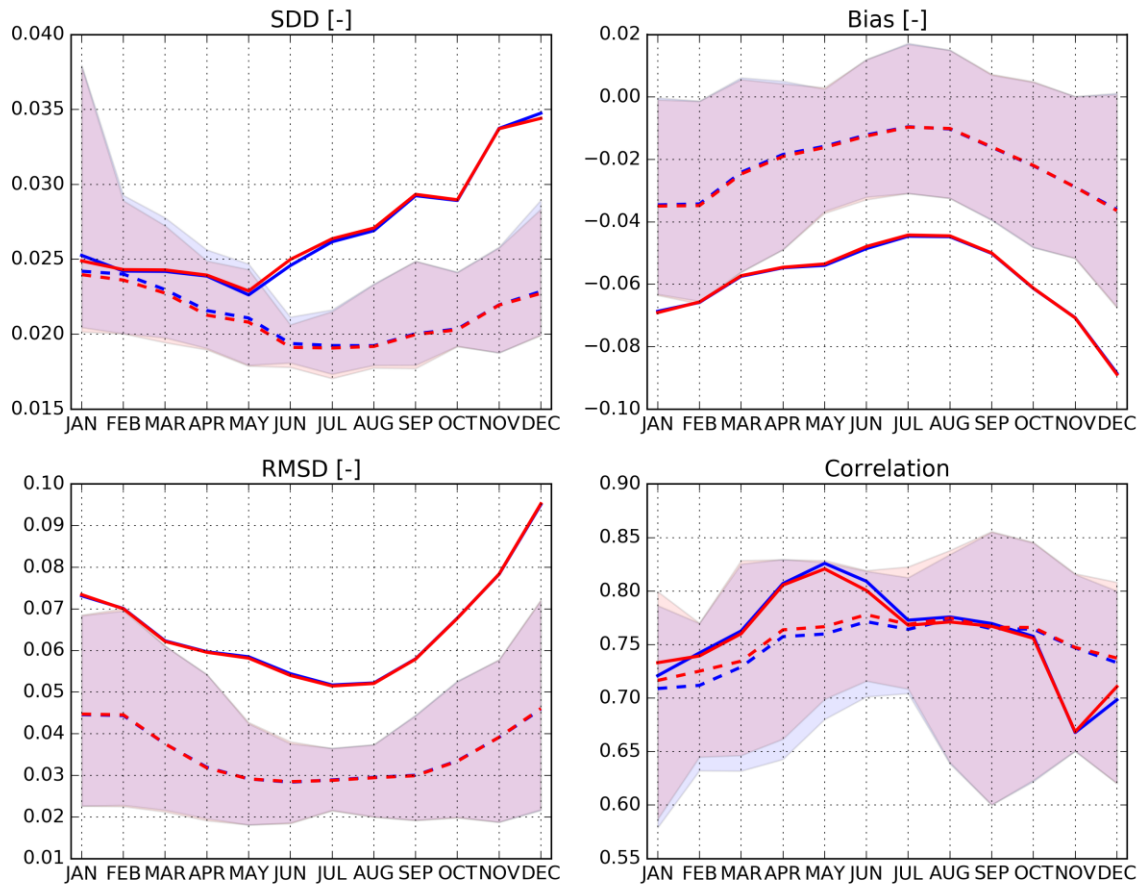


Figure 23: Monthly average values of SA over Western Europe (top) from 2010 to 2018, the Murray-Darling basin (bottom) from 2010 to 2018: model (blue line), satellite product (green circles), analysis (red line). Analysis-Model differences show the impact of assimilating LAI and SWI-001 on the simulated SA. (Note that spikes in Western Europe correspond to extensive snowfalls. In the analysis, the snow-free seasonal variability is triggered by changes in the fractional cover of crops related to LAI. Model and analysis curves are often superimposed).



	JAN	FEB	MAR	APR	MAY	JUN	JUL	AUG	SEP	OCT	NOV	DEC	min	max
2010-01-01 - 2017-12-31	7255	15665	25719	25888	23348	22490	21889	19717	22131	24650	16490	7442	7255	25888
2018-01-01 - 2018-12-31	55	1283	2098	3363	2652	2302	1962	1808	3168	3472	1826	130	55	3472

Figure 24: Monthly SA scores of the model (blue) and analysis (red) when compared to the observations over Western Europe at a 0.25° spatial resolution: from 2010 to 2017 (dashed lines), with N ranging from 7255 in January to 258,888 in April; and for January to December 2018 (solid lines), with N ranging from 55 in January to 3,472 in October. The monthly N values are indicated in the legend Table. Analysis-Model differences show the impact of assimilating LAI and SWI-001 on the simulated SA. (Note that model and analysis curves are often superimposed).



	JAN	FEB	MAR	APR	MAY	JUN	JUL	AUG	SEP	OCT	NOV	DEC	min	max
2010-01-01 - 2017-12-31	33581	34715	36612	38153	37538	37950	37478	37756	37404	36671	33757	32985	32985	38153
2018-01-01 - 2018-12-31	4023	4632	4797	4554	3990	3997	3956	3865	4531	4316	3472	3718	3472	4797

Figure 25: Monthly SA scores of the model (blue) and analysis (red) when compared to the observations over the Murray-Darling basin at 0.25° spatial resolution: from 2010 to 2017 (dashed lines), with N ranging from 32,985 in December to 38,153 in April; and for January to December 2018 (solid lines), with N ranging from 3,472 in November to 4,797 in March. The monthly N values are indicated in the legend Table. Analysis-Model differences show the impact of assimilating LAI and SWI-001 on the simulated SA. (Note that model and analysis curves are often superimposed).

Table 5: Model and analysis SA scores from 2010 to 2017 and for 2018 over Western Europe (top), the Murray-Darling basin (bottom). Analysis-Model differences show the impact of assimilating LAI and SWI-001 on the simulated SA.

	Version	Bias	Correlation	RMSD	SDD	Nb_pts
2010-01-01 - 2017-12-31	Model	0.000	0.603	0.072	0.072	232684
2010-01-01 - 2017-12-31	Analysis	-0.000	0.604	0.072	0.072	232684
2018-01-01 - 2018-12-31	Model	-0.026	0.268	0.056	0.050	24119
2018-01-01 - 2018-12-31	Analysis	-0.025	0.272	0.055	0.049	24119

	Version	Bias	Correlation	RMSD	SDD	Nb_pts
2010-01-01 - 2017-12-31	Model	-0.018	0.610	0.036	0.031	434600
2010-01-01 - 2017-12-31	Analysis	-0.018	0.613	0.036	0.030	434600
2018-01-01 - 2018-12-31	Model	-0.059	0.753	0.066	0.030	49851
2018-01-01 - 2018-12-31	Analysis	-0.059	0.750	0.066	0.030	49851

Conclusion for Surface Albedo:

Contrary to LAI and FAPAR, the SA scores in 2018 do not always present better values than during the 2010-2017 reference period of time. Particularly large SDD values are observed over the Murray-Darling basin from June to December 2018 (Figure 25). Table 5 indicates that in 2018 SDD and RMSD scores are worse (better) over the Murray-Darling basin (Western Europe), while correlation is better (worse). The bias is also much more pronounced in 2018, especially over the Murray-Darling basin (Table 5, Figure 25). This can be at least partly attributed to the transition between SPOT-VGT and PROBA-V in 2014. A discontinuity in mean observed SA values is clearly visible in May 2014, when data from SPOT-VGT were replaced by data from PROBA-V (Figure 23). The SA values tend to present higher values after this date (see Section 9.2 for a detailed comparison).

Over the Murray-Darling basin, the marked decrease in LAI values from 2016 to 2018 (Figure 9) corresponds to a marked increase in SA (Figure 23). However, the assimilation tends to reduce SA values in the southwestern part of the area in January and December (Figures 21 and 22, respectively), while LAI is reduced (Figures 6 and 7, respectively) and SSM is increased (Figures 28 and 29, respectively). Decreasing SA values in browning areas could be related to increasing SSM. The same type of response of the simulated SA to the assimilation is observed over Western Europe from August to November 2018 (Figure 20 to be compared with Figure 5 for LAI, and to Figure 27 for SSM, mainly over eastern England and northern France).

The number of SA observations (Table 5) is smaller than for LAI and FAPAR (Table 4). In 2018, N for SA is 35% and 20% smaller than N for FAPAR over Western Europe and the Murray-Darling basin, respectively. For example, only 55 SA observations are available over Western Europe in January, against 657 for FAPAR.

7 RESULTS FOR SWI-001

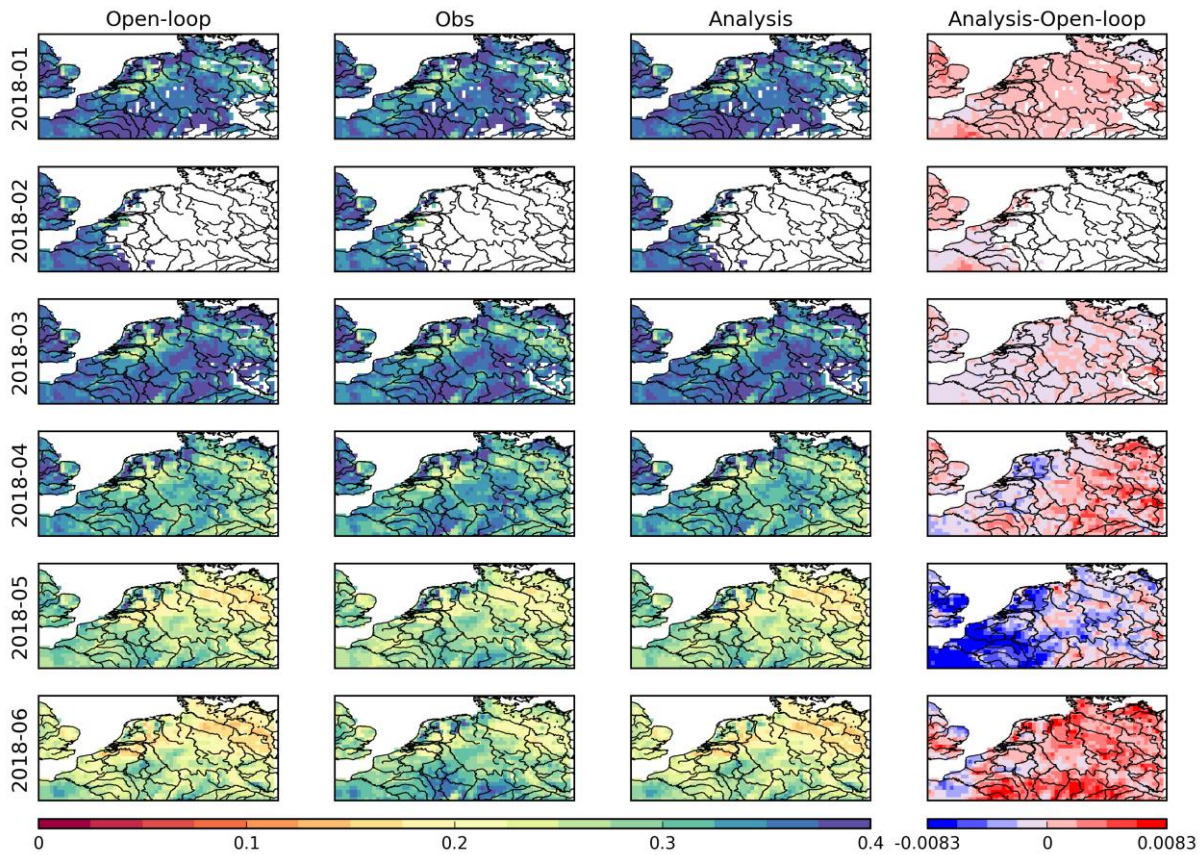


Figure 26: Monthly average values of SSM over Western Europe at 0.25° spatial resolution from January (top) to June 2018 (bottom). From left to right: model, rescaled satellite product after CDF matching, analysis, analysis-model difference. The latter shows the impact of assimilating LAI and SWI-001 on the simulated SSM. The color scale range of SSM values is 0 to 0.4 m³ m⁻³.

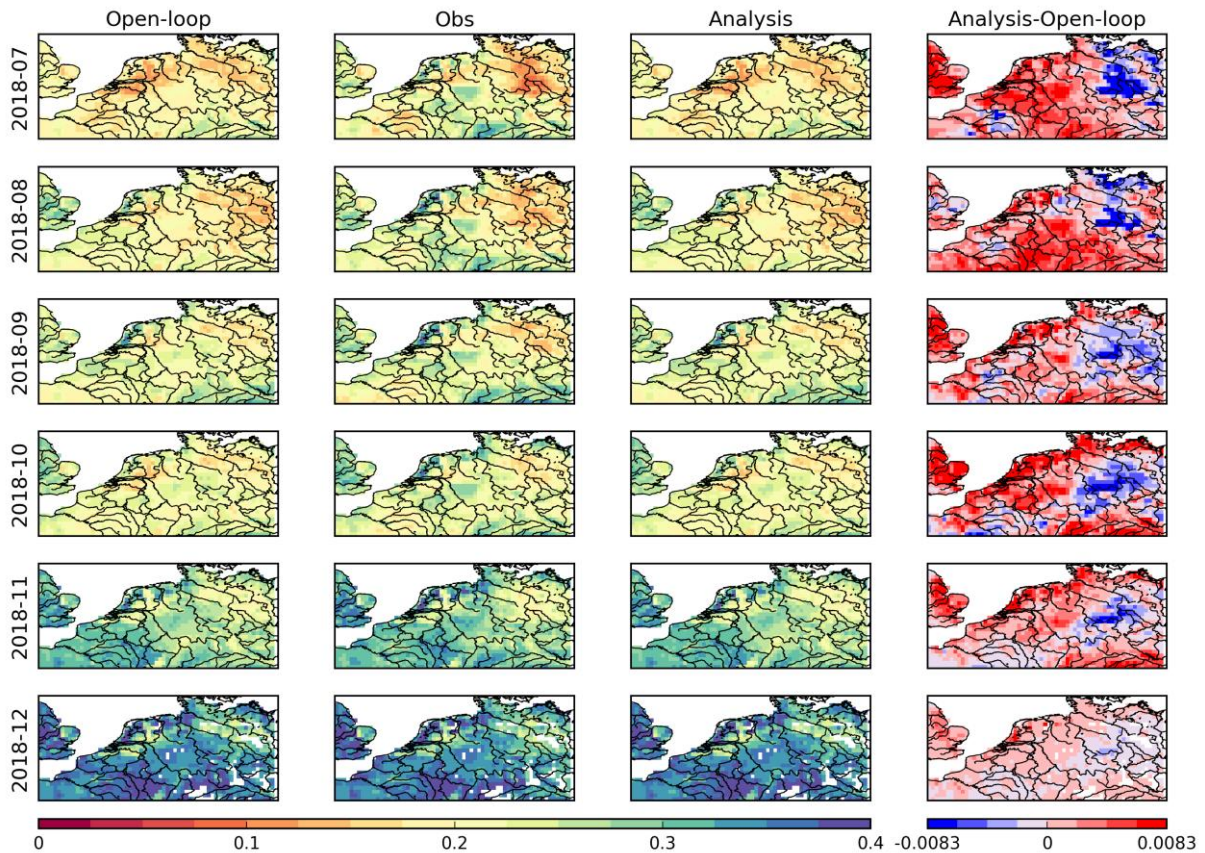


Figure 27: Monthly average values of SSM over Western Europe at 0.25° spatial resolution from July (top) to December 2018 (bottom). From left to right: model, rescaled satellite product after CDF matching, analysis, analysis-model difference. The latter shows the impact of assimilating LAI and SWI-001 on the simulated SSM. The color scale range of SSM values is 0 to 0.4 m³m⁻³.

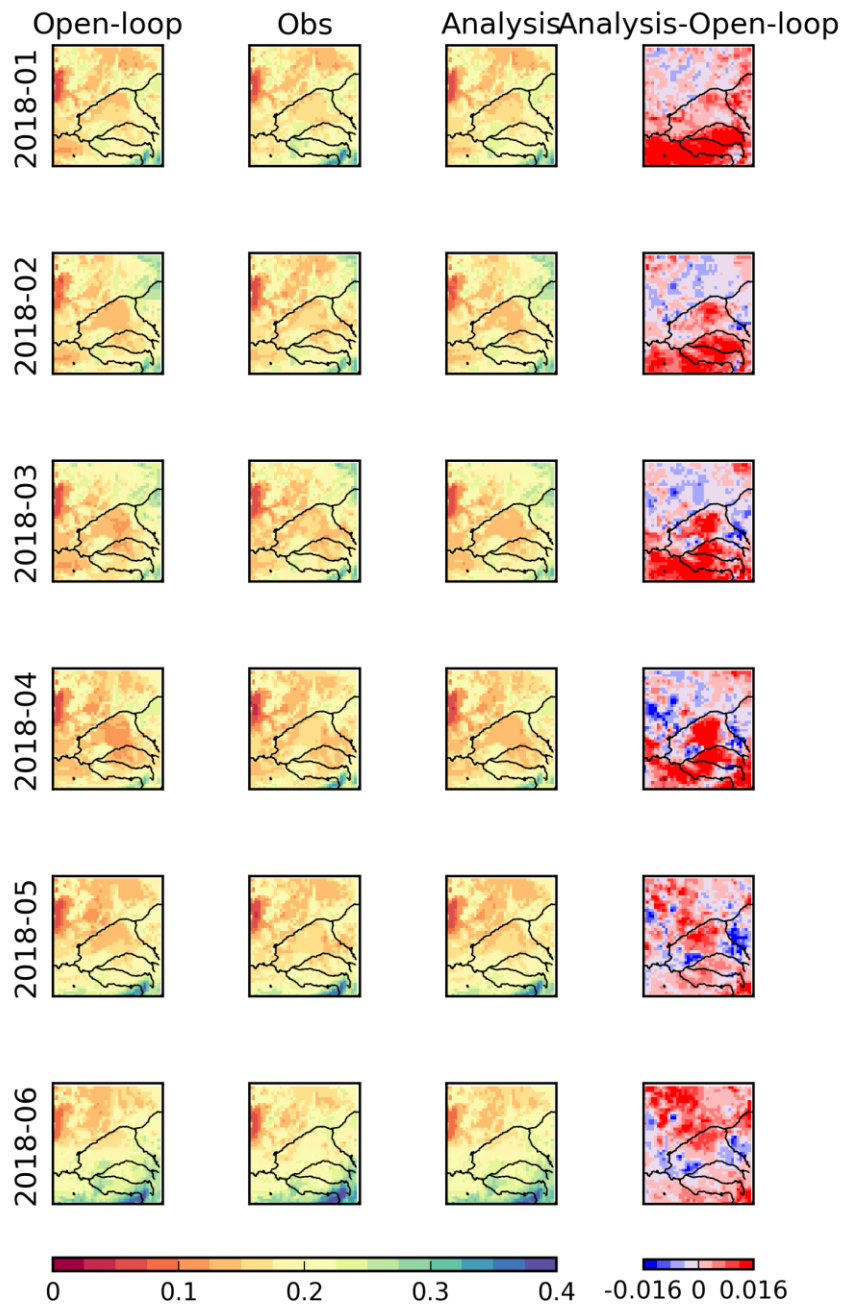


Figure 28: Monthly average values of SSM over the Murray-Darling basin at 0.25° spatial resolution from January (top) to June 2018 (bottom). From left to right: model, rescaled satellite product after CDF matching, analysis, analysis-model difference. The latter shows the impact of assimilating LAI and SWI-001 on the simulated SSM. The color scale range of SSM values is 0 to 0.4 m³ m⁻³.

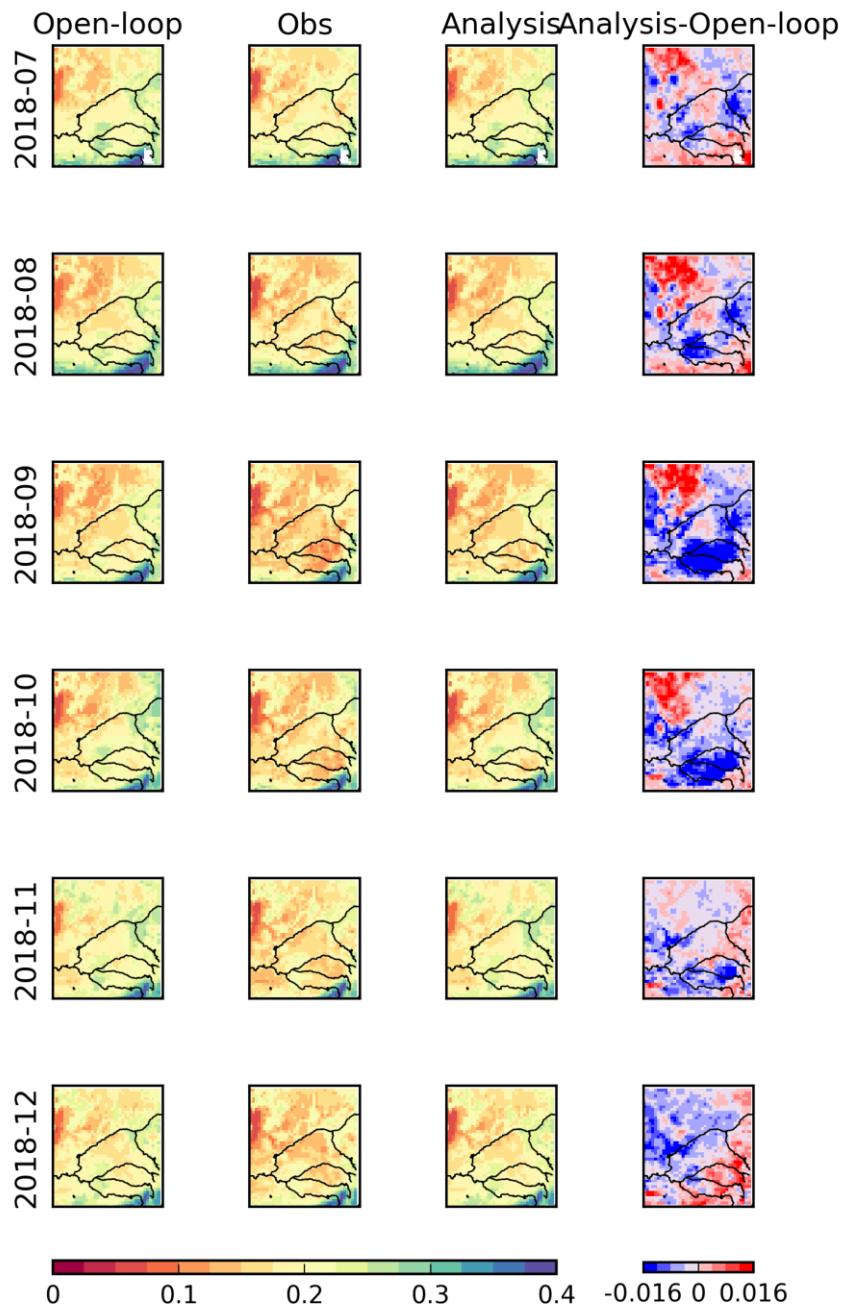


Figure 29: Monthly average values of SSM over the Murray-Darling basin at 0.25° spatial resolution from July (top) to December 2018 (bottom). From left to right: model, rescaled satellite product after CDF matching, analysis, analysis-model difference. The latter shows the impact of assimilating LAI and SWI-001 on the simulated SSM. The color scale range of SSM values is 0 to 0.4 m³m⁻³.

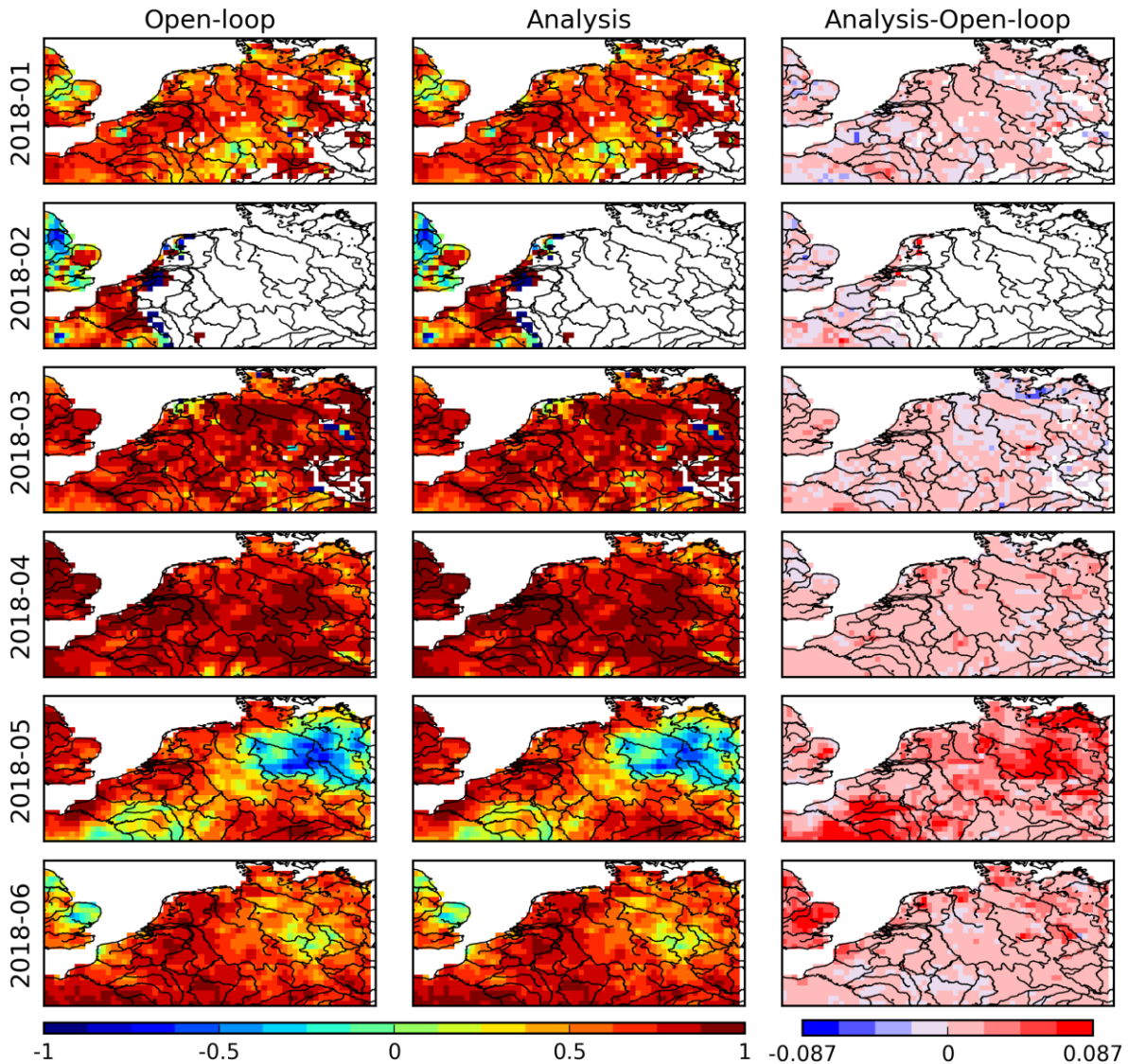


Figure 30: Monthly correlation maps between the rescaled SWI-001 product time series after CDF matching and the modeled SSM (left), and the analyzed SSM (middle) over Western Europe at 0.25° spatial resolution from January (top) to June 2018 (bottom). Analysis-Model differences show the impact of assimilating LAI and SWI-001 on the simulated SSM. The color scale range of R values is -1.0 to 1.0. Areas with missing data are left blank.

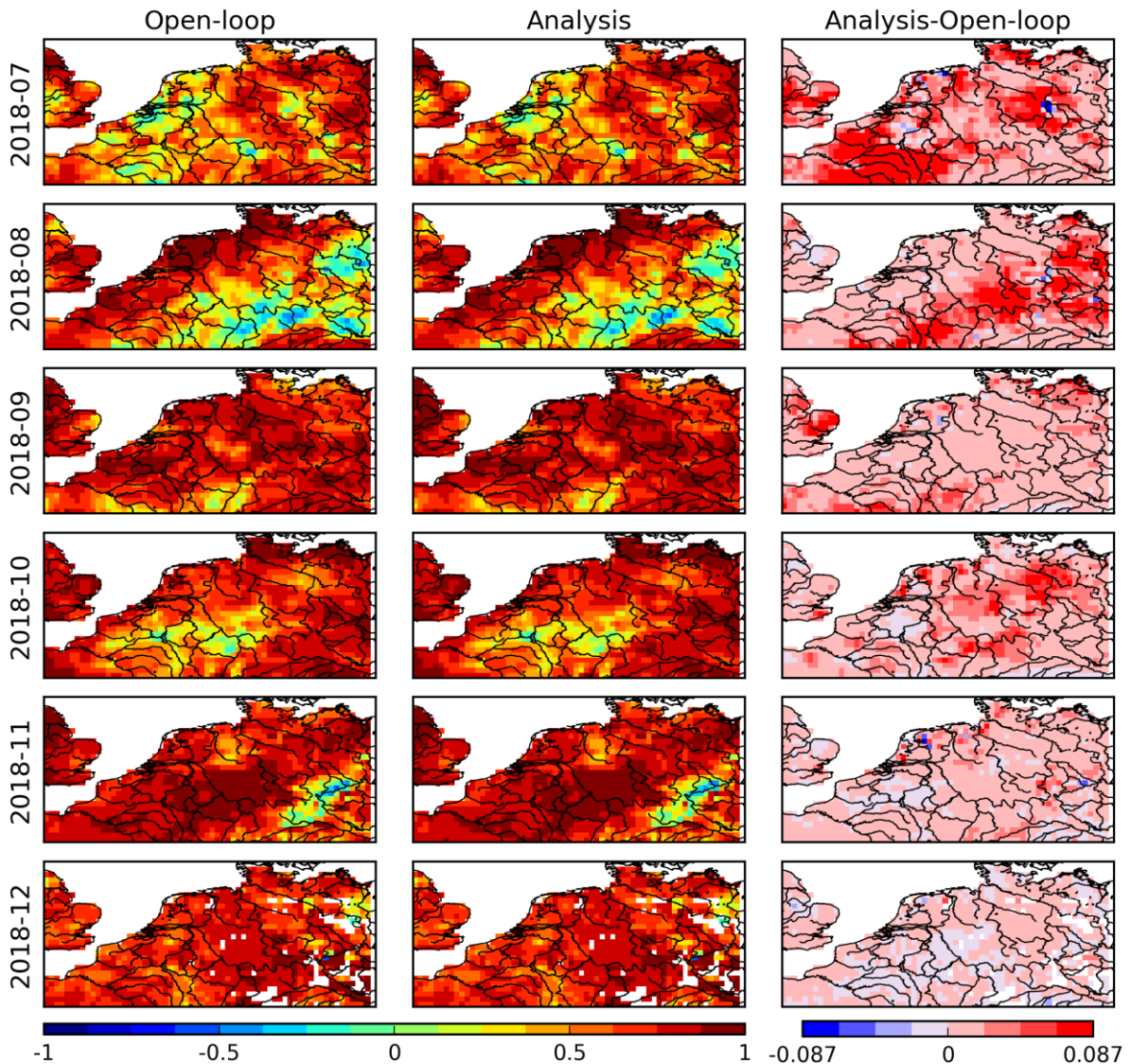


Figure 31: Monthly correlation maps between the rescaled SWI-001 product time series after CDF matching and the modeled SSM (left), and the analyzed SSM (middle) over Western Europe at 0.25° spatial resolution from July (top) to December 2018 (bottom). Analysis-Model differences show the impact of assimilating LAI and SWI-001 on the simulated SSM. The color scale range of R values is -1.0 to 1.0.

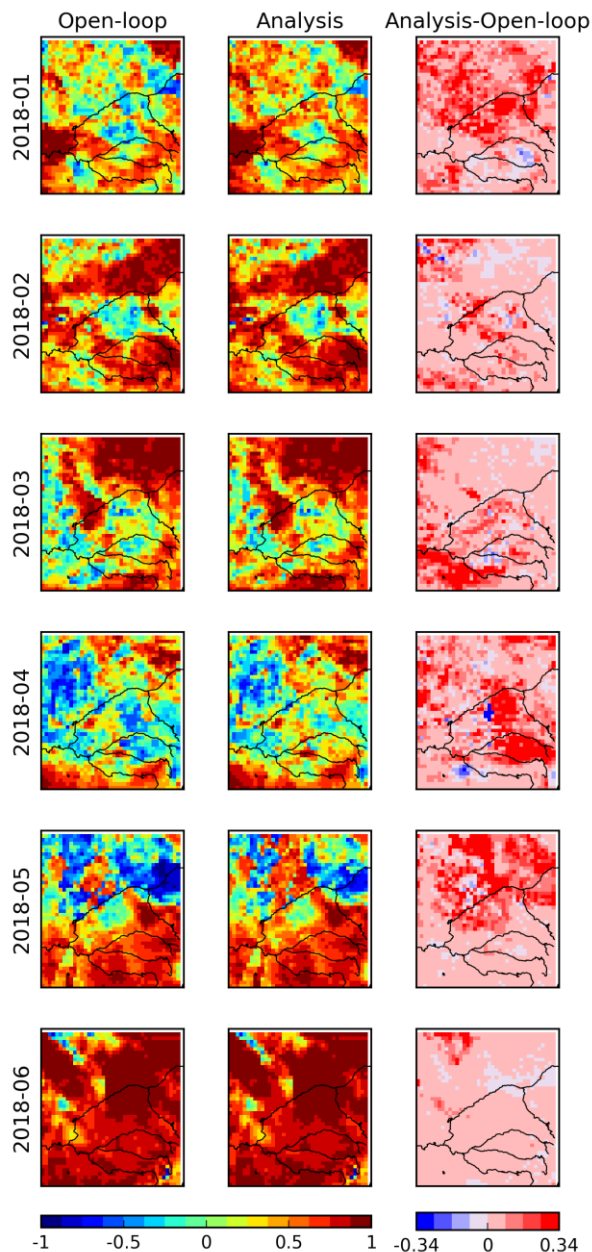


Figure 32: Monthly correlation maps between the rescaled SWI-001 product time series after CDF matching and the modeled SSM (left), and the analyzed SSM (middle) over the Murray-Darling basin at 0.25° spatial resolution from January (top) to June 2018 (bottom). Analysis-Model differences show the impact of assimilating LAI and SWI-001 on the simulated SSM. The color scale range of R values is -1.0 to 1.0.

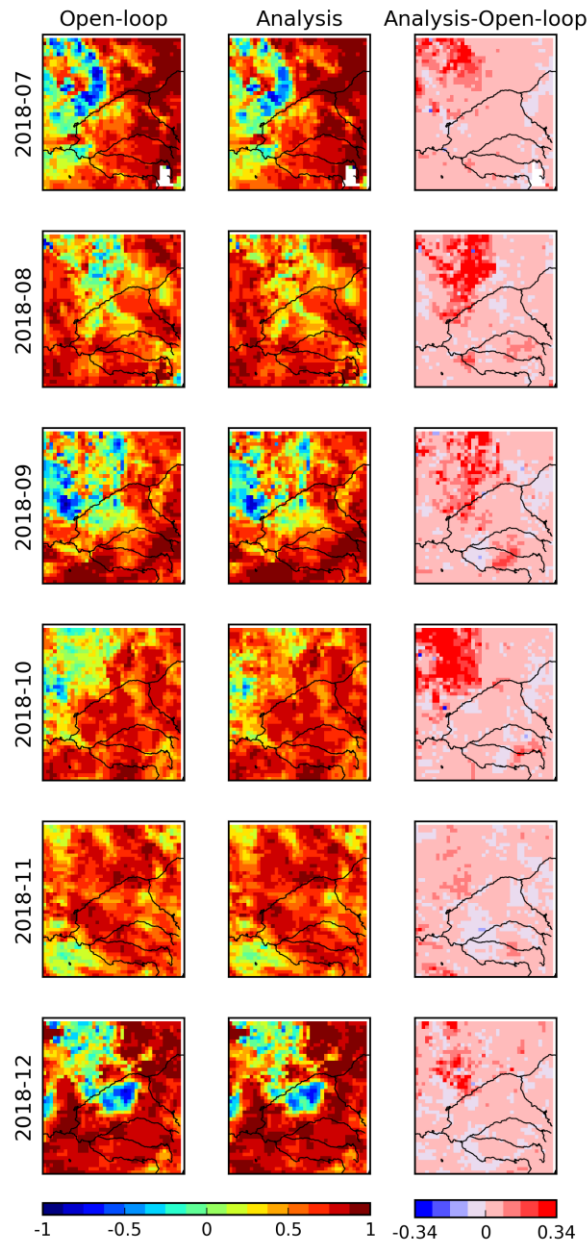


Figure 33: Monthly correlation maps between the rescaled SWI-001 product time series after CDF matching and the modeled SSM (left), and the analyzed SSM (middle) over the Murray-Darling basin at 0.25° spatial resolution from July (top) to December 2018 (bottom). Analysis-Model differences show the impact of assimilating LAI and SWI-001 on the simulated SSM. The color scale range of R values is -1.0 to 1.0.

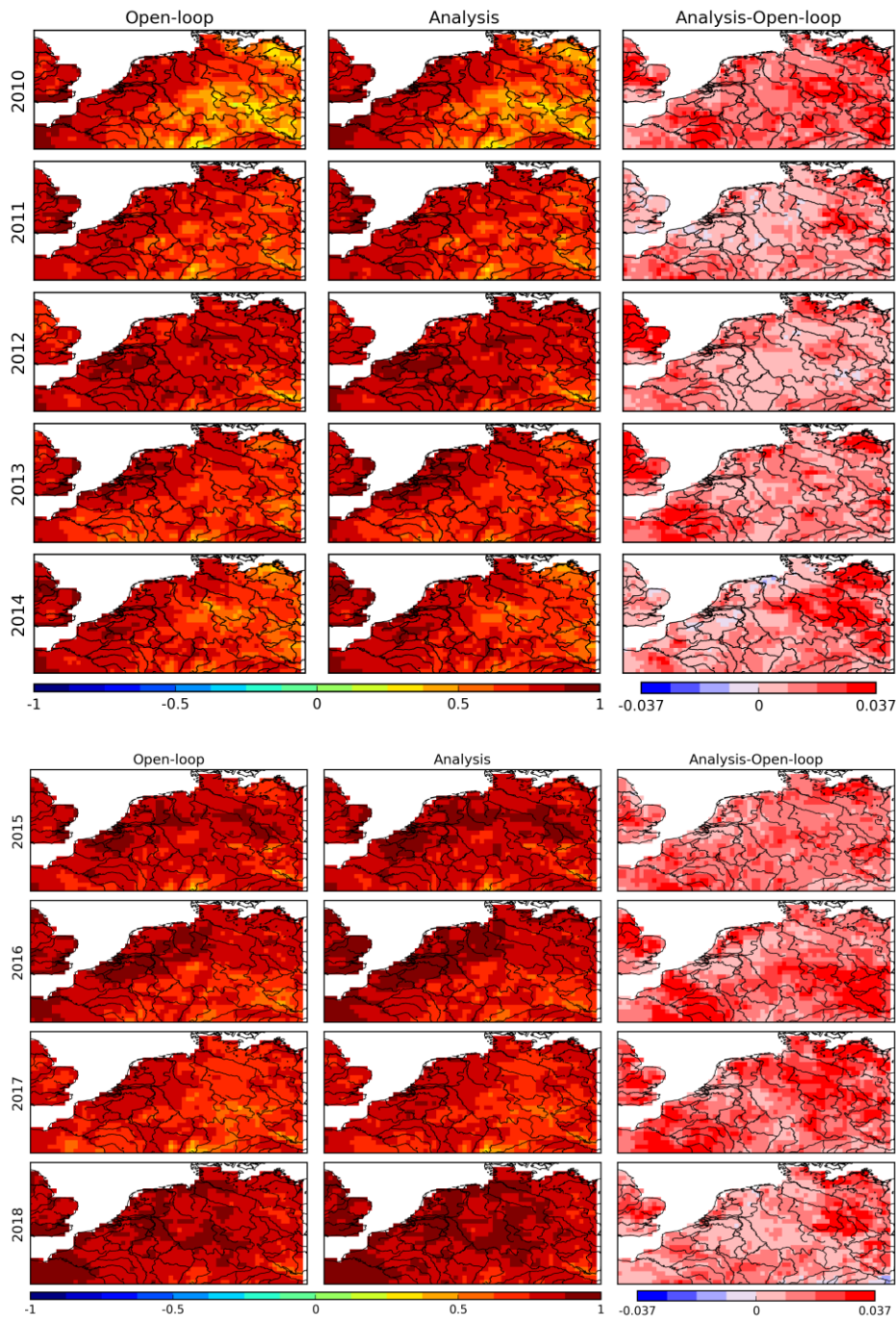


Figure 34: Yearly correlation maps between the rescaled SWI-001 product time series after CDF matching and the modeled SSM (left), and the analyzed SSM (middle) over Western Europe at 0.25° resolution from 2010 to 2018. Analysis-Model differences show the impact of assimilating LAI and SWI-001 on the simulated SSM. The color scale range of R values is -1.0 to 1.0.

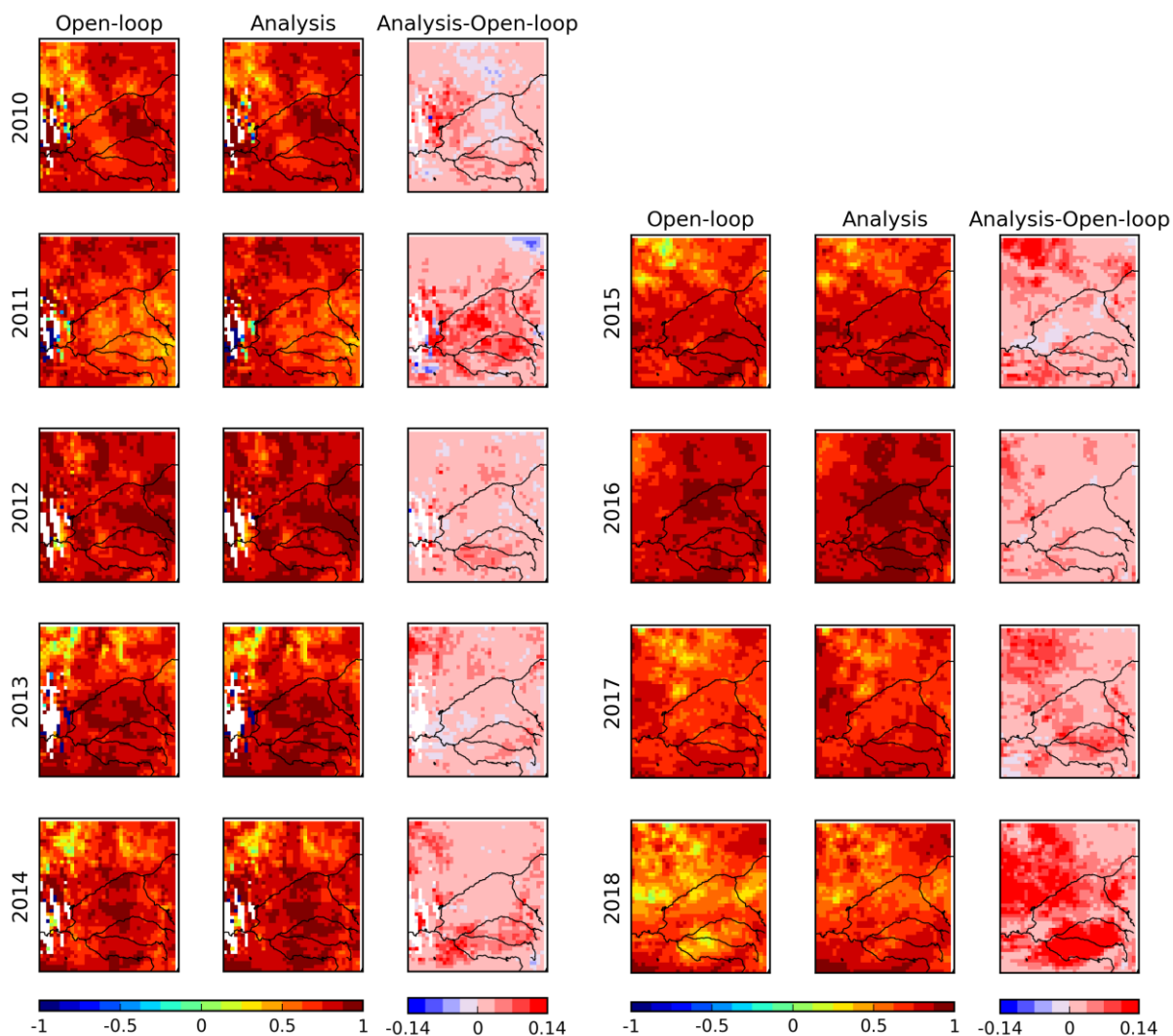


Figure 35: Yearly correlation maps between the rescaled SWI-001 product time series after CDF matching and the modeled SSM (left), and the analyzed SSM (middle) over the Murray-Darling basin at 0.25° resolution from 2010 to 2018. Analysis-Model differences show the impact of assimilating LAI and SWI-001 on the simulated SSM. The color scale range of R values is -1.0 to 1.0.

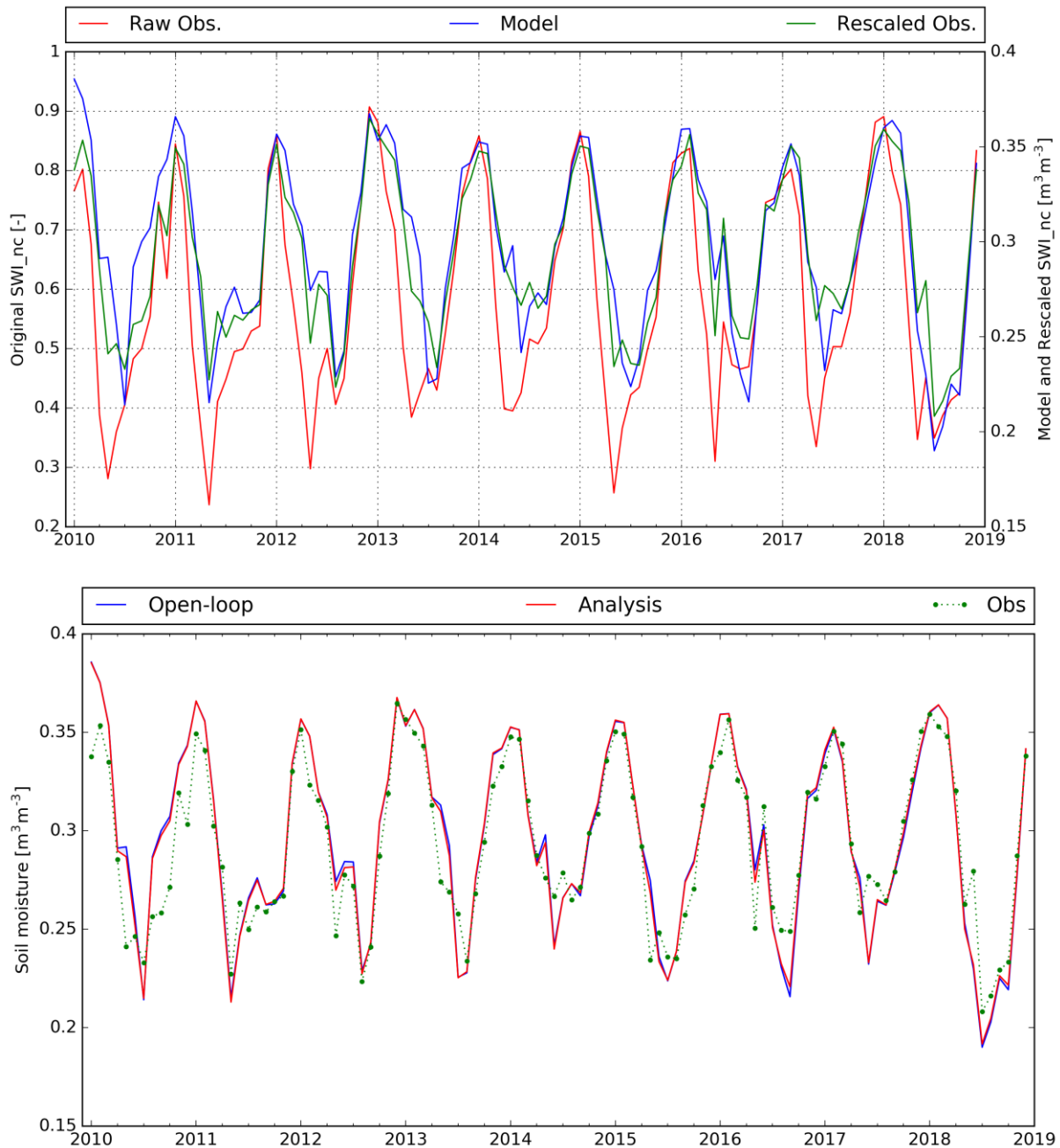


Figure 36: Monthly average values of SSM over Western Europe from 2010 to 2018. Top panel: original SWI-001 (red), model SSM used for CDF-matching (blue), rescaled SWI-001 product (green). Bottom panel: model (blue, same as on the top graph), rescaled SWI-001 observations (green), analysis (red). Analysis-Model differences show the impact of assimilating LAI and SWI-001 on the simulated SSM.

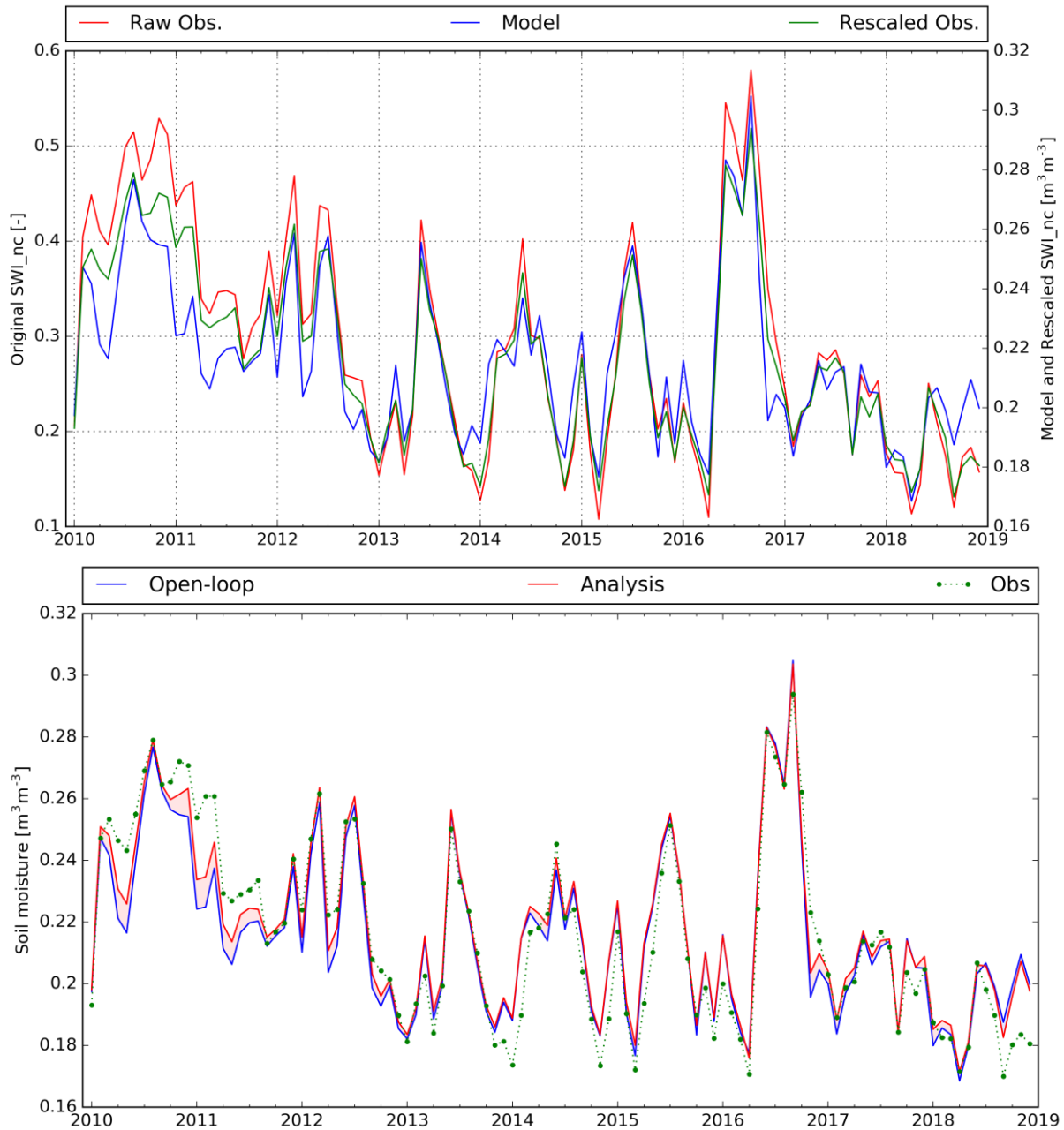
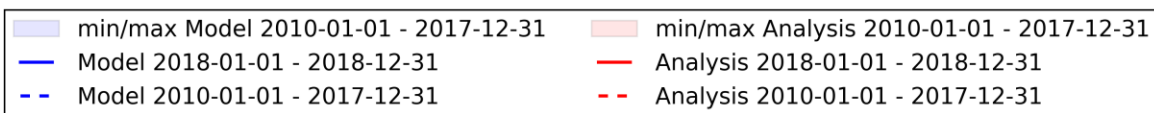
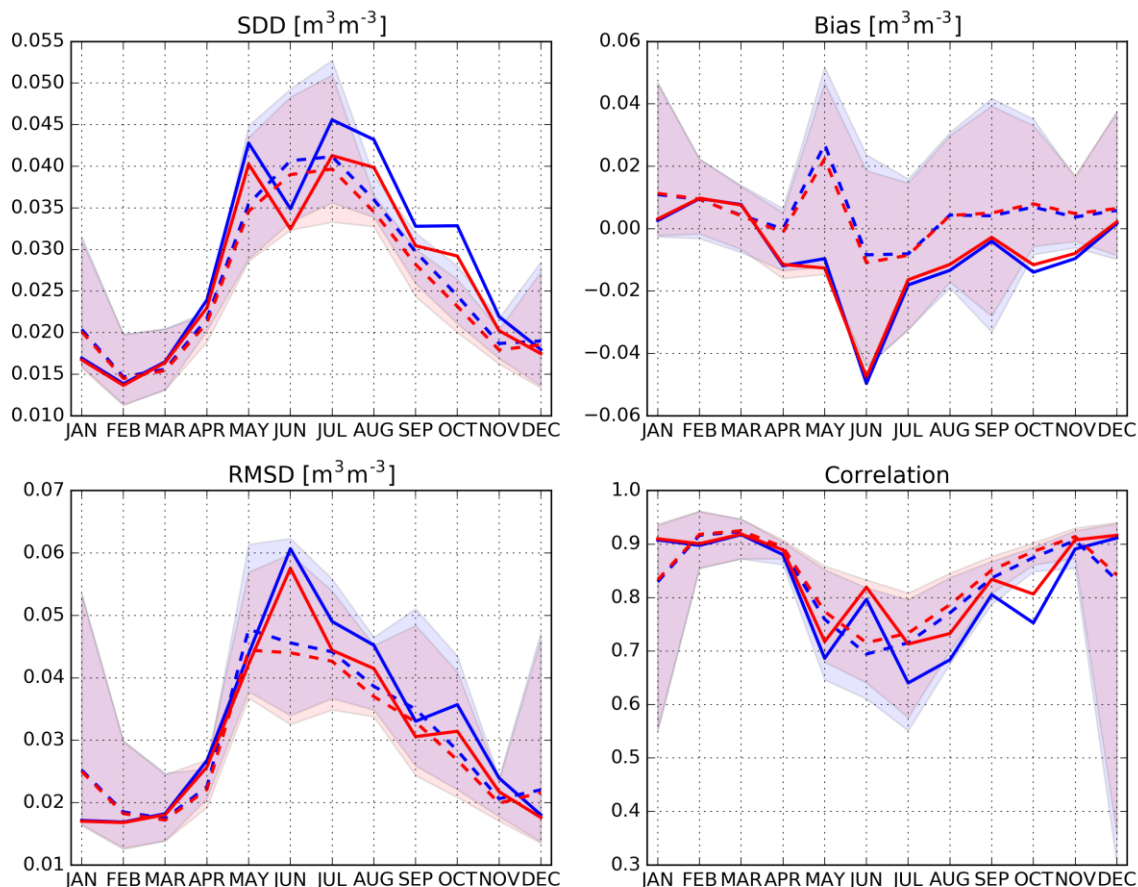
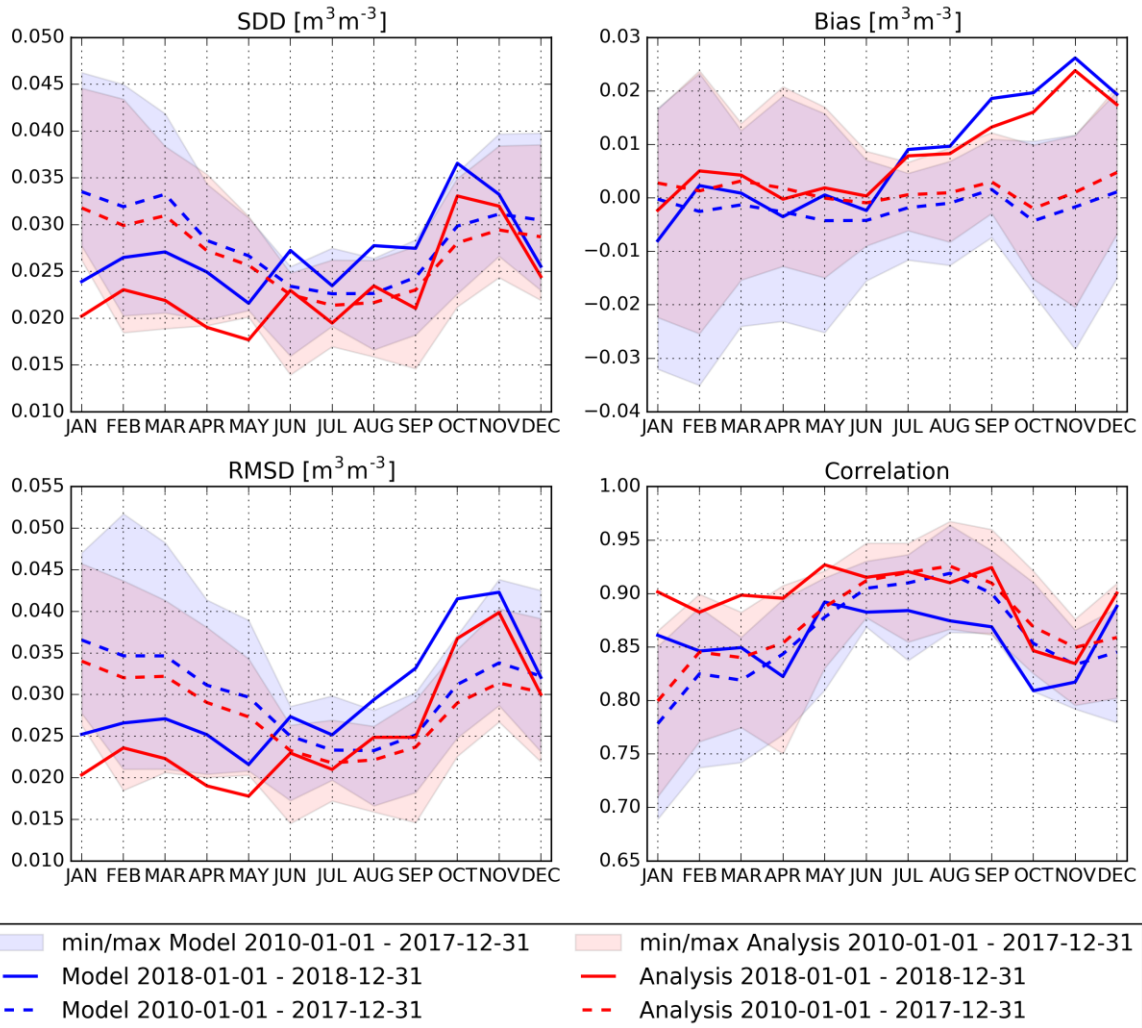


Figure 37: Monthly average values of SSM over the Murray-Darling basin from 2010 to 2018. Top panel: original SWI-001 (red), model SSM used for CDF-matching (blue), rescaled SWI-001 product (green). Bottom panel: model (blue, same as on the top graph), rescaled SWI-001 observations (green), analysis (red). Analysis-Model differences show the impact of assimilating LAI and SWI-001 on the simulated SSM.



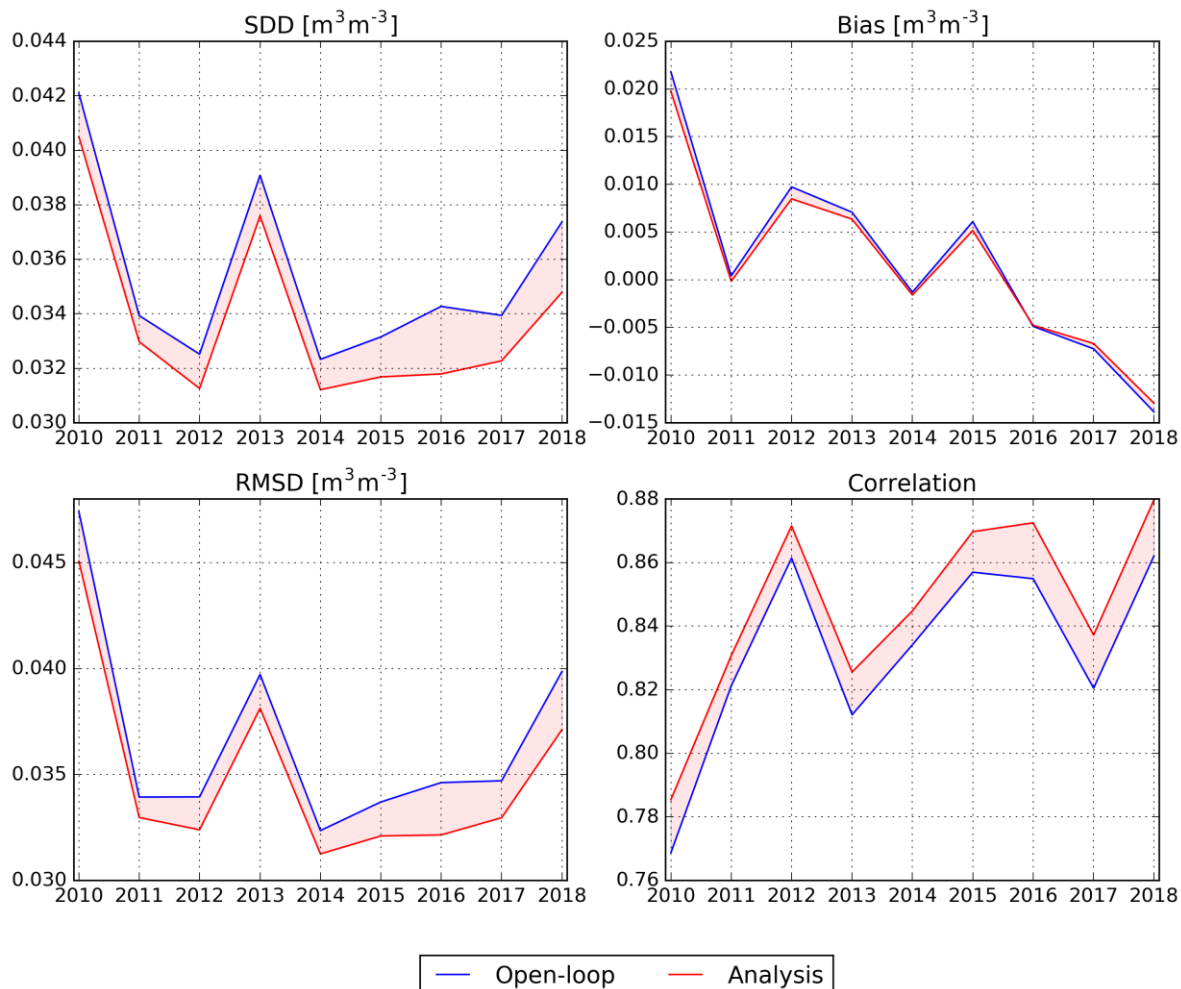
	JAN	FEB	MAR	APR	MAY	JUN	JUL	AUG	SEP	OCT	NOV	DEC	min	max
2010-01-01 - 2017-12-31	39163	42697	87316	148431	213040	216892	233025	244876	232816	219850	150352	78278	39163	244876
2018-01-01 - 2018-12-31	17089	1530	12693	36238	41470	40559	41868	41554	39280	40107	24286	18387	1530	41868

Figure 38: Monthly SSM scores of the model (blue) and analysis (red) when compared to the rescaled SWI-001 over Western Europe at 0.25° spatial resolution: for all data from 2010 to 2017 (dashed lines), with N ranging from 39,163 in January to 2,448,876 in August, and for data in 2018 (solid lines), with N ranging from 1,530 in February to 41,868 in July. The monthly N values are indicated in the legend Table. Analysis-Model differences show the impact of assimilating LAI and SWI-001 on the simulated SSM. Shaded areas are between minimum and maximum score values recorded from 2010 to 2017.



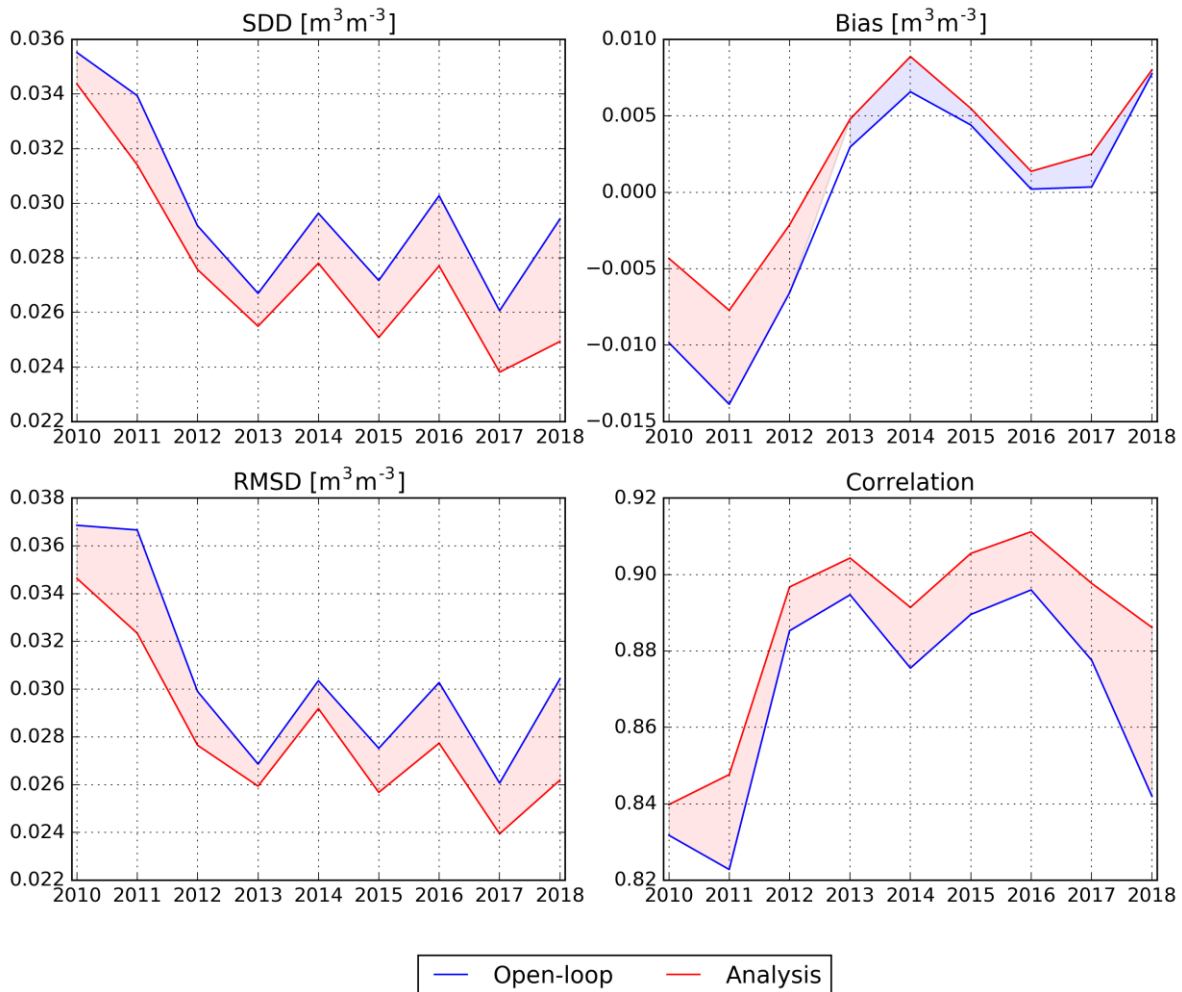
	JAN	FEB	MAR	APR	MAY	JUN	JUL	AUG	SEP	OCT	NOV	DEC	min	max
2010-01-01 - 2017-12-31	127201	118513	131833	124113	123056	119196	129428	158756	162965	168797	169957	164721	118513	169957
2018-01-01 - 2018-12-31	43993	39454	43971	43091	42614	40767	41178	42385	42468	44720	42153	44250	39454	44720

Figure 39: Monthly scores of the model (blue) and analysis (red) when compared to the rescaled SWI-001 over the Murray-Darling basin at 0.25° spatial resolution: for all data from 2010 to 2017 (dashed lines), with N ranging from 118,513 in February to 169,957 in November, and for data in 2018 (solid lines), with N ranging from 39,454 in February to 44,720 in October. The monthly N values are indicated in the legend Table. Analysis-Model differences show the impact of assimilating LAI and SWI-001 on the simulated SSM. Shaded areas are between minimum and maximum score values recorded from 2010 to 2017.



2010	164456
2011	188508
2012	195031
2013	182596
2014	205216
2015	279547
2016	343779
2017	347603
2018	355061
min	164456
max	355061

Figure 40: Annual scores of the model (blue) and analysis (red) when compared to the rescaled SWI-001 over Western Europe at 0.25° spatial resolution, with N ranging from 164,456 in 2010 to 355,061 in 2018. The yearly N values are indicated in the legend Table. Analysis-Model differences show the impact of assimilating LAI and SWI-001 on the simulated SSM.



— Open-loop — Analysis

2010	85972
2011	85439
2012	83612
2013	84304
2014	82588
2015	285998
2016	495292
2017	495331
2018	511044
min	82588
max	511044

Figure 41: Annual scores of the model (blue) and analysis (red) when compared to the rescaled SWI-001 over the Murray-Darling basin at 0.25° spatial resolution, with N ranging from 82,588 in 2014 to 511,044 in 2018. The yearly N values are indicated in the legend Table. Analysis-Model differences show the impact of assimilating LAI and SWI-001 on the simulated SSM.

Table 6: Annual score values of the model and analysis w.r.t. the rescaled SWI-001 over Western Europe (top) from 2010 to 2018, the Murray-Darling basin (bottom) from 2010 to 2018. Model-analysis differences show the impact of assimilating LAI and SWI-001 on the simulated SSM.

Period	Version	Bias	Correlation	RMSD	SDD	Nb_pts
2010	Model	0.022	0.769	0.047	0.042	164456
2010	Analysis	0.020	0.785	0.045	0.040	164456
2011	Model	0.000	0.821	0.034	0.034	188508
2011	Analysis	-0.000	0.831	0.033	0.033	188508
2012	Model	0.010	0.861	0.034	0.033	195031
2012	Analysis	0.008	0.872	0.032	0.031	195031
2013	Model	0.007	0.812	0.040	0.039	182596
2013	Analysis	0.006	0.826	0.038	0.038	182596
2014	Model	-0.001	0.834	0.032	0.032	205216
2014	Analysis	-0.002	0.845	0.031	0.031	205216
2015	Model	0.006	0.857	0.034	0.033	279547
2015	Analysis	0.005	0.870	0.032	0.032	279547
2016	Model	-0.005	0.855	0.035	0.034	343779
2016	Analysis	-0.005	0.873	0.032	0.032	343779
2017	Model	-0.007	0.820	0.035	0.034	347603
2017	Analysis	-0.007	0.837	0.033	0.032	347603
2018	Model	-0.014	0.862	0.040	0.037	355061
2018	Analysis	-0.013	0.880	0.037	0.035	355061

Period	Version	Bias	Correlation	RMSD	SDD	Nb_pts
2010	Model	-0.010	0.832	0.037	0.036	85972
2010	Analysis	-0.004	0.840	0.035	0.034	85972
2011	Model	-0.014	0.823	0.037	0.034	85439
2011	Analysis	-0.008	0.848	0.032	0.031	85439
2012	Model	-0.007	0.885	0.030	0.029	83612
2012	Analysis	-0.002	0.897	0.028	0.028	83612
2013	Model	0.003	0.895	0.027	0.027	84304
2013	Analysis	0.005	0.904	0.026	0.025	84304
2014	Model	0.007	0.876	0.030	0.030	82588
2014	Analysis	0.009	0.891	0.029	0.028	82588
2015	Model	0.004	0.890	0.028	0.027	285998
2015	Analysis	0.005	0.906	0.026	0.025	285998
2016	Model	0.000	0.896	0.030	0.030	495292
2016	Analysis	0.001	0.911	0.028	0.028	495292
2017	Model	0.000	0.878	0.026	0.026	495331
2017	Analysis	0.003	0.898	0.024	0.024	495331
2018	Model	0.008	0.842	0.030	0.029	511044
2018	Analysis	0.008	0.886	0.026	0.025	511044

Conclusion for SWI-001:

Contrary to LAI and FAPAR products:

- SSM scores in 2018 do not present significantly better values than for the 2010-2017 reference period of time (Figure 38, Figure 39, Figure 40, Figure 41, Table 6),
- the analyzed SSM does not present a reinforcement of the drought signal over Western Europe with respect to the modelled SSM.

For example, in September and in October 2018, the analysis leads to larger SSM values (Figure 27) in areas where the analysis leads to smaller LAI values (Figure 5): eastern England, the Netherlands and Belgium. The same conclusion can be drawn for the Murray-Darling basin for January 2018 only (see the southwestern part of the area in Figure 7 for LAI and in Figure 28 for SSM).

The impact of the seasonal SSM CDF-matching performed prior the assimilation is particularly striking for Western Europe (Figure 36): while the lowest SSM rescaled observations, model and analysis simulations are observed during the summer of 2018, the raw SWI-001 time series indicate lower values during the springs of 2010, 2011, 2012, 2015, 2016, and 2017. Without the complex seasonal CDF-matching, the SSM information would be misleading over Western Europe. On the other hand, raw and rescaled observations are much more proportional over the Murray-Darling basin (Figure 37), and a simple constant CDF-matching would probably give similar results as the seasonal CDF-matching over this region.

8 RESULTS FOR LST

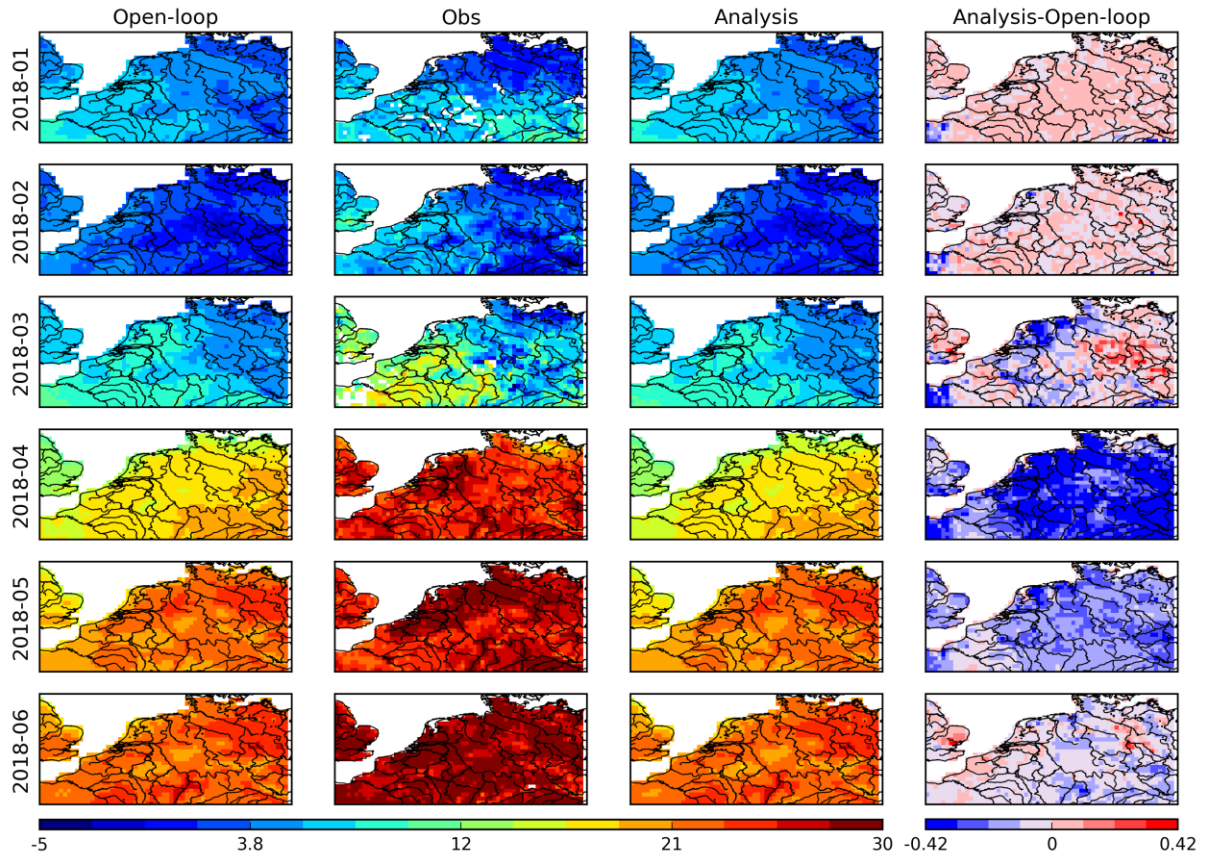


Figure 42: Monthly average values of LST at 1200 UTC over Western Europe at 0.25° spatial resolution from January to June 2018. From left to right: model, satellite product, analysis, analysis-model difference. The latter shows the impact of assimilating LAI and SWI-001 on the simulated LST. The color scale range of LST values is -5 to 30 °C.

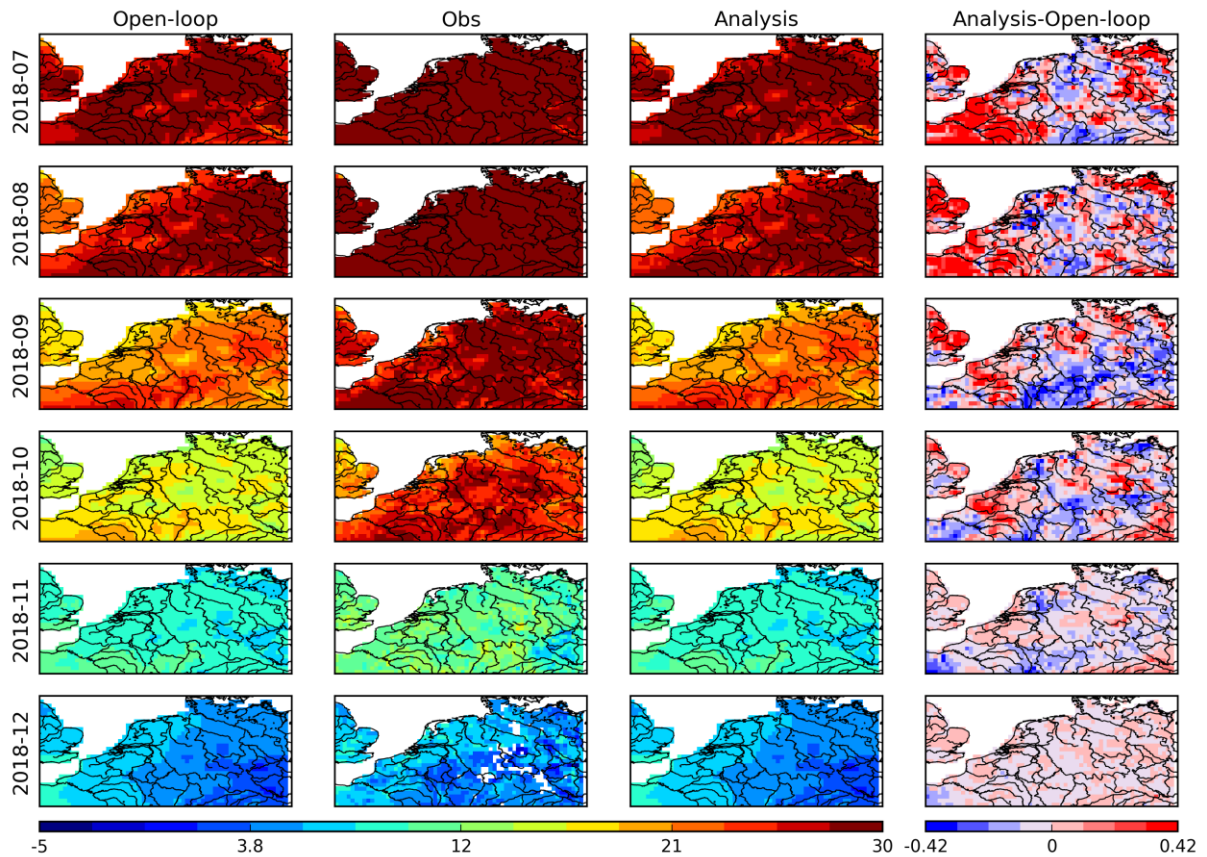


Figure 43: Monthly average values of LST at 1200 UTC over Western Europe at 0.25° spatial resolution from July to December 2018. From left to right: model, satellite product, analysis, analysis-model difference. The latter shows the impact of assimilating LAI and SWI-001 on the simulated LST. The color scale range of LST values is -5 to 30 °C.

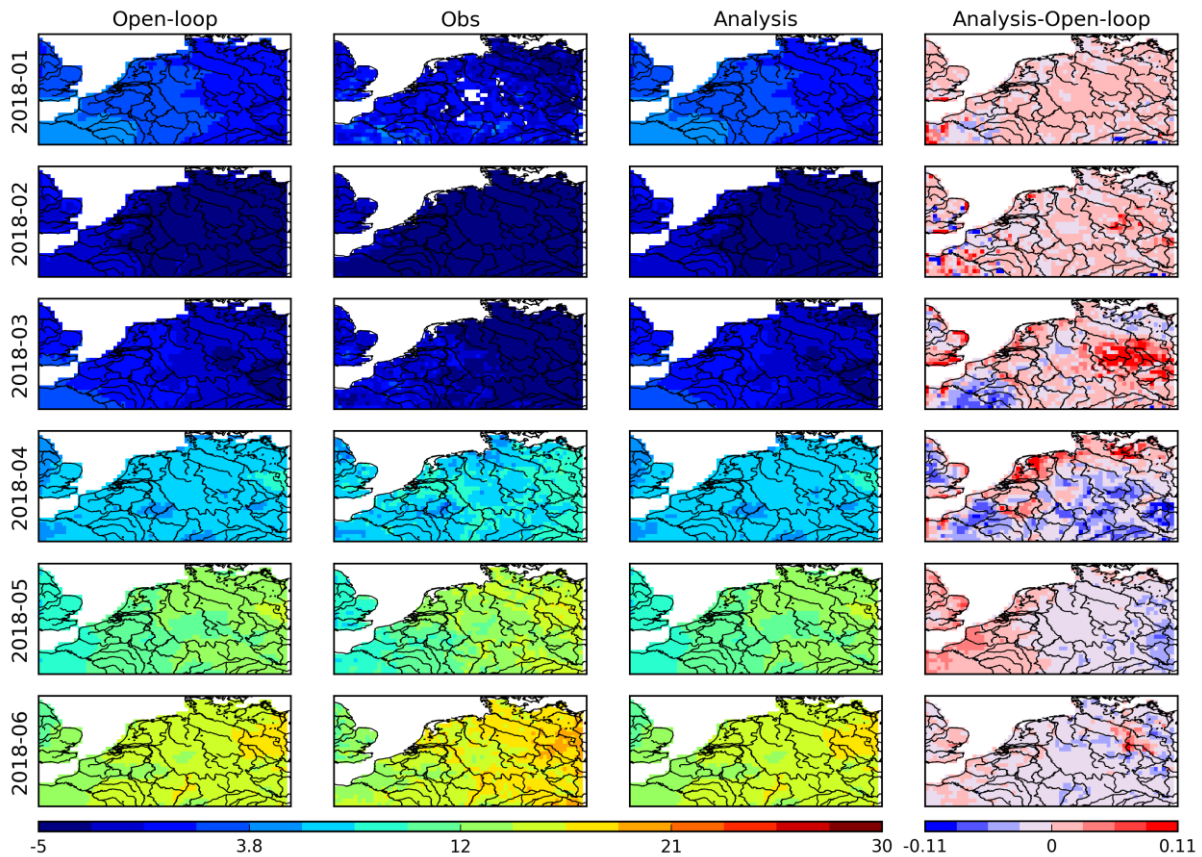


Figure 44: Monthly average values of LST at 0600 UTC over Western Europe at 0.25° spatial resolution from January to June 2018. From left to right: model, satellite product, analysis, analysis-model difference. The latter shows the impact of assimilating LAI and SWI-001 on the simulated LST. The color scale range of LST values is -5 to 30 °C.

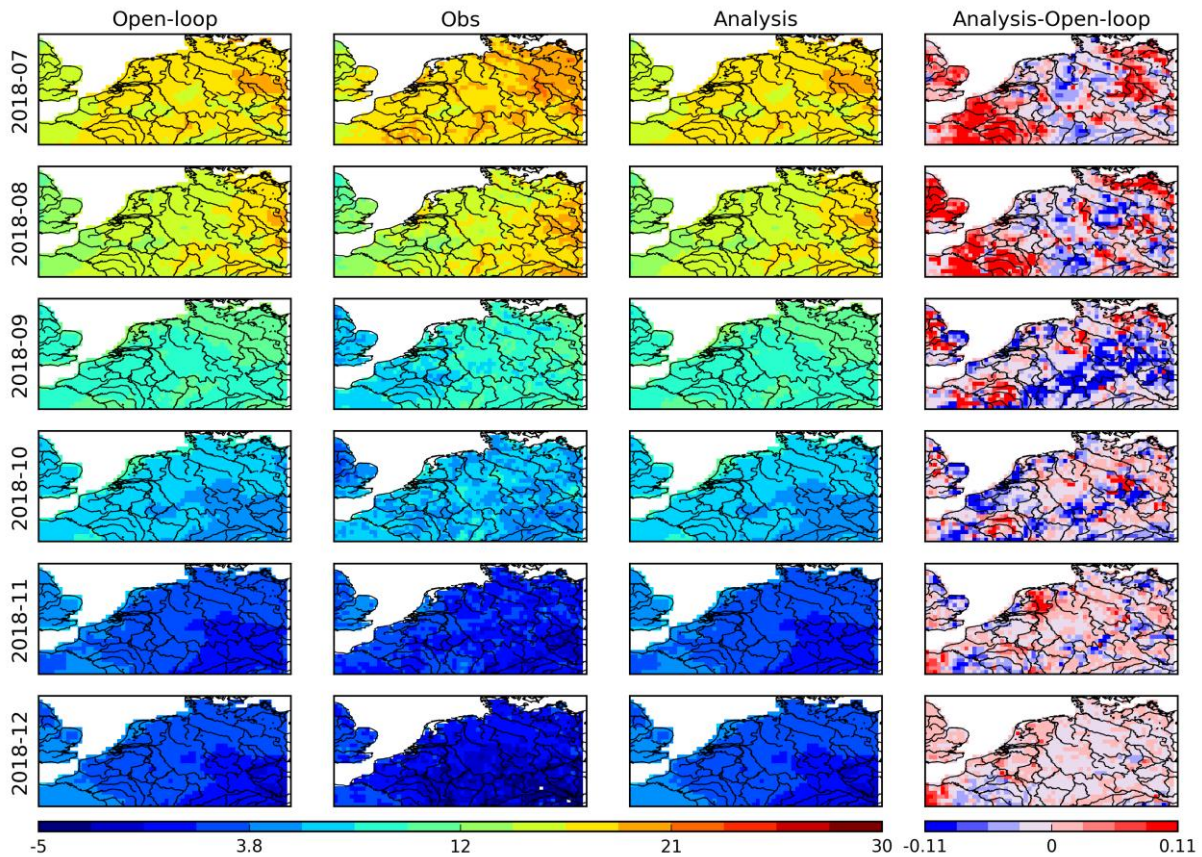


Figure 45: Monthly average values of LST at 0600 UTC over Western Europe at 0.25° spatial resolution from July to December 2018. From left to right: model, satellite product, analysis, analysis-model difference. The latter shows the impact of assimilating LAI and SWI-001 on the simulated LST. The color scale range of LST values is -5 to 30 °C.

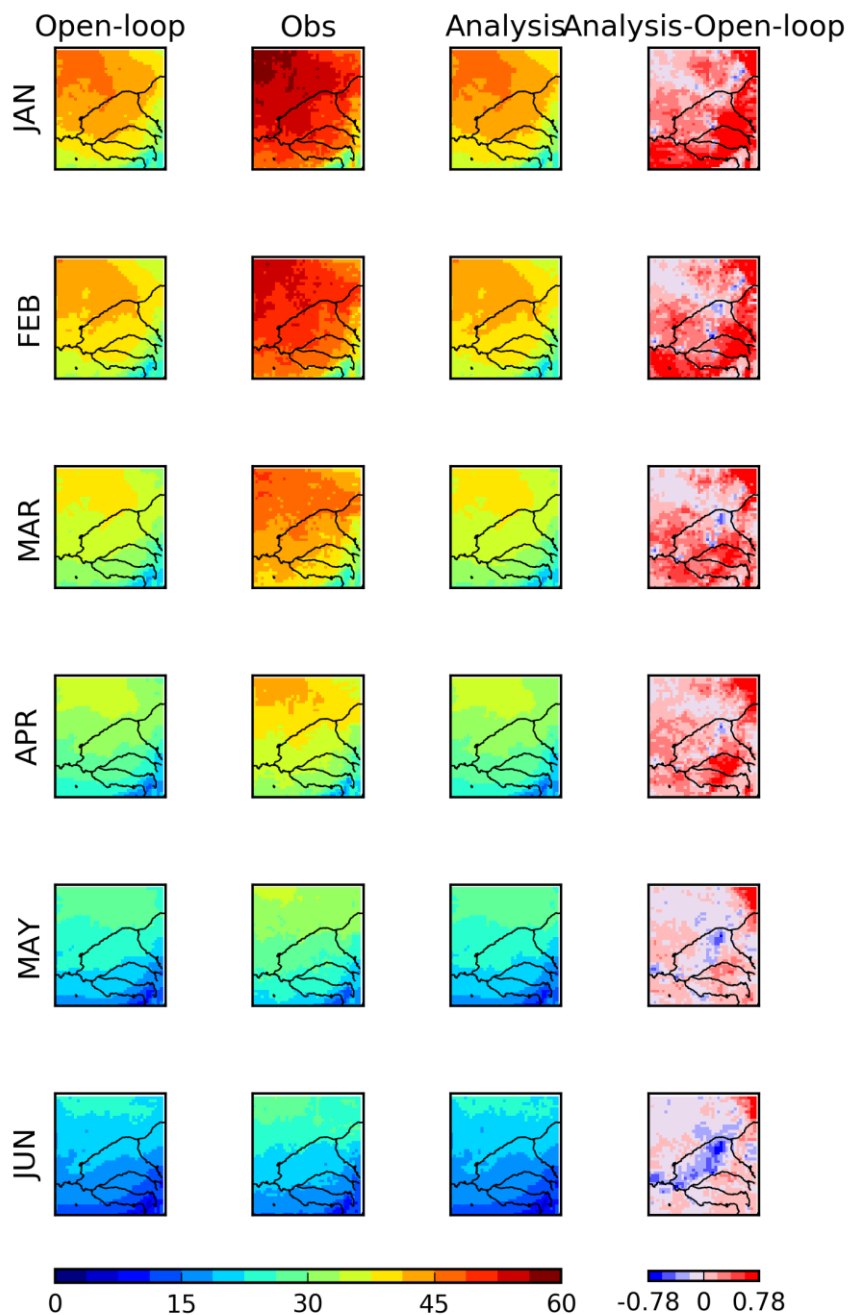


Figure 46: Monthly average values of LST at 0300 UTC (~noon) over the Murray-Darling basin at 0.25° spatial resolution from January to June 2018: model (left), satellite (middle) product, and analysis (right). Analysis-Model differences show the impact of assimilating LAI and SWI-001 on the simulated LST. The color scale range of LST values is 0 to 60 °C.

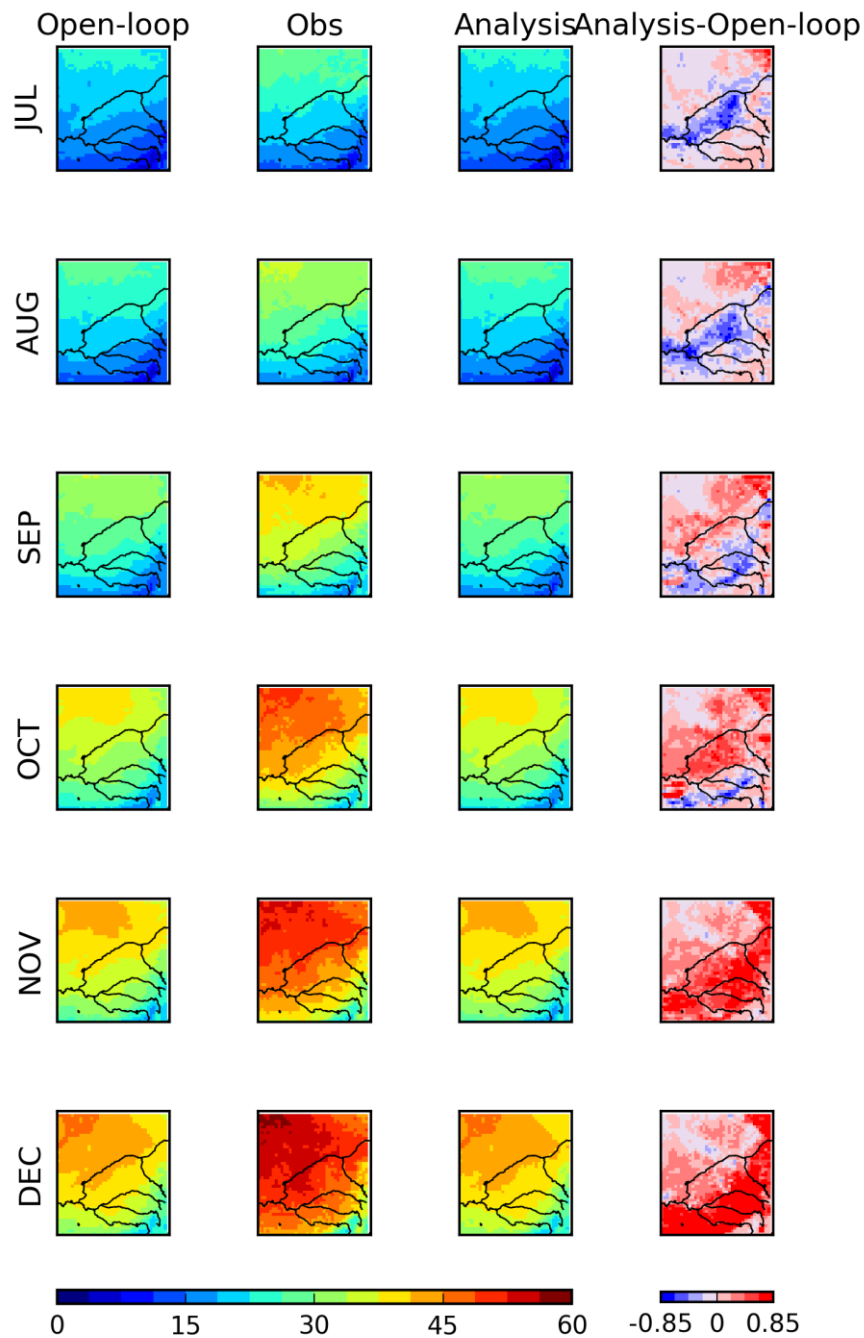


Figure 47: Monthly average values of LST at 0300 UTC (~noon) over the Murray-Darling basin at 0.25° spatial resolution from July to December 2018: model (left), satellite (middle) product, and analysis (right). Analysis-Model differences show the impact of assimilating LAI and SWI-001 on the simulated LST. The color scale range of LST values is 0 to 60 °C.

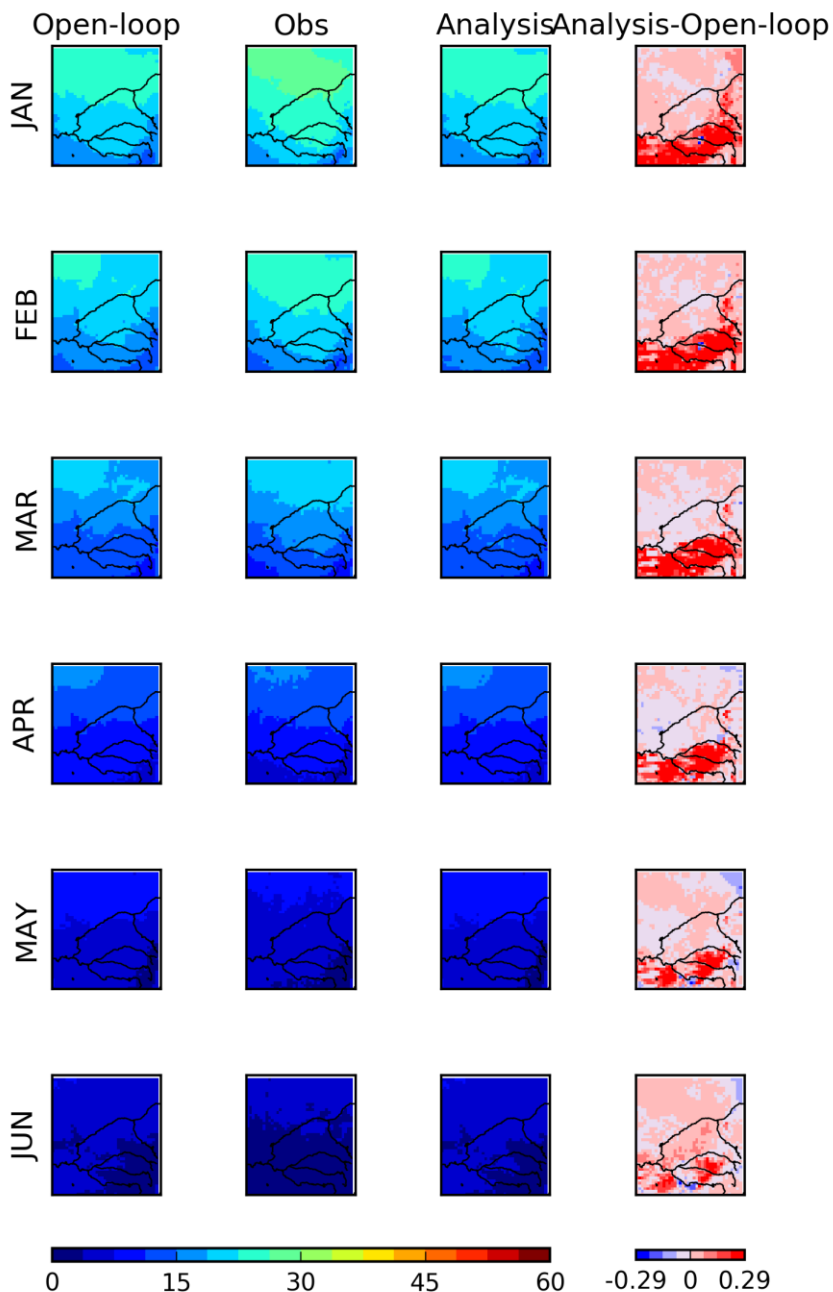


Figure 48: Monthly average values of LST at 2100 UTC (~dawn) over the Murray-Darling basin at 0.25° spatial resolution from January to June 2018: model (left), satellite (middle) product, and analysis (right). Analysis-Model differences show the impact of assimilating LAI and SWI-001 on the simulated LST. The color scale range of LST values is 0 to 60 °C.

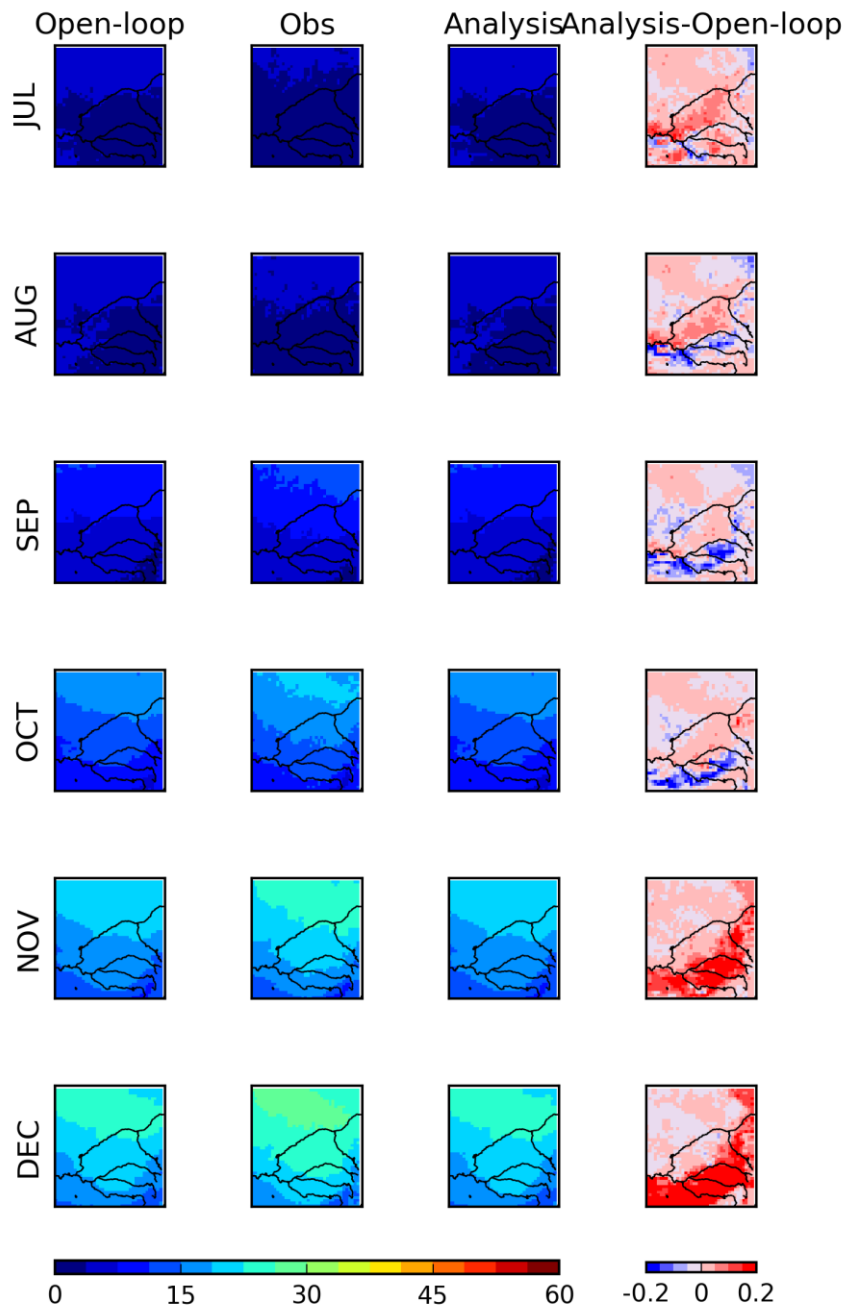


Figure 49: Monthly average values of LST at 2100 UTC (~dawn) over the Murray-Darling basin at 0.25° spatial resolution from July to December 2018: model (left), satellite (middle) product, and analysis (right). Analysis-Model differences show the impact of assimilating LAI and SWI-001 on the simulated LST. The color scale range of LST values is 0 to 60 °C.

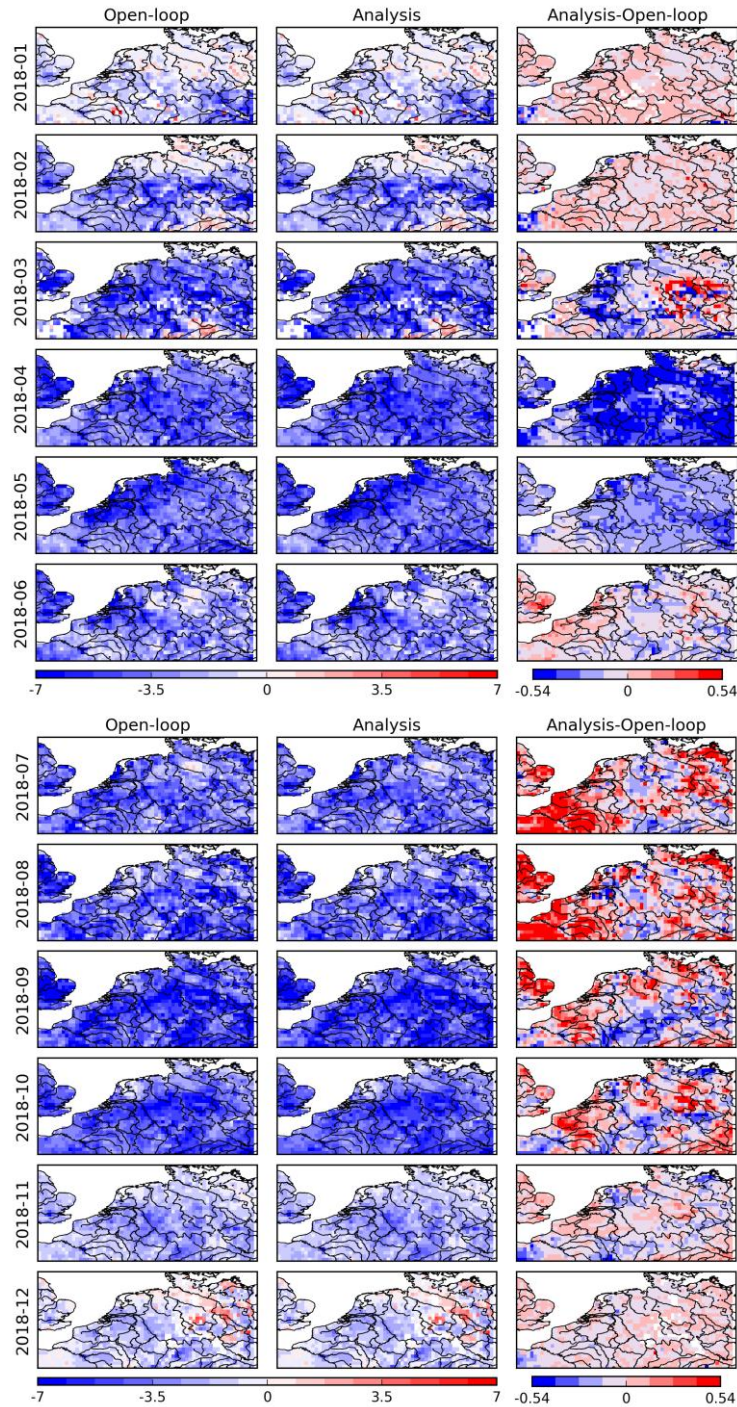


Figure 50: Monthly bias for LST at 1200 UTC over Western Europe at 0.25° spatial resolution from January to December 2018. From left to right: model, analysis, analysis-model difference. The latter shows the impact of assimilating LAI and SWI-001 on the simulated LST. The color scale range of LST bias values is -7 to 7 °C.

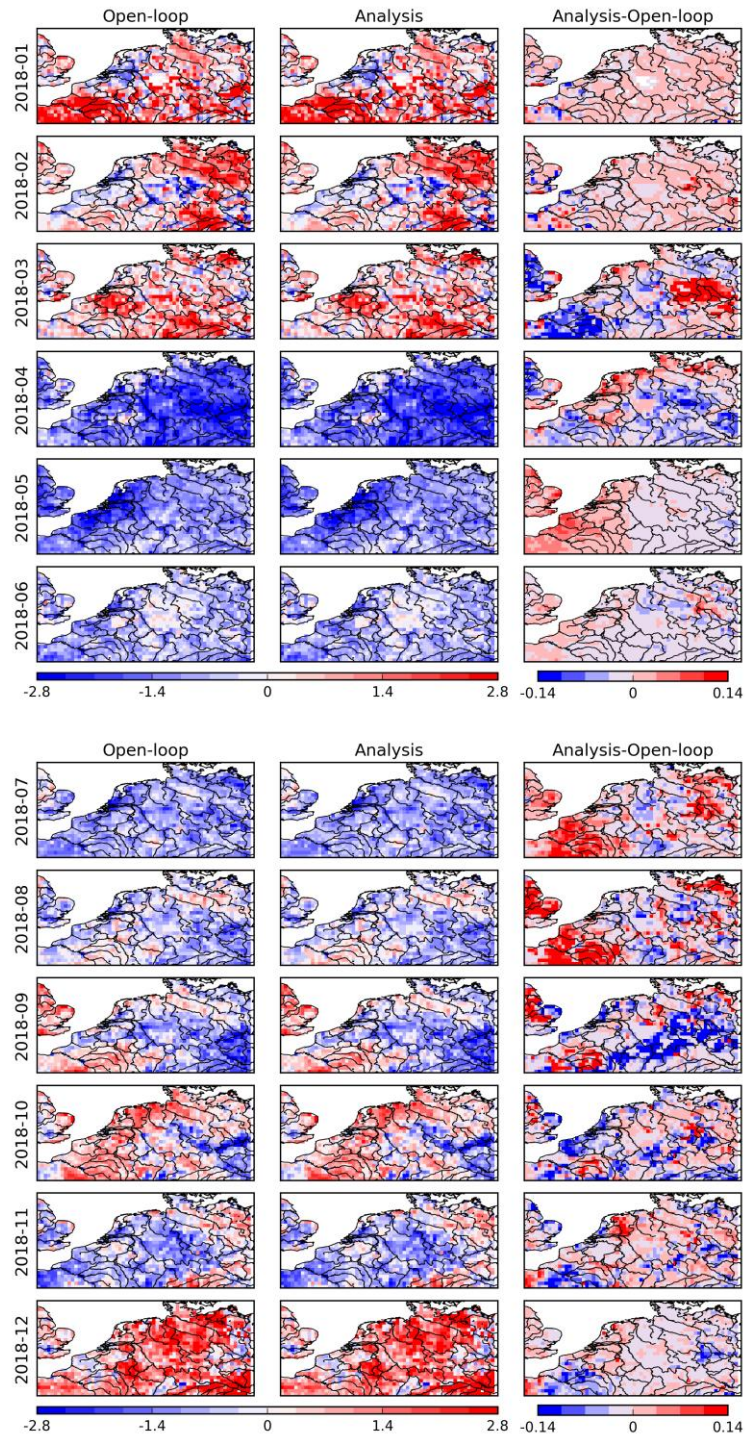


Figure 51: Monthly bias for LST at 0600 UTC over Western Europe at 0.25° spatial resolution from January to December 2018. From left to right: model, analysis, analysis-model difference. The latter shows the impact of assimilating LAI and SWI-001 on the simulated LST. The color scale range of LST bias values is -2.8 to 2.8 °C.

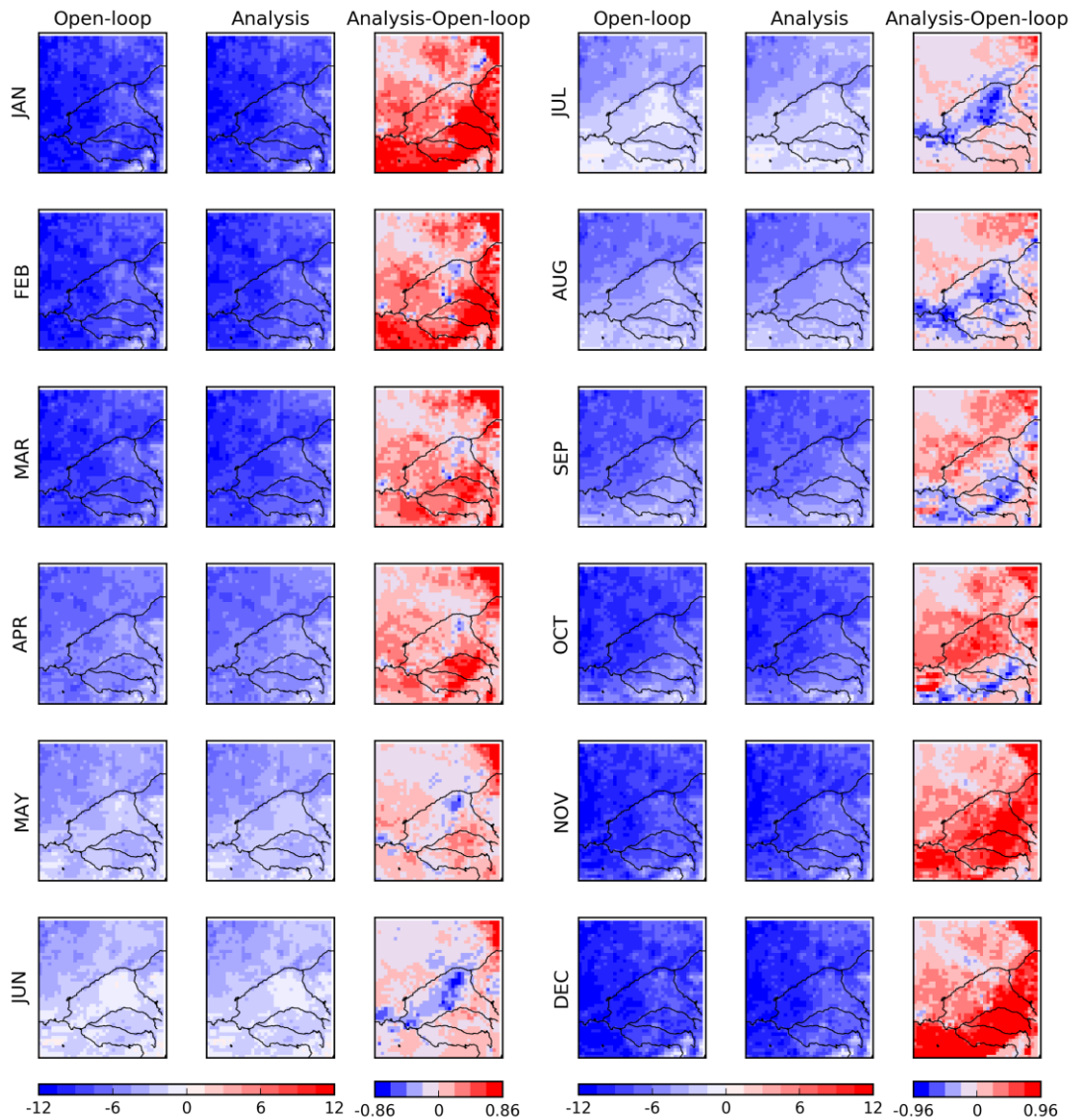


Figure 52: Monthly bias for LST at 0300 UTC (~noon) over the Murray-Darling basin at 0.25° spatial resolution from January to December 2018. From left to right: model, analysis, analysis-model difference. The latter shows the impact of assimilating LAI and SWI-001 on the simulated LST. The color scale range of LST bias values is -12 to 12 °C.

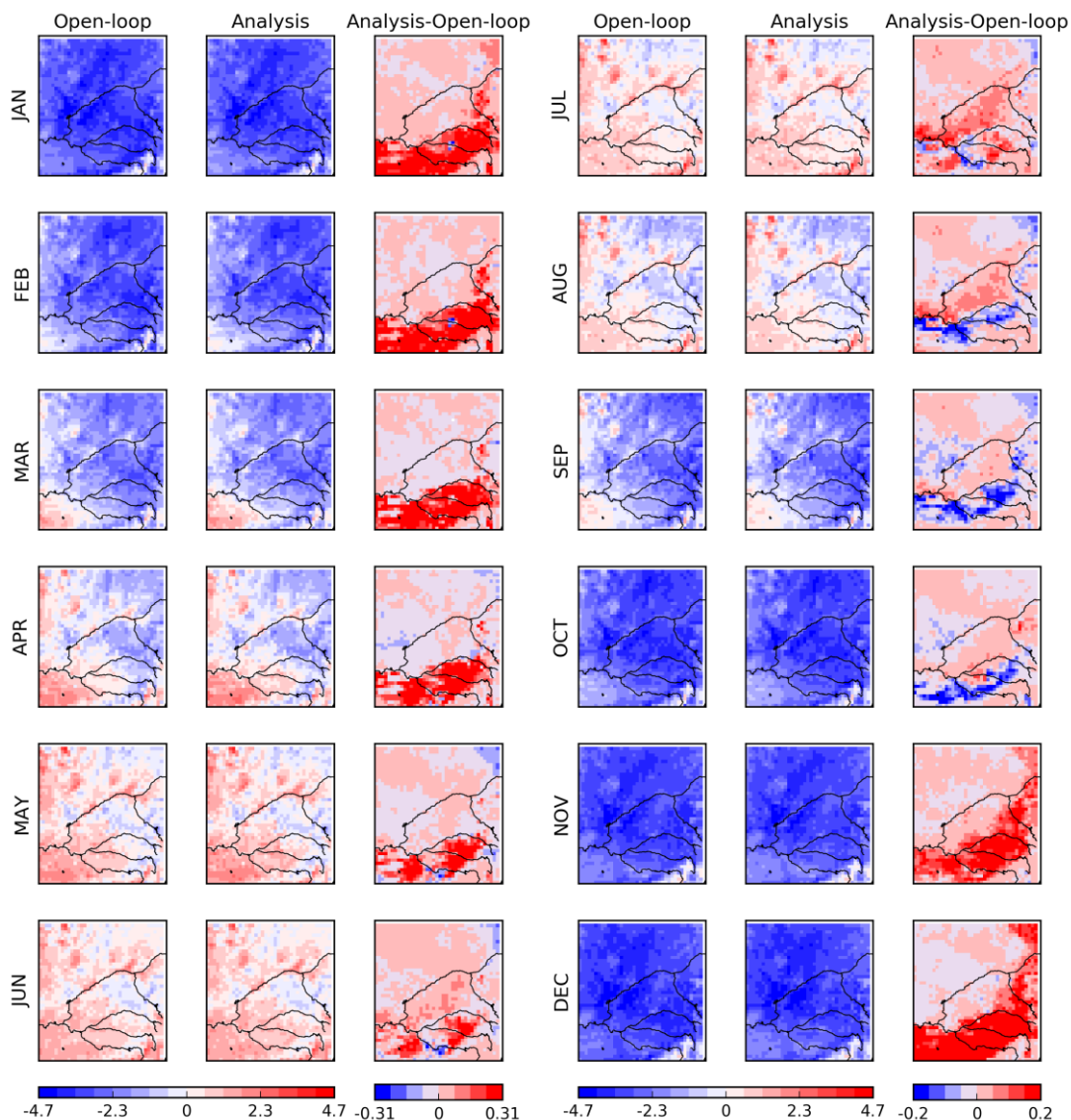


Figure 53: Monthly bias for LST at 2100 UTC (~dawn) over the Murray-Darling basin at 0.25° spatial resolution from January to December 2018. From left to right: model, analysis, analysis-model difference. The latter shows the impact of assimilating LAI and SWI-001 on the simulated LST. The color scale range of LST bias values is -4.7 to 4.7 °C.

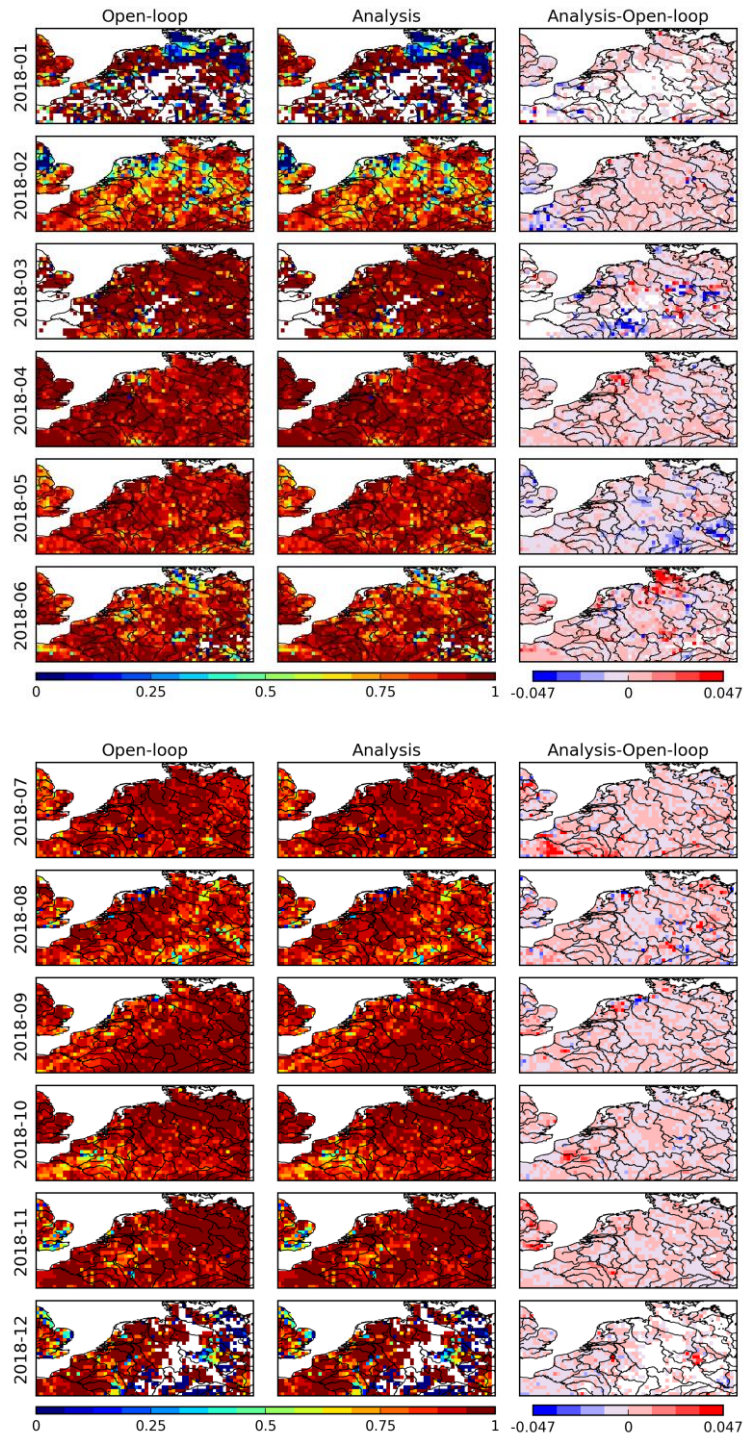


Figure 54: Monthly correlation for LST at 1200 UTC over Western Europe at 0.25° spatial resolution from January to December 2018. From left to right: model, analysis, analysis-model difference. The latter shows the impact of assimilating LAI and SWI-001 on the simulated LST.

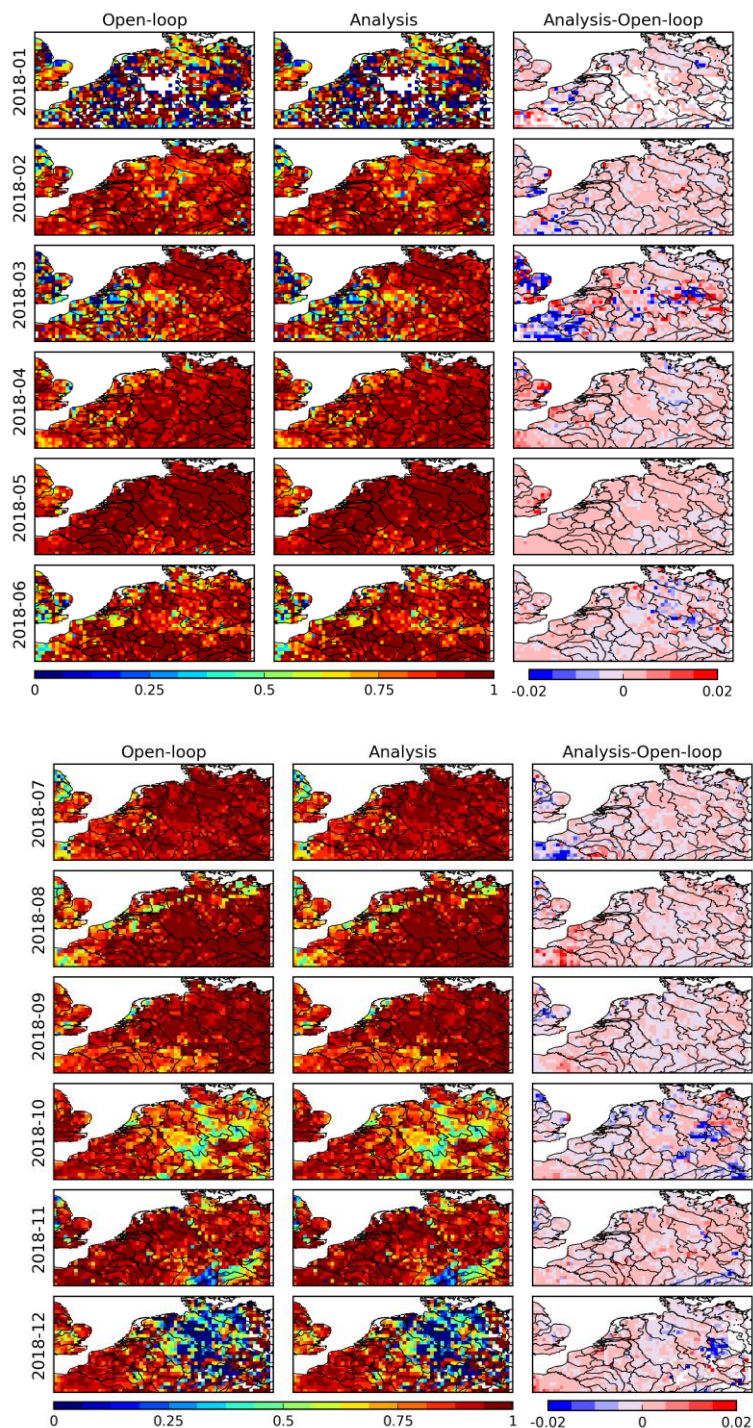


Figure 55: Monthly correlation for LST at 0600 UTC over Western Europe at 0.25° spatial resolution from January to December 2018. From left to right: model, analysis, analysis-model difference. The latter shows the impact of assimilating LAI and SWI-001 on the simulated LST.

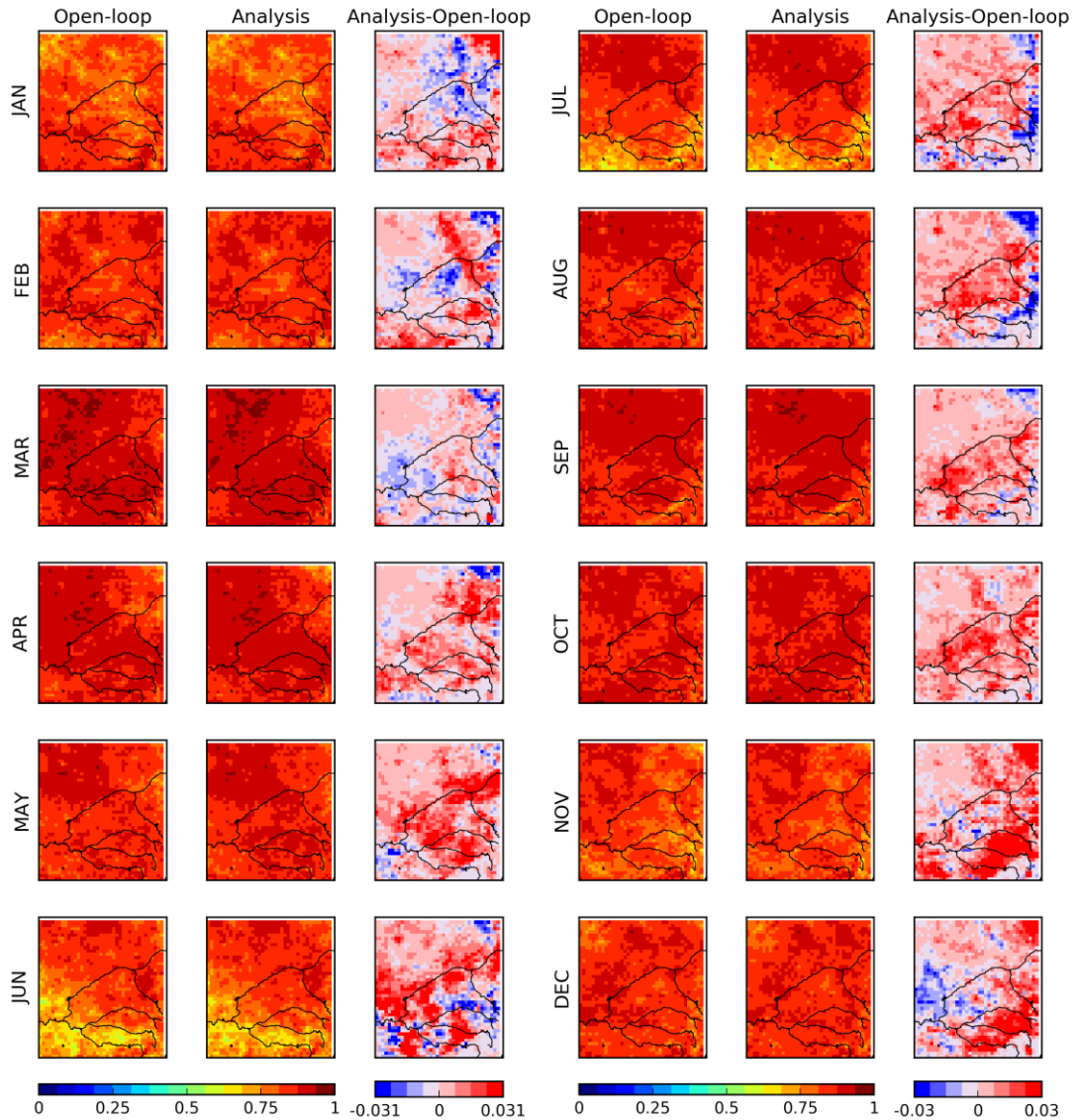


Figure 56: Monthly correlation for LST at 0300 UTC (~noon) over the Murray-Darling basin at 0.25° spatial resolution from January to December 2018. From left to right: model, analysis, analysis-model difference. The latter shows the impact of assimilating LAI and SWI-001 on the simulated LST.

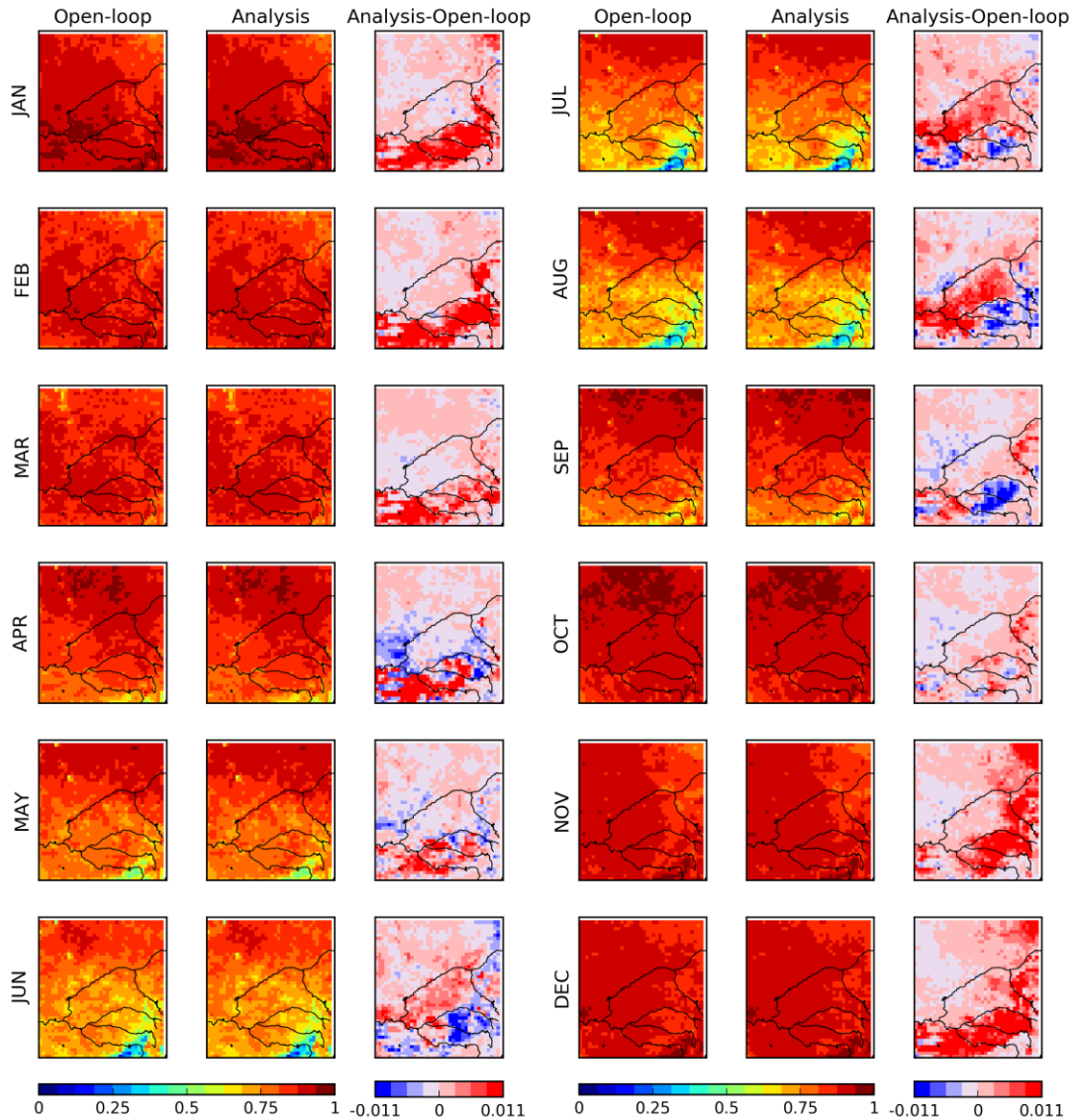
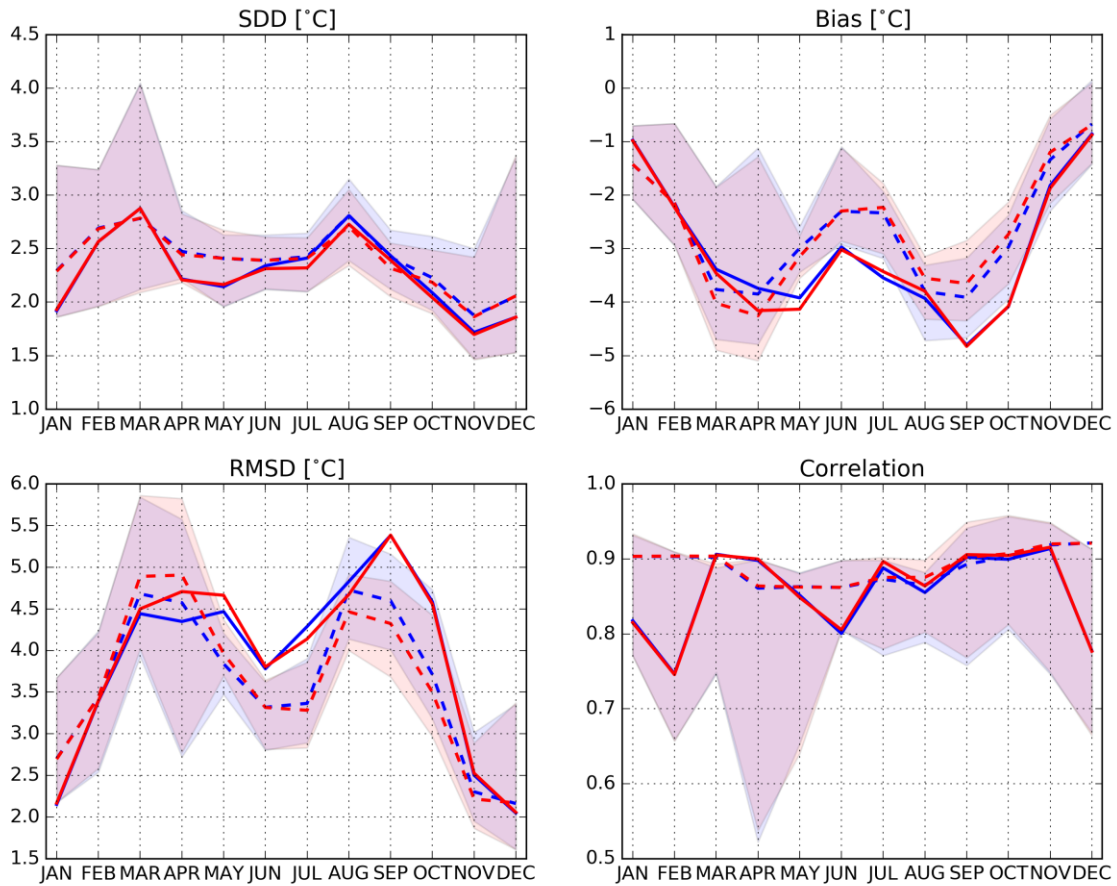
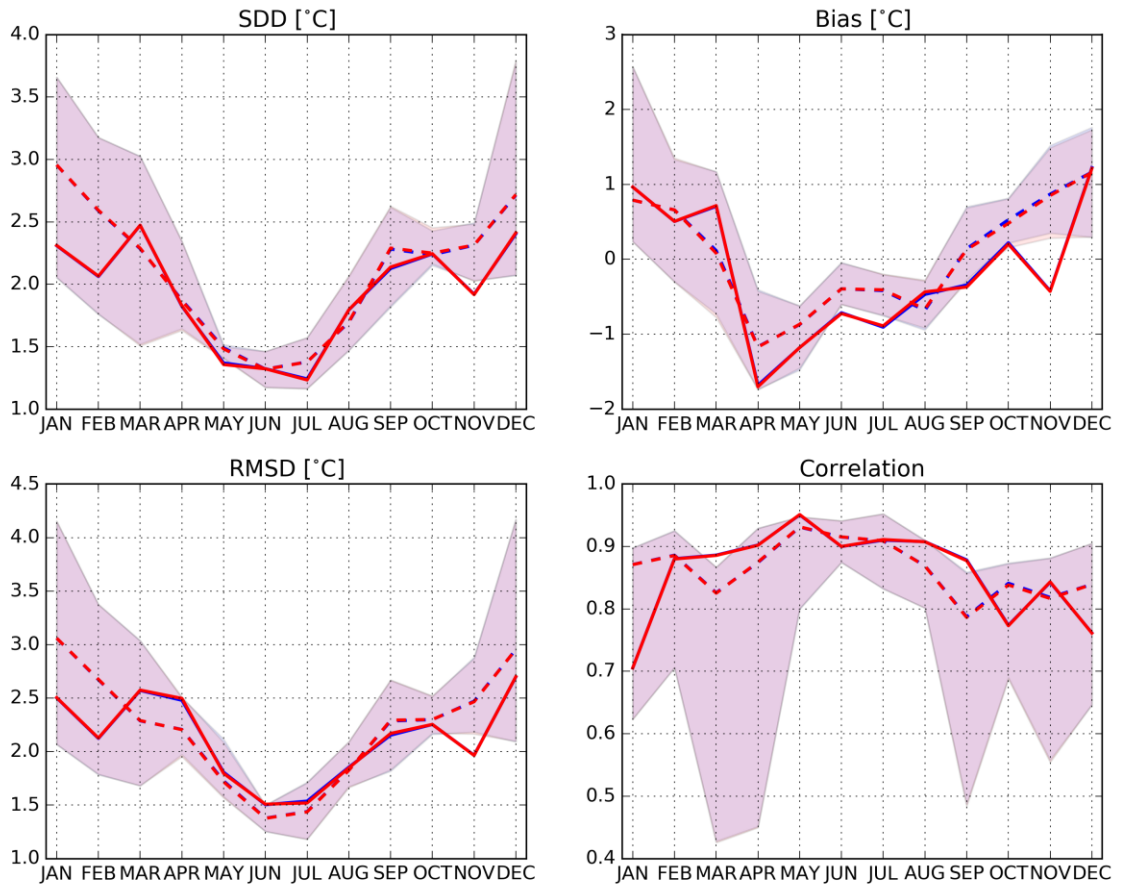


Figure 57: Monthly correlation for LST at 2100 UTC (~dawn) over the Murray-Darling basin at 0.25° spatial resolution from January to December 2018. From left to right: model, analysis, analysis-model difference. The latter shows the impact of assimilating LAI and SWI-001 on the simulated LST.



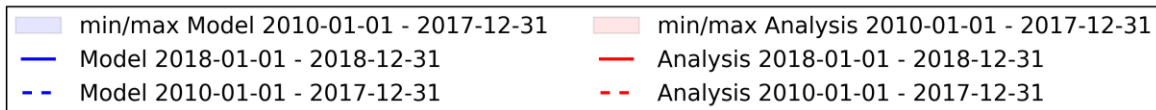
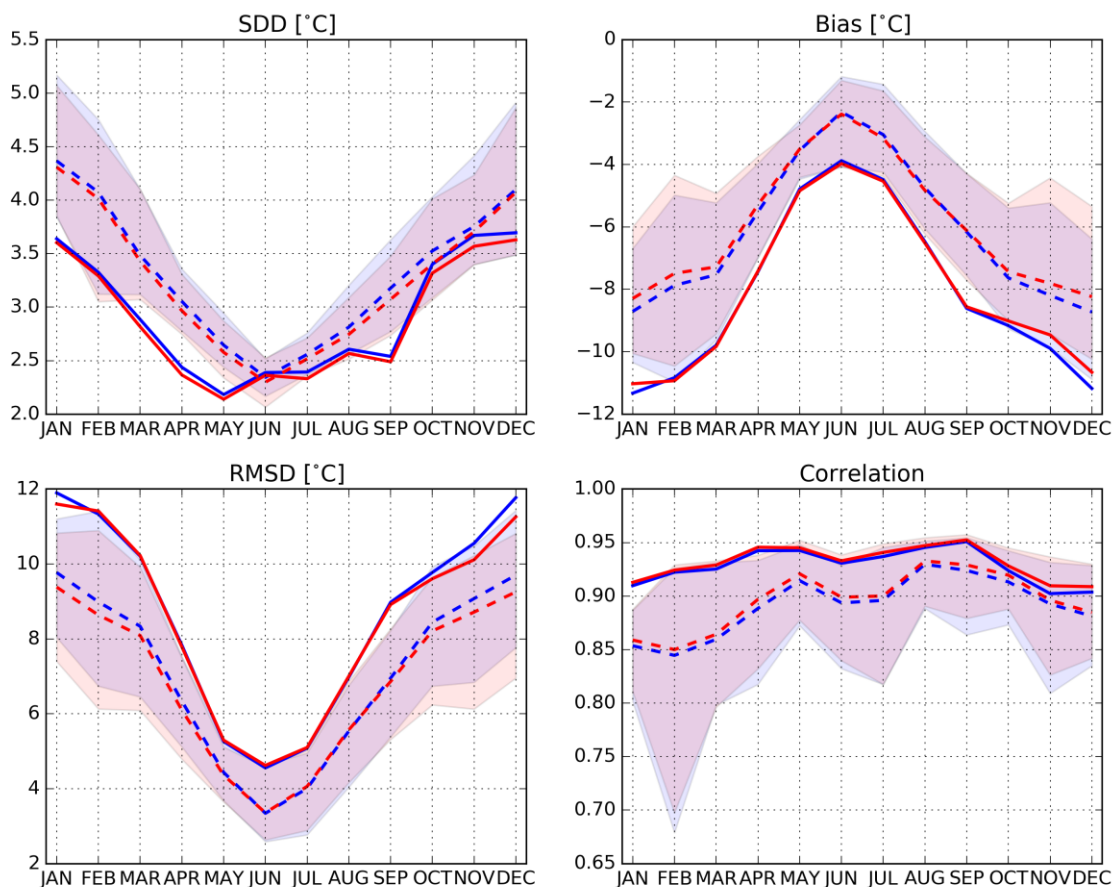
	JAN	FEB	MAR	APR	MAY	JUN	JUL	AUG	SEP	OCT	NOV	DEC	min	max
2010-01-01 - 2017-12-31	47133	47795	89644	61289	55686	64613	68474	71619	66828	66366	46080	46003	46003	89644
2018-01-01 - 2018-12-31	3518	11977	5658	10970	15793	8852	14997	12594	13094	15583	9209	4106	3518	15793

Figure 58: Monthly LST scores at 1200 UTC of the model (blue) and analysis (red) when compared to observations over Western Europe at 0.25° spatial resolution: from 2010 to 2017 (dashed lines), with N ranging from 46,003 in December to 89,644 in March; and 2018 (solid lines), with N ranging from 3,518 in January to 15,793 in May. The monthly N values are indicated in the legend Table. Analysis-Model differences show the impact of assimilating LAI and SWI-001 on the simulated LST. Shaded areas are between minimum and maximum score values recorded from 2010 to 2017.



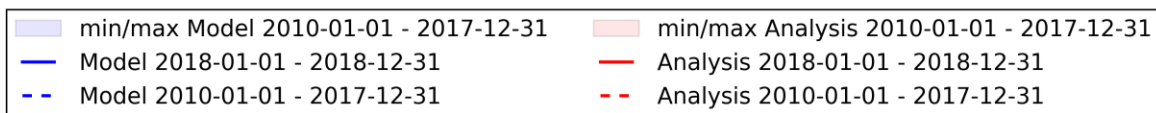
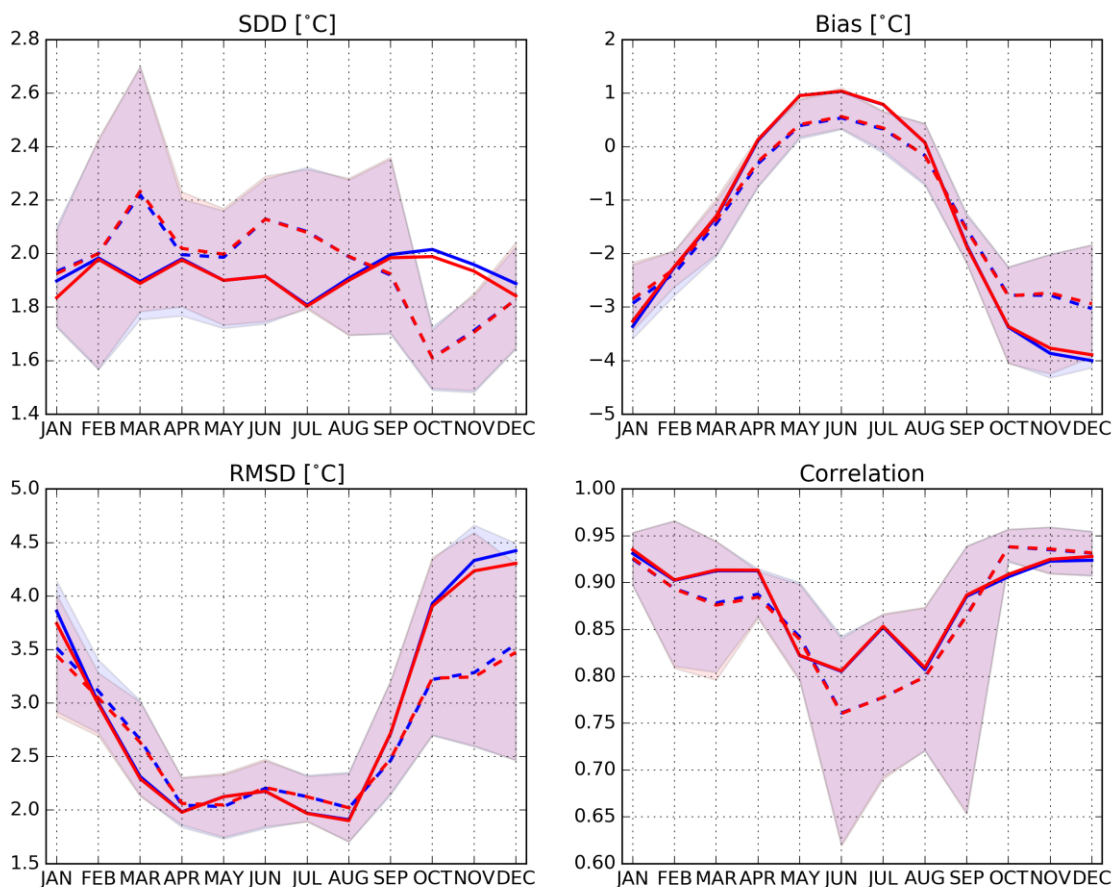
	JAN	FEB	MAR	APR	MAY	JUN	JUL	AUG	SEP	OCT	NOV	DEC	min	max
2010-01-01 - 2017-12-31	66724	68473	121511	103665	93851	102831	111954	117912	120032	104756	65939	65986	65939	121511
2018-01-01 - 2018-12-31	4617	15766	9397	13430	20550	14117	23143	20051	19502	18004	9773	7295	4617	23143

Figure 59: Monthly LST scores at 0600 UTC of the model (blue) and analysis (red) when compared to observations over Western Europe at 0.25° spatial resolution: from 2010 to 2017 (dashed lines), with N ranging from 65,939 in November to 121,511 in March; and 2018 (solid lines), with N ranging from 4,617 in January to 23,143 in July. The monthly N values are indicated in the legend Table. Analysis-Model differences show the impact of assimilating LAI and SWI-001 on the simulated LST. Shaded areas are between minimum and maximum score values recorded from 2010 to 2017.



	JAN	FEB	MAR	APR	MAY	JUN	JUL	AUG	SEP	OCT	NOV	DEC	min	max
2010-01-01 - 2017-12-31	260972	236918	203215	240197	252091	215145	250319	270278	271237	276530	219177	254967	203215	276530
2018-01-01 - 2018-12-31	32440	31293	41246	43105	38879	35667	43685	41487	41130	29839	31367	35622	29839	43685

Figure 60: Monthly LST scores at 0300 UTC (~noon) of the model (blue) and analysis (red) when compared to observations over the Murray-Darling basin at 0.25° spatial resolution: from 2010 to 2017 (dashed lines), with N ranging from 238,774 in February to 328,607 in August; and 2018 (solid lines), with N ranging from 31,525 in January to 46,979 in July. The monthly N values are indicated in the legend Table. Analysis-Model differences show the impact of assimilating LAI and SWI-001 on the simulated LST. Shaded areas are between minimum and maximum score values recorded from 2010 to 2017.



	JAN	FEB	MAR	APR	MAY	JUN	JUL	AUG	SEP	OCT	NOV	DEC	min	max
2010-01-01 - 2017-12-31	267623	253338	301378	304096	302503	291836	318794	323233	308391	301854	259325	285671	253338	323233
2018-01-01 - 2018-12-31	38109	33596	40583	45982	44590	38724	45289	44758	45176	32842	34586	41687	32842	45982

Figure 61: Monthly LST scores at 2100 UTC (~dawn) of the model (blue) and analysis (red) when compared to observations over the Murray-Darling basin at 0.25° spatial resolution: from 2010 to 2017 (dashed lines), with N ranging from 208,626 in November to 274,567 in August; and 2018 (solid lines), with N ranging from 30,402 in October to 43,894 in July. The monthly N values are indicated in the legend Table. Analysis-Model differences show the impact of assimilating LAI and SWI-001 on the simulated LST. Shaded areas are between minimum and maximum score values recorded from 2010 to 2017.

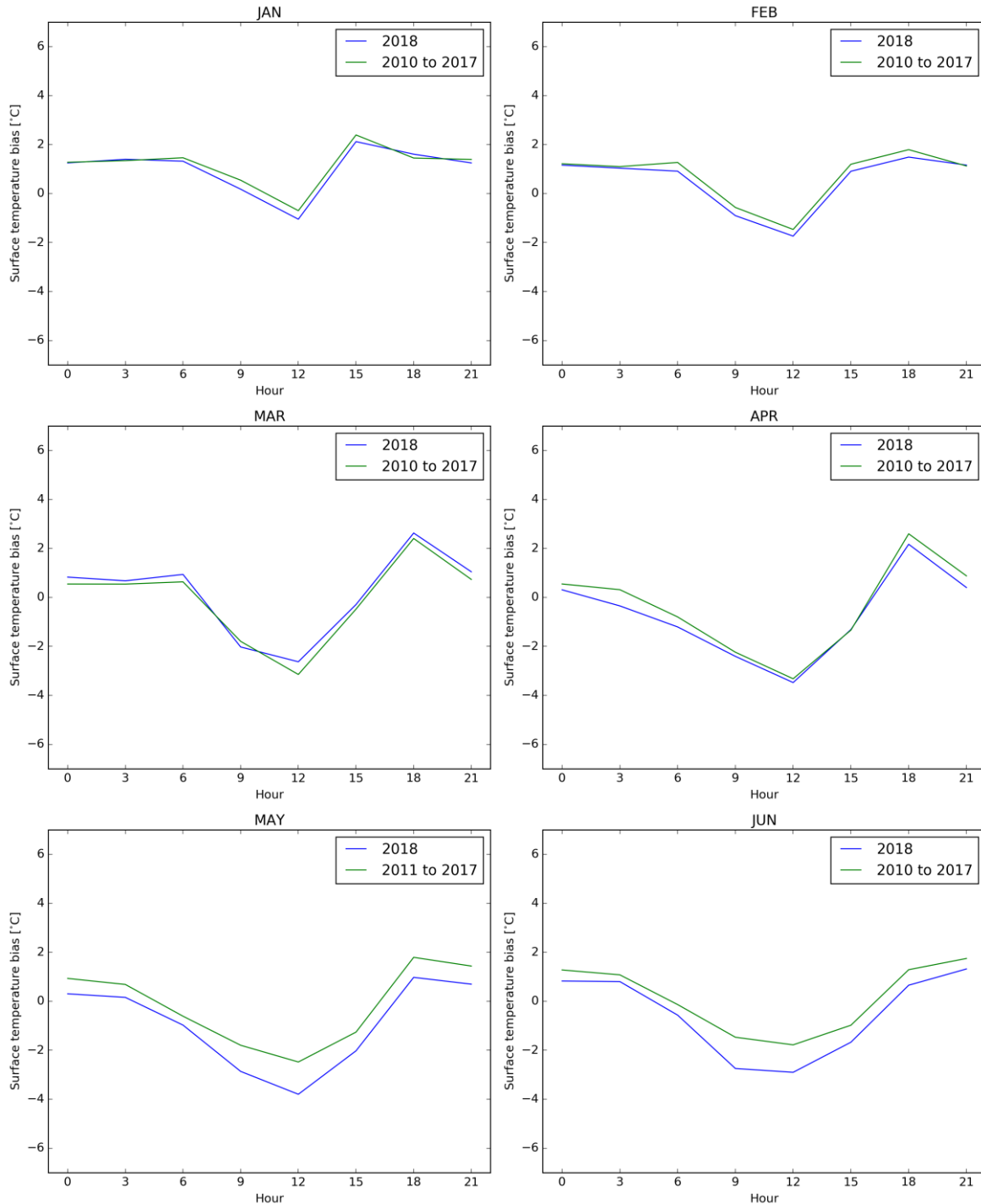


Figure 62: LST 3-hourly bias of the analysis over Western Europe at 0.25° spatial resolution from January to June from 2010 to 2017 (green line) and for 2018 (blue line).

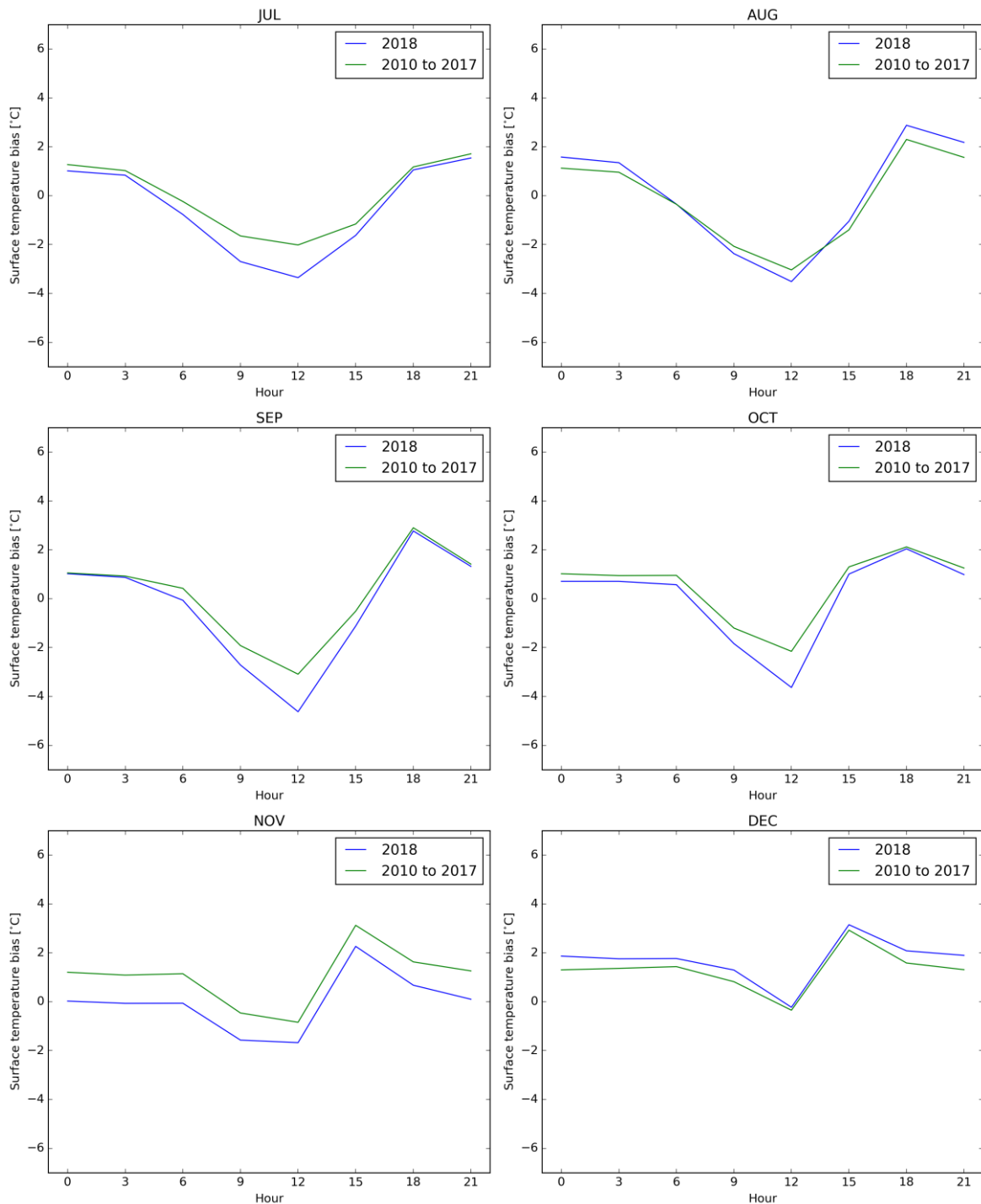


Figure 63: LST 3-hourly bias of the analysis over Western Europe at 0.25° spatial resolution from July to December from 2010 to 2017 (green line) and for 2018 (blue line).

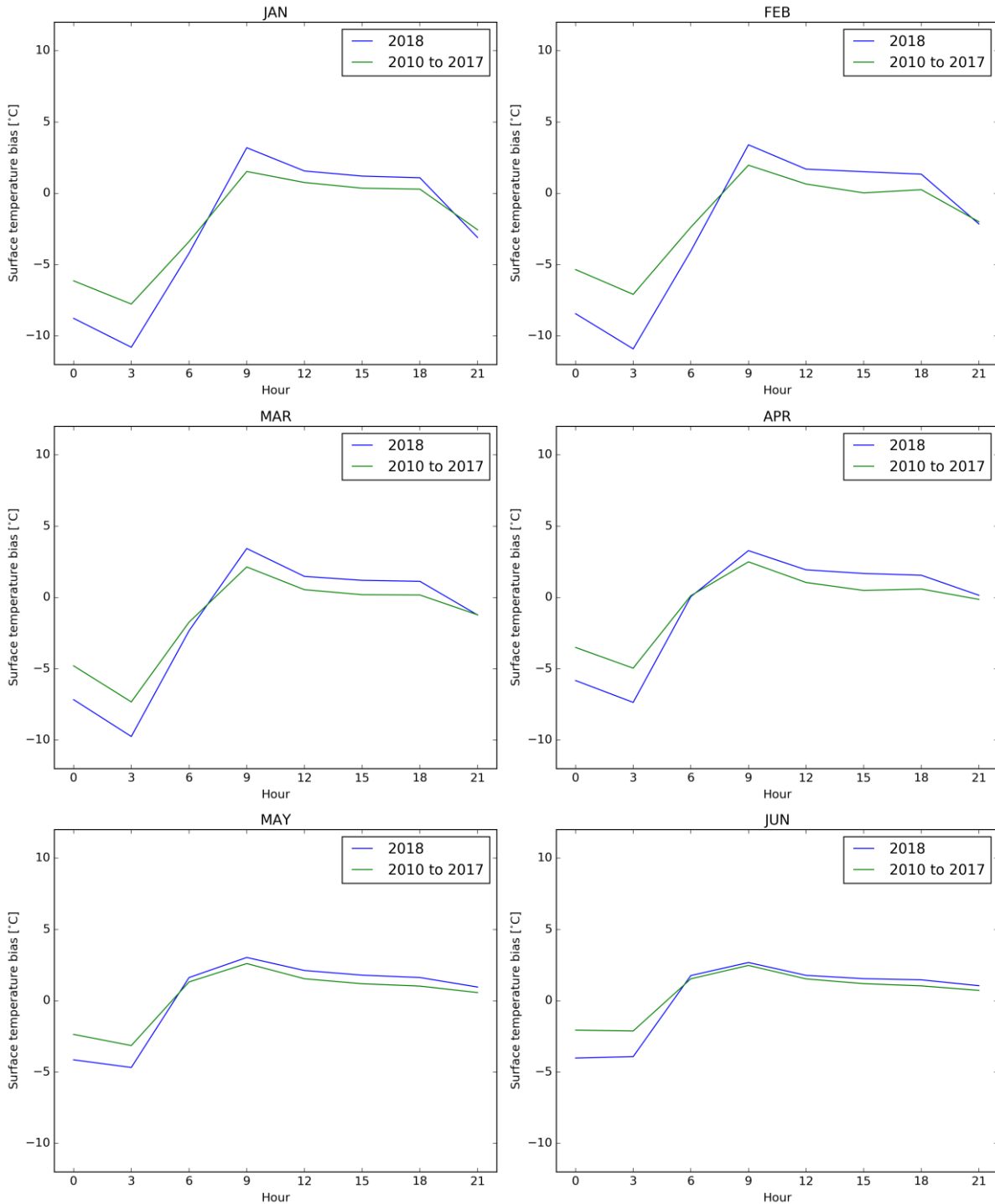


Figure 64: LST 3-hourly bias of the analysis over the Murray-Darling basin at 0.25° spatial resolution from January to June from 2010 to 2017 (green line) and for 2018 (blue line). [Note that 0300 UTC is close to noon at these longitudes.]

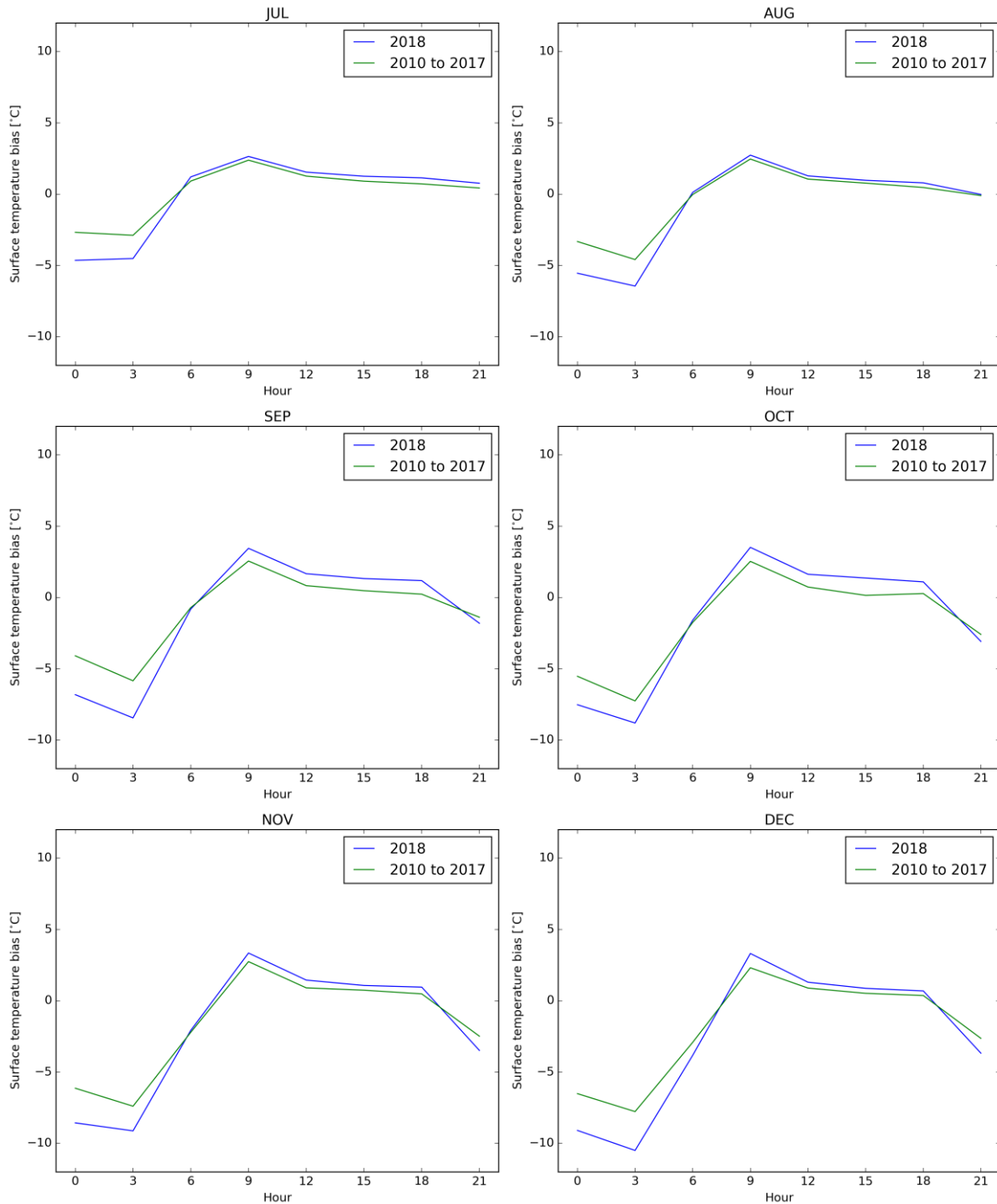


Figure 65: LST 3-hourly bias of the analysis over the Murray-Darling basin at 0.25° spatial resolution from July to December from 2010 to 2017 (green line) and for 2018 (blue line). [Note that 0300 UTC is close to noon at these longitudes.]

Table 7: LST annual scores of the model and analysis w.r.t. the LST observations at 1200 UTC (top) and 0600 UTC (bottom) over Western Europe. Analysis-Model differences show the impact of assimilating LAI and SWI-001 on the simulated LST. The relatively unbiased average LST at 0600 UTC hides marked spatial and seasonal patterns (Figure 51 and Figure 59).

Period	Version	Bias	Correlation	RMSD	SDD	Nb_pts
2010	Model	-2.505	0.971	4.006	3.125	69554
2010	Analysis	-2.404	0.971	3.918	3.095	69554
2011	Model	-3.052	0.959	4.009	2.599	125738
2011	Analysis	-3.070	0.958	4.037	2.622	125738
2012	Model	-2.756	0.972	3.941	2.816	93815
2012	Analysis	-2.762	0.971	3.956	2.832	93815
2013	Model	-2.656	0.971	3.833	2.763	85076
2013	Analysis	-2.615	0.971	3.791	2.744	85076
2014	Model	-2.726	0.961	3.642	2.416	83447
2014	Analysis	-2.764	0.960	3.684	2.435	83447
2015	Model	-2.889	0.969	3.854	2.552	97265
2015	Analysis	-2.873	0.969	3.829	2.531	97265
2016	Model	-2.835	0.980	3.777	2.496	92171
2016	Analysis	-2.800	0.981	3.692	2.407	92171
2017	Model	-2.712	0.976	3.677	2.484	84464
2017	Analysis	-2.738	0.975	3.708	2.501	84464
2018	Model	-3.386	0.977	4.236	2.544	126351
2018	Analysis	-3.436	0.977	4.263	2.524	126351

Period	Version	Bias	Correlation	RMSD	SDD	Nb_pts
2010	Model	0.137	0.970	2.494	2.491	117593
2010	Analysis	0.130	0.970	2.493	2.490	117593
2011	Model	-0.010	0.953	2.197	2.197	169808
2011	Analysis	-0.023	0.953	2.199	2.198	169808
2012	Model	0.210	0.964	2.368	2.359	143772
2012	Analysis	0.202	0.964	2.368	2.359	143772
2013	Model	0.035	0.968	2.262	2.262	136050
2013	Analysis	0.033	0.968	2.264	2.264	136050
2014	Model	-0.282	0.959	1.965	1.945	139525
2014	Analysis	-0.299	0.959	1.966	1.944	139525
2015	Model	-0.288	0.963	2.025	2.005	150066
2015	Analysis	-0.291	0.963	2.024	2.003	150066
2016	Model	-0.064	0.966	2.150	2.149	146200
2016	Analysis	-0.062	0.966	2.150	2.149	146200
2017	Model	-0.065	0.968	2.117	2.116	140620
2017	Analysis	-0.079	0.968	2.116	2.115	140620
2018	Model	-0.376	0.975	2.053	2.018	175645
2018	Analysis	-0.377	0.975	2.054	2.019	175645

Table 8: LST annual scores of the model and analysis w.r.t. the LST observations at 0300 UTC (~noon) (top) and at 2100 UTC (~dawn) (bottom) over the Murray-Darling basin. Analysis-Model differences show the impact of assimilating LAI and SWI-001 on the simulated LST. The relatively unbiased average LST at 0600 UTC hides marked spatial and seasonal patterns (Figure 53 and Figure 61).

Period	Version	Bias	Correlation	RMSD	SDD	Nb_pts
2010	Model	-4.688	0.945	6.338	4.265	325542
2010	Analysis	-4.249	0.951	5.806	3.956	325542
2011	Model	-4.670	0.939	6.033	3.820	319690
2011	Analysis	-4.542	0.944	5.813	3.628	319690
2012	Model	-5.238	0.958	6.393	3.666	387556
2012	Analysis	-5.118	0.960	6.273	3.628	387556
2013	Model	-6.252	0.965	7.421	3.997	367295
2013	Analysis	-6.178	0.966	7.330	3.946	367295
2014	Model	-7.111	0.963	8.268	4.219	389410
2014	Analysis	-6.971	0.964	8.118	4.160	389410
2015	Model	-7.249	0.965	8.550	4.533	373684
2015	Analysis	-7.003	0.967	8.255	4.371	373684
2016	Model	-7.327	0.970	8.497	4.303	357970
2016	Analysis	-7.082	0.973	8.171	4.075	357970
2017	Model	-7.477	0.969	8.472	3.983	429899
2017	Analysis	-7.387	0.971	8.319	3.828	429899
2018	Model	-7.978	0.972	8.875	3.889	445760
2018	Analysis	-7.900	0.974	8.752	3.767	445760

Period	Version	Bias	Correlation	RMSD	SDD	Nb_pts
2010	Model	-1.197	0.958	2.737	2.462	414350
2010	Analysis	-1.136	0.958	2.710	2.461	414350
2011	Model	-1.016	0.964	2.644	2.441	418557
2011	Analysis	-0.982	0.964	2.621	2.430	418557
2012	Model	-1.048	0.970	2.448	2.212	456084
2012	Analysis	-1.039	0.970	2.452	2.221	456084
2013	Model	-1.234	0.970	2.546	2.227	460390
2013	Analysis	-1.210	0.970	2.539	2.232	460390
2014	Model	-1.368	0.971	2.796	2.438	451034
2014	Analysis	-1.351	0.971	2.785	2.436	451034
2015	Model	-1.240	0.970	2.790	2.499	457507
2015	Analysis	-1.194	0.971	2.752	2.479	457507
2016	Model	-1.746	0.953	3.188	2.667	384690
2016	Analysis	-1.700	0.953	3.153	2.655	384690
2017	Model	-1.434	0.975	2.827	2.436	475430
2017	Analysis	-1.390	0.976	2.783	2.411	475430
2018	Model	-1.287	0.972	2.974	2.681	485922
2018	Analysis	-1.259	0.973	2.932	2.649	485922

Conclusion for LST:

The simulated LST is generally smaller than the observed LST at daytime, for both Western Europe and the Murray-Darling basin. At nighttime, the simulated LST tends to be slightly overestimated (Figure 62, Figure 63, Figure 64, Figure 65).

The cold bias observed at noon is particularly large:

- at springtime and during the autumn over Western Europe (down to -5°C) as shown in Figure 58,

- at summertime over the Murray-Darling basin (down to -11°C in 2018) as shown in Figure 60.

These biases at noon are even more striking in 2018 (Table 7, Table 8). Over the Murray-Darling basin, the mean yearly bias is about -8°C in 2018, against -4°C in 2010. Since 2010 is a very wet year compared to 2018 (see RZSM values in Figure 9), this result shows that LST biases are more pronounced in dry conditions.

When the assimilation significantly reduces the simulated LAI (see Chapter 4), the LST noon bias is slightly reduced in the analysis, as shown by Figure 43 and Figure 50 for Western Europe during the heatwave, and by Figure 46, Figure 47 and Figure 52 for the Murray-Darling basin in January and December. Reducing LAI tends to reduce plant transpiration cooling and to increase the simulated LST. Since the model is too cold at noon, the LST bias is reduced. Also, the assimilation tends to improve the temporal correlation of the simulated and observed LST as shown in Figure 54 and Figure 56. This shows the consistency of the observed LST with the observed LAI.

At dawn, the LST bias is rather small over Western Europe (Figure 59) and is more marked in 2018 (Table 7). Over the Murray-Darling basin, a cold LST bias is observed at dawn, down to -4°C at summertime, and the correlation is markedly weaker at wintertime, from May to August (Figure 61).

Possible causes of the spatial, diurnal and seasonal patterns of the LST bias are:

- hot-spot phenomenon (more sunlit than shaded elements are seen by the satellite) as described in Ermida et al. 2018,

- remaining biases in incoming solar (Urraca et al., 2018) and infrared radiation and in air temperature of ERA5.

9 LDAS STATISTICS

9.1 INCREMENTS AND IMPACTS OF THE ASSIMILATION ON WATER AND CARBON FLUXES

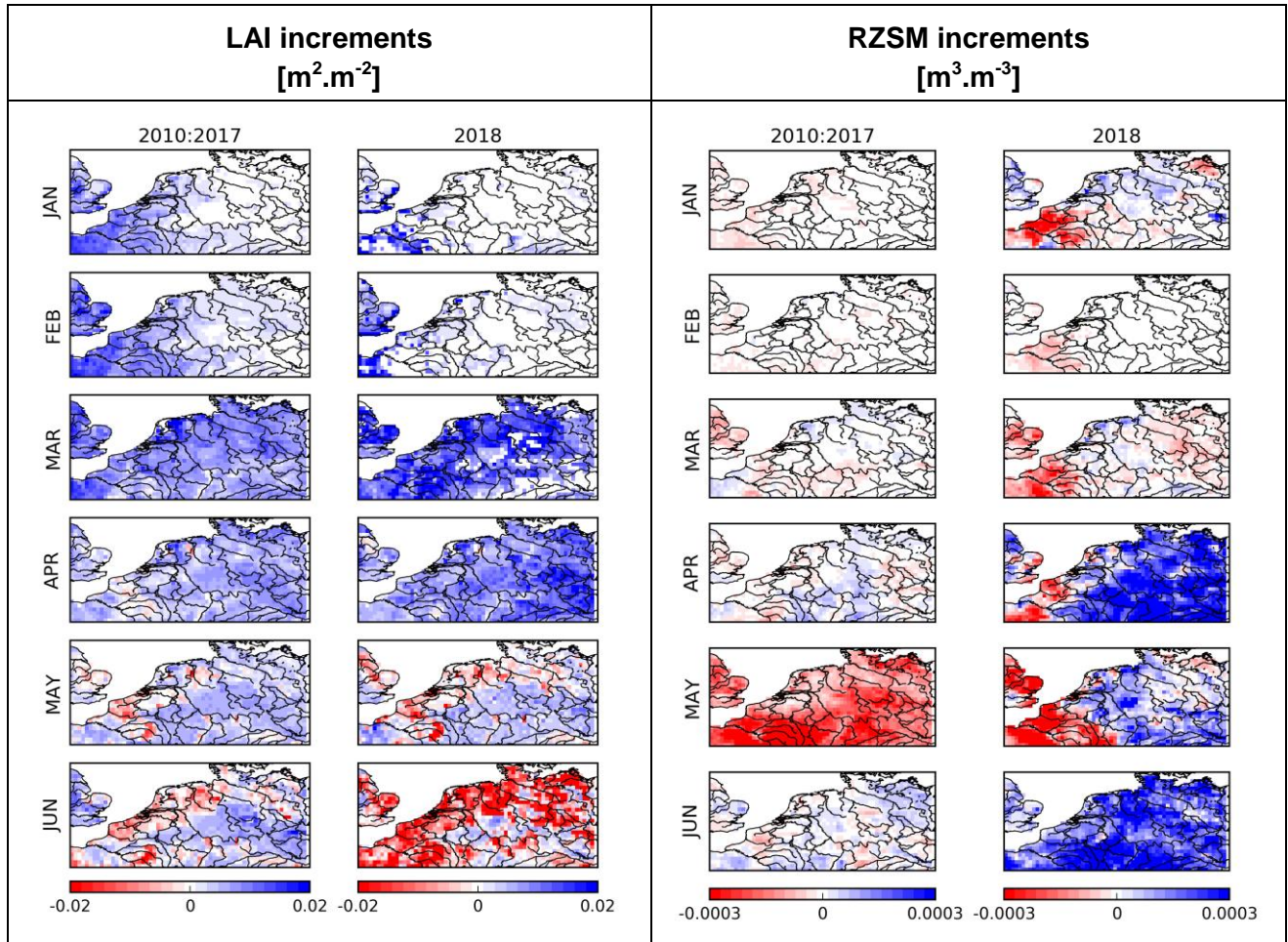


Figure 66: Monthly maps over Western Europe from January to June of LAI (1st column), root-zone soil moisture (2nd column) increments: averages over 2010–2017 (left), and for 2018 (right).

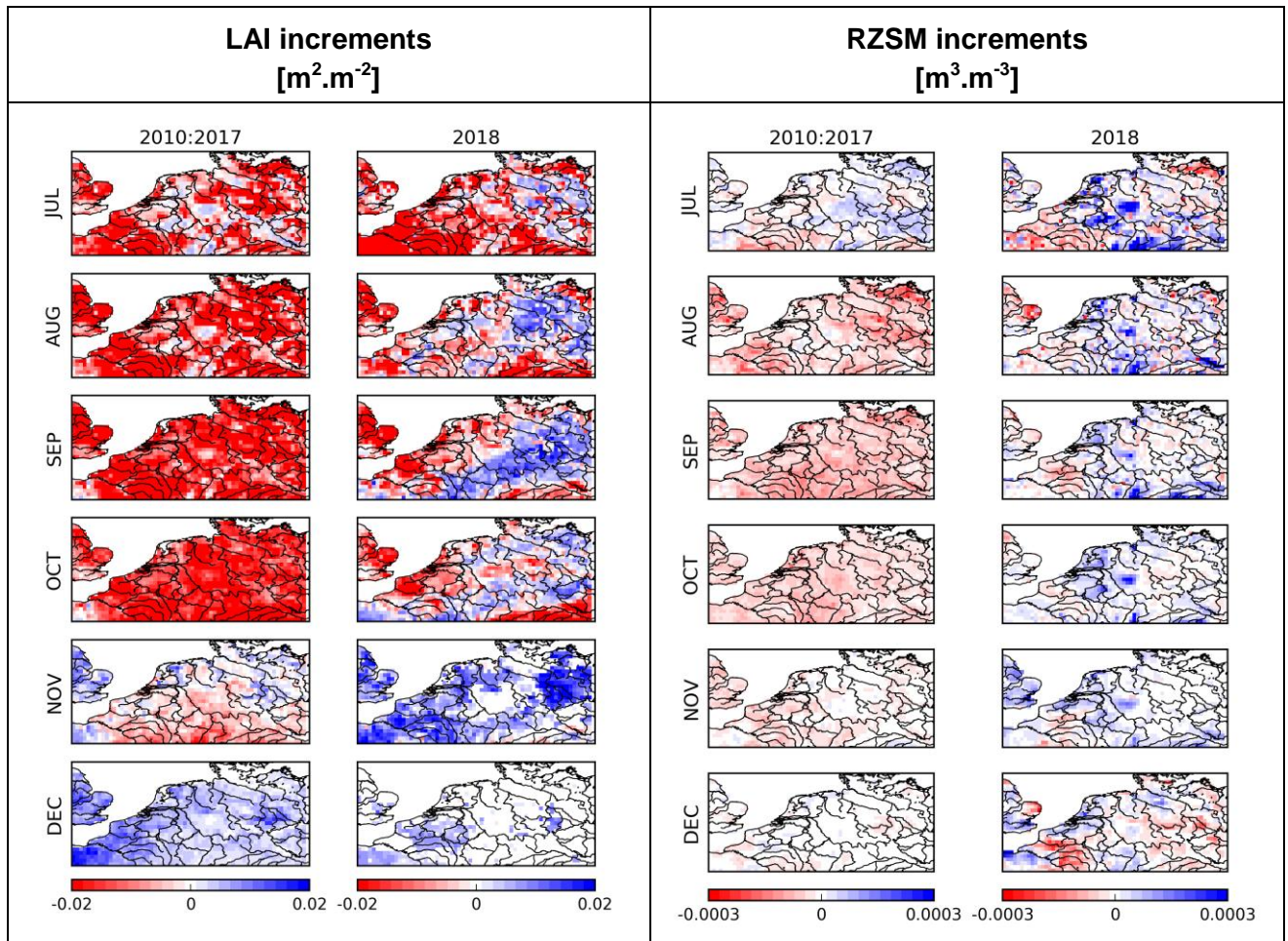


Figure 67: Monthly maps over Western Europe from July to December of LAI (1st column), root-zone soil moisture (2nd column) increments: averages over 2010–2017 (left), and for 2018 (right).

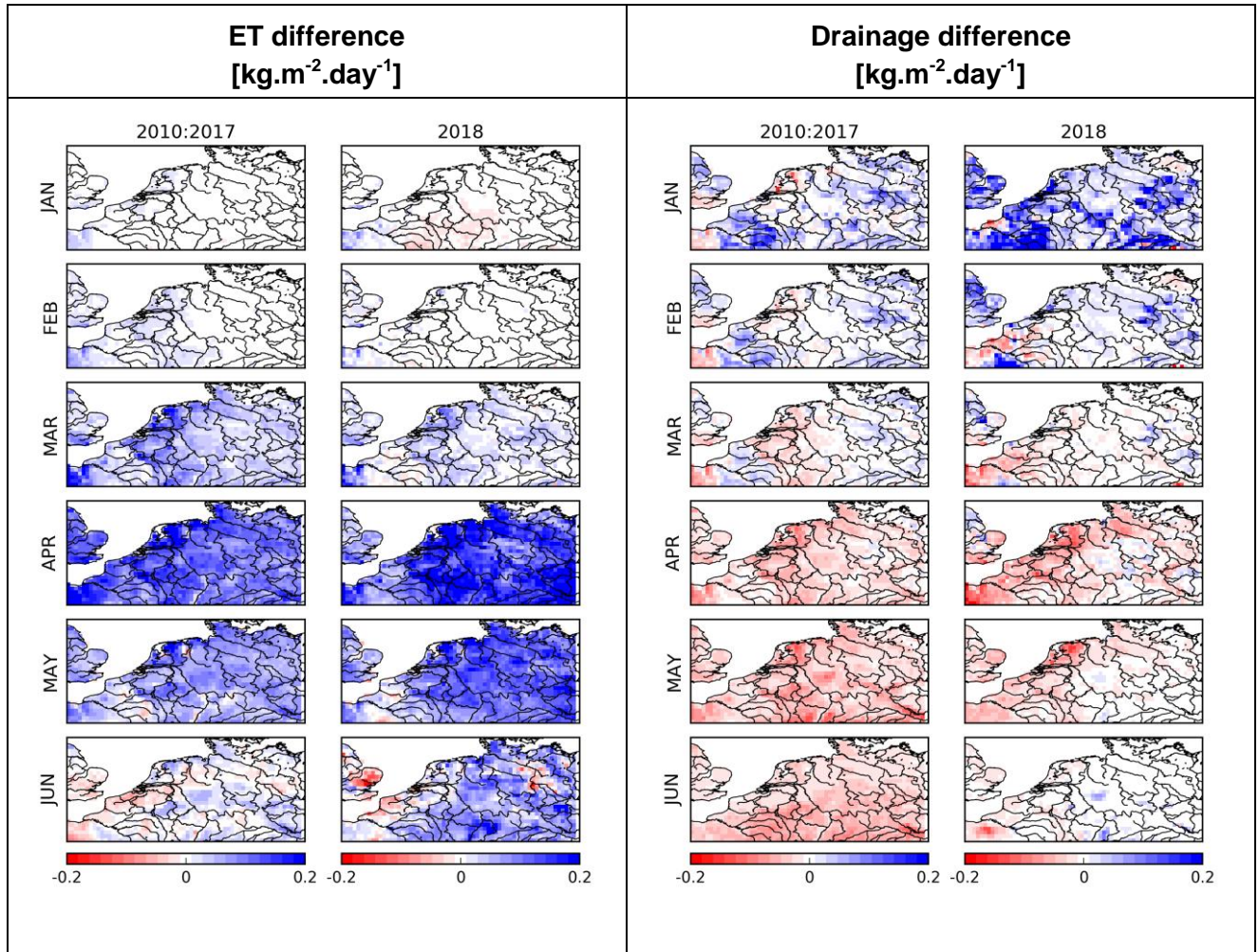


Figure 68: Monthly maps over Western Europe from January to June of the differences (Analysis-Model) for evapotranspiration (ET, 1st column) and drainage fluxes (2nd column): averages over 2010–2017 (left), and for 2018 (right).

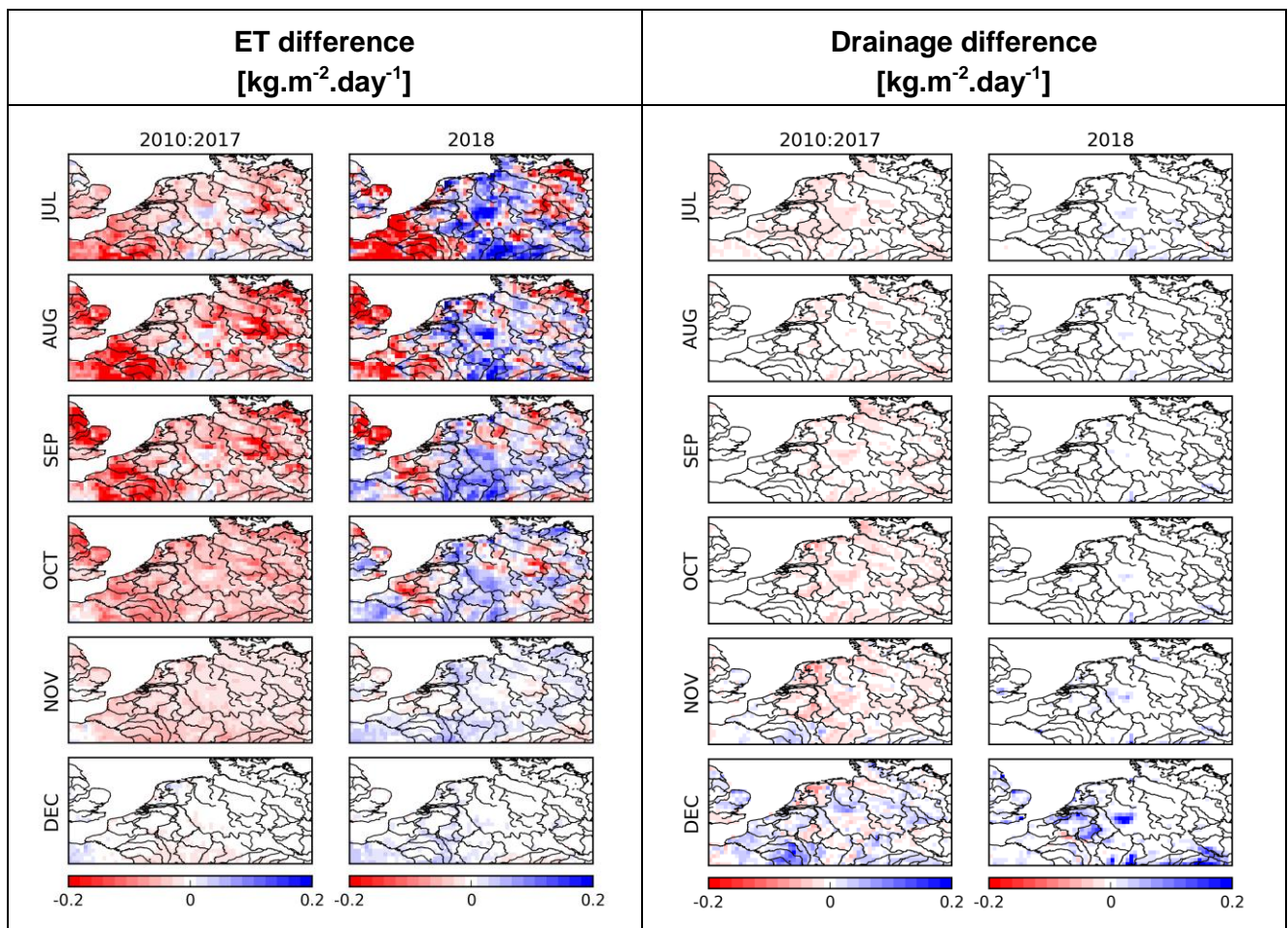


Figure 69: Monthly maps over Western Europe from July to December of the differences (Analysis-Model) for evapotranspiration (ET, 1st column) and drainage fluxes (2nd column): averages over 2010–2017 (left), and for 2018 (right).

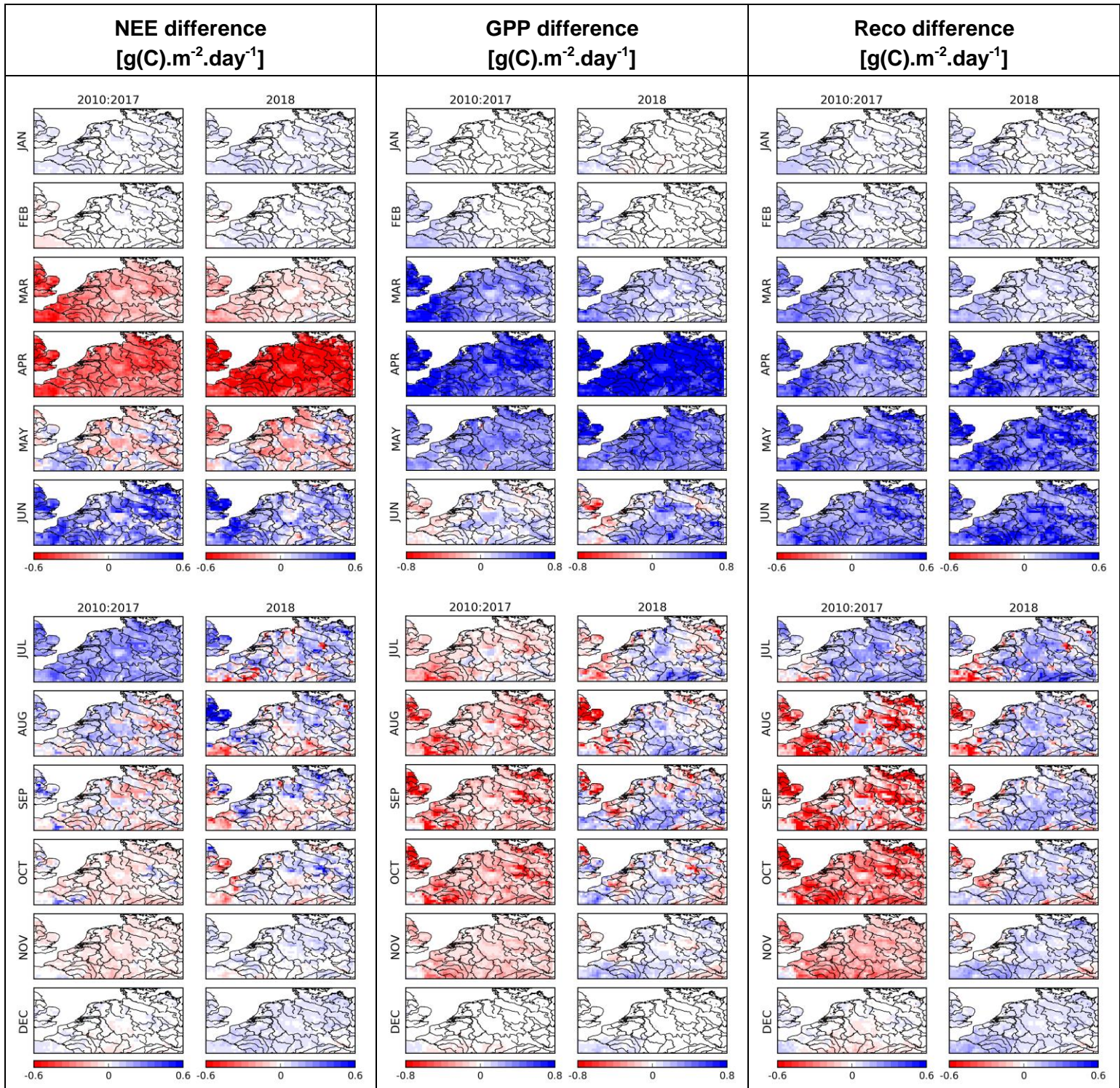


Figure 70: Monthly maps over Western Europe from January to December of the differences (Analysis-Model) for NEE (1st column), GPP (2nd column) and Reco fluxes (3rd column): averages over 2010–2017 (left), and for 2018 (right).

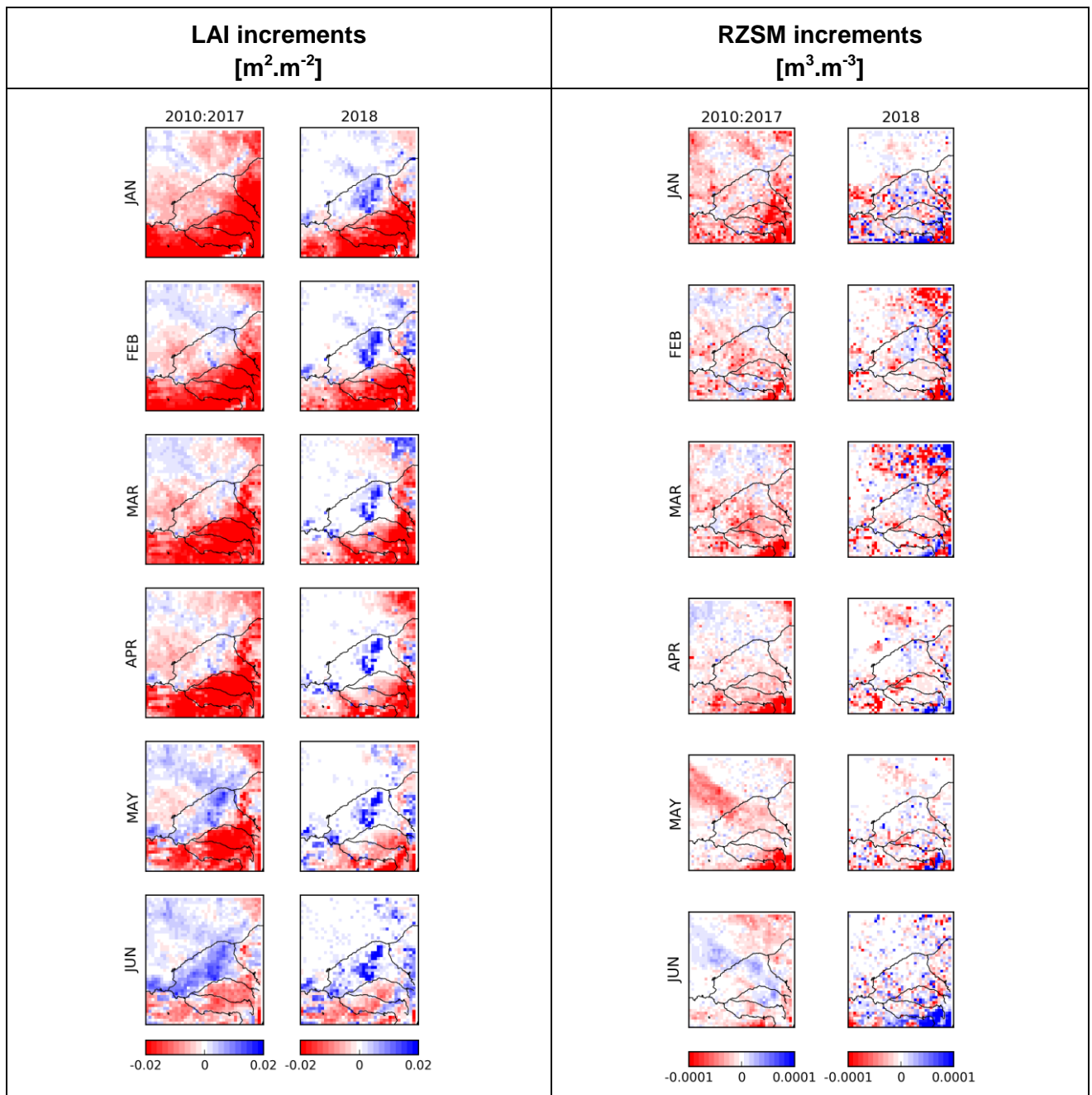


Figure 71: Monthly maps over the Murray-Darling basin from January to June of LAI (1st column), root-zone soil moisture (2nd column) increments: averages over 2010–2017 (left), and for 2018 (right).

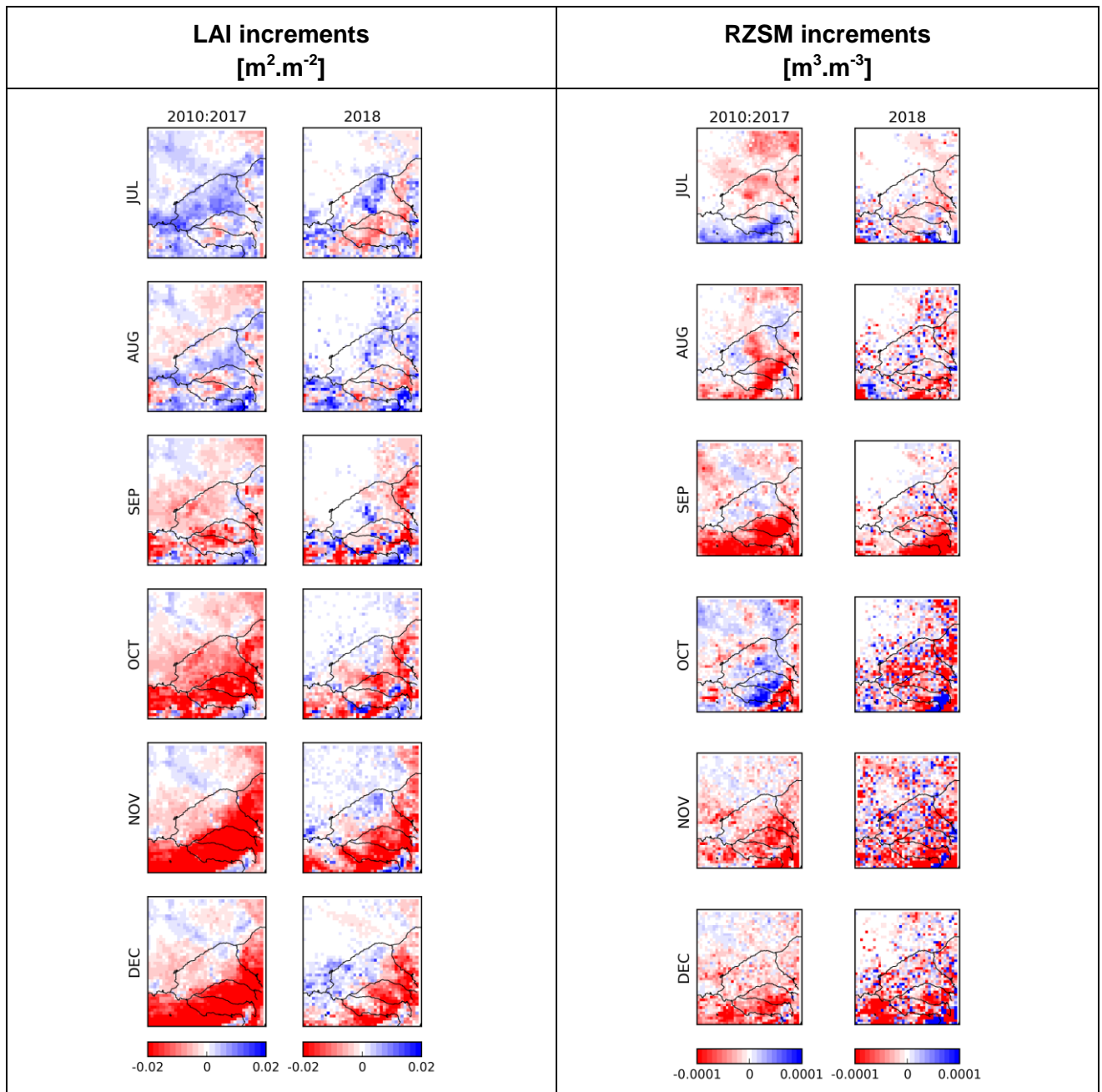


Figure 72: Monthly maps over the Murray-Darling basin from July to December of LAI (1st column), root-zone soil moisture (2nd column) increments: averages over 2010–2017 (left), and for 2018 (right).

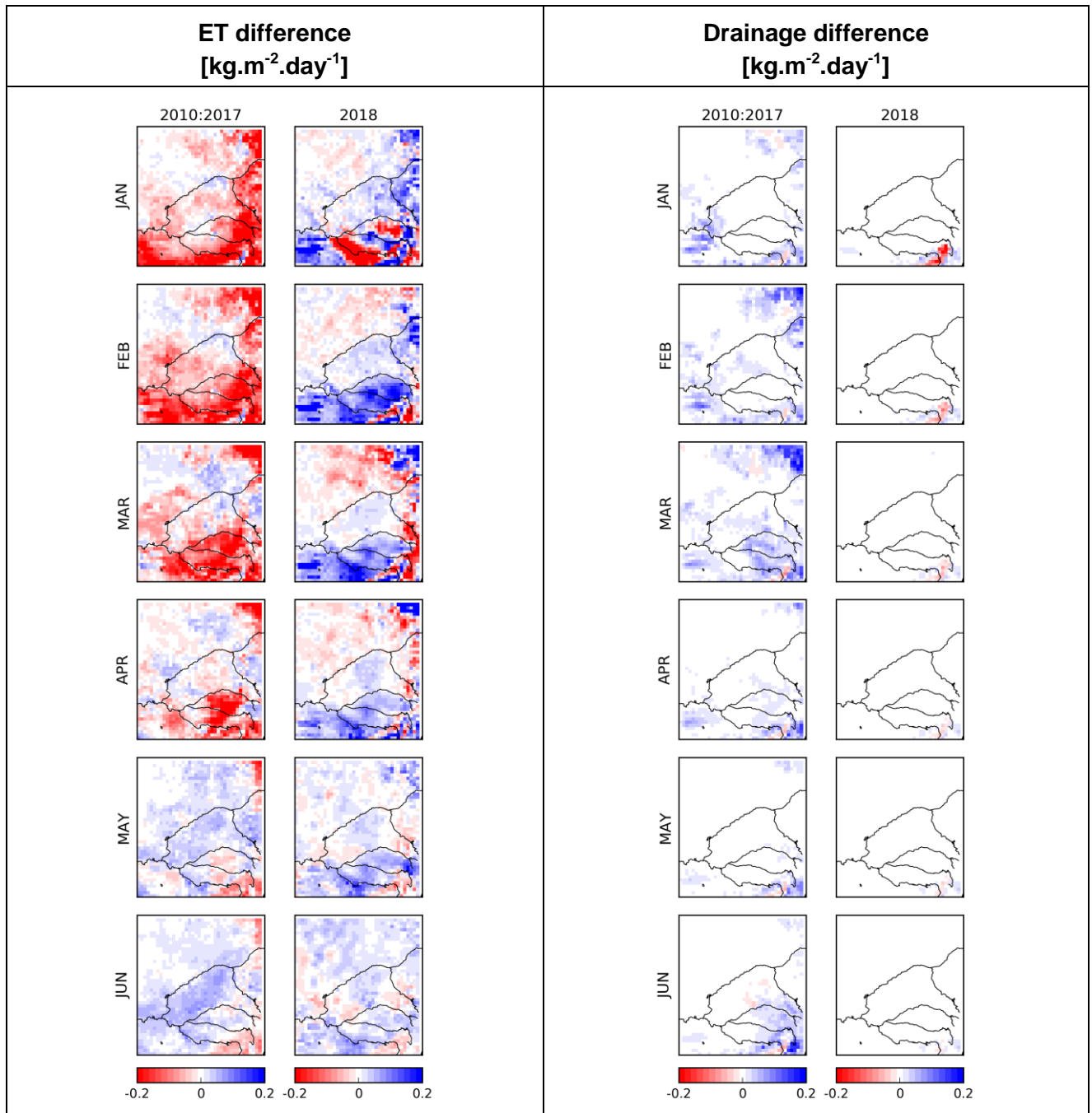


Figure 73: Monthly maps over the Murray-Darling basin from January to June of the differences (Analysis-Model) for evapotranspiration (ET, 1st column) and drainage fluxes (2nd column): averages over 2010–2017 (left), and for 2018 (right).

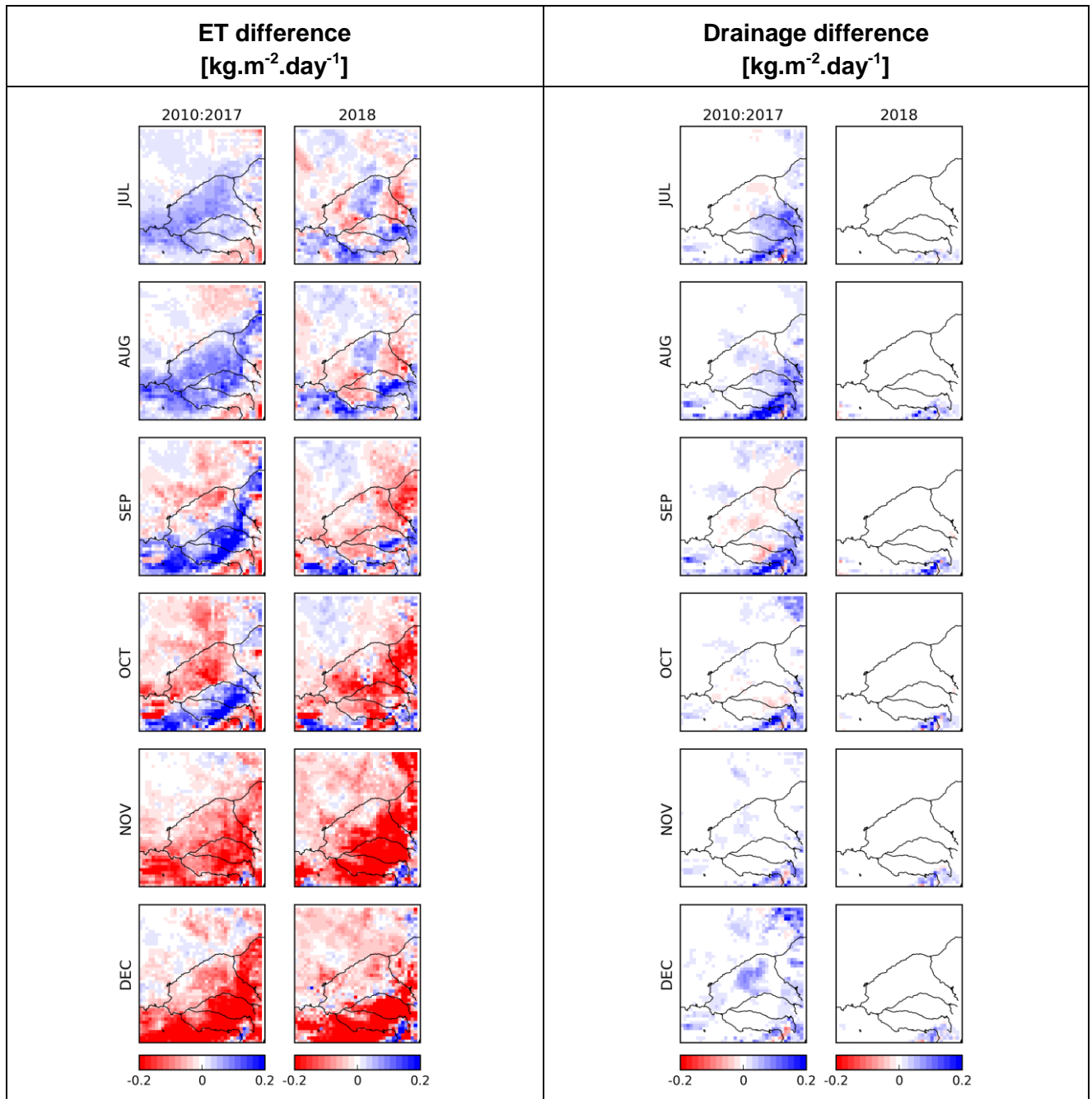


Figure 74: Monthly maps over the Murray-Darling basin from July to December of the differences (Analysis-Model) for evapotranspiration (ET, 1st column) and drainage fluxes (2nd column): averages over 2010–2017 (left), and for 2018 (right).

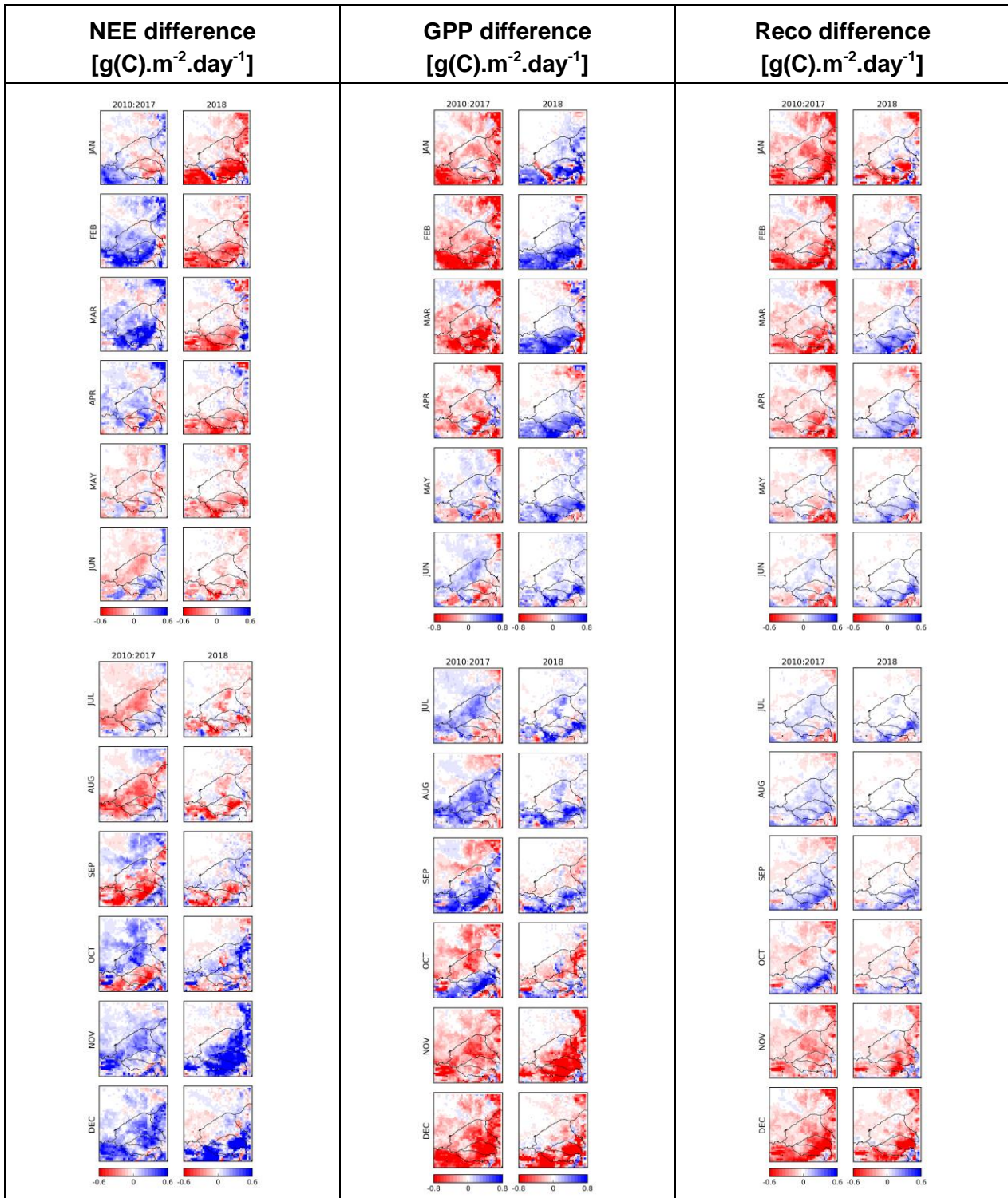


Figure 75: Monthly maps over the Murray-Darling basin from January to December of the differences (Analysis-Model) for NEE (1st column), GPP (2nd column) and Reco fluxes (3rd column): averages over 2010–2017 (left), and for 2018 (right).

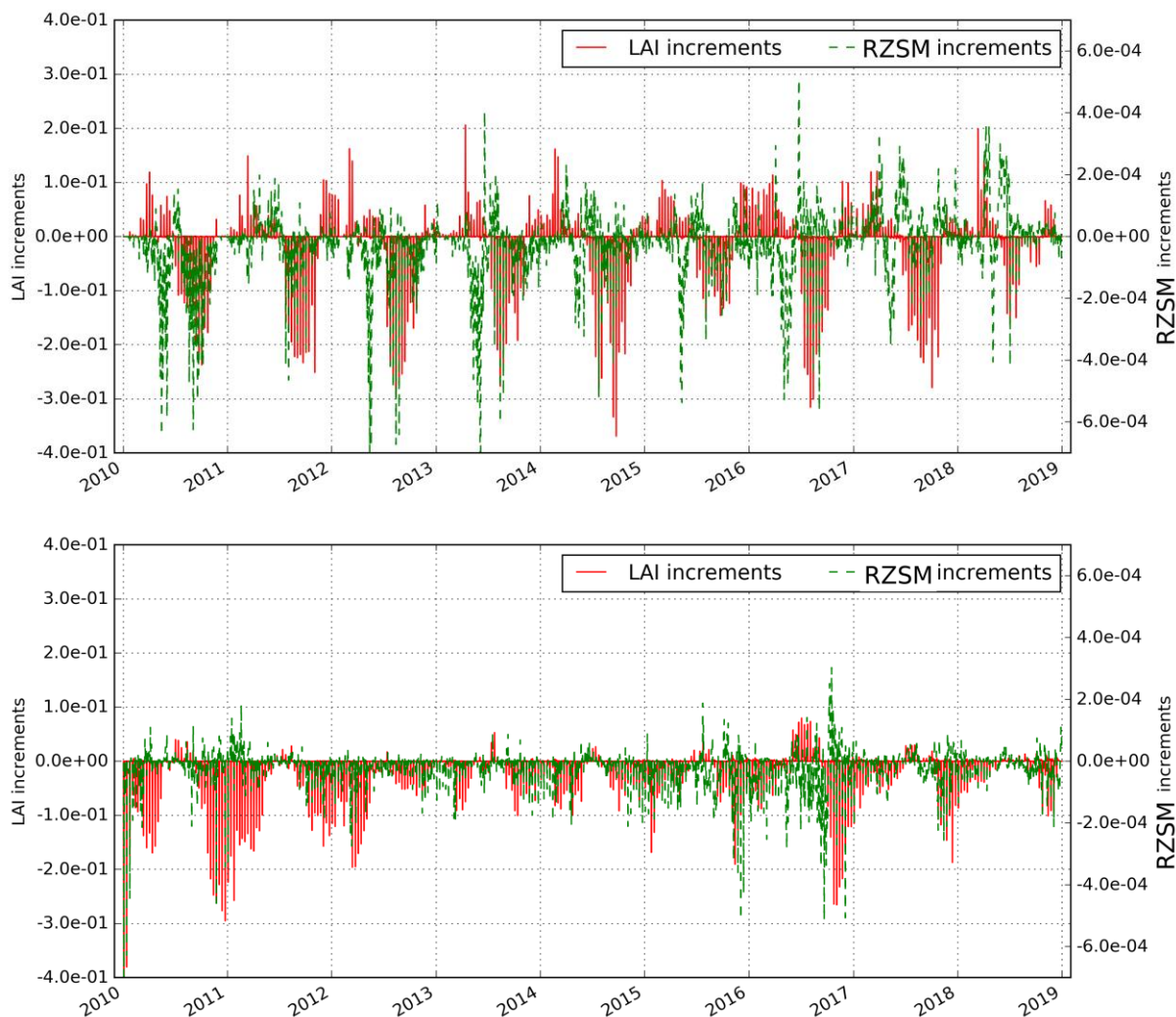


Figure 76: RZSM and LAI mean increments which result from the assimilation of both SWI-001 and LAI observations over Western Europe (top) from 2010 to 2018, over the Murray-Darling basin (bottom) from 2010 to 2018.

Over Western Europe, largest differences caused by the assimilation in 2018 with respect to the 2010-2017 period of time are observed for ET during the heat wave, from August to October: marked positive ET differences are observed over forested areas of western Germany and over the French Vosges (Figure 69). Positive GPP differences are also observed over these areas (Figure 70), in relation to larger analyzed SSM (Figure 27) and to small or positive increments of LAI and RZSM (Figure 67).

Over the Murray-Darling basin, marked positive LAI increments are observed in 2018 close to the Murray river in September and October (Figure 72). These areas correspond to irrigated areas as shown by the irrigation map of the Murray-Darling basin: <http://www.bom.gov.au/water/nwa/2016/mdb/regiondescription/geographicinformation.shtml>. This enhancement of plant growth by integrating observations into the model could be related to irrigation, which is not represented in the model simulations. Overall, the assimilation tends to increase ET in the southern part of the domain in 2018, from February to April (Figure 73), consistent with larger LAI values in Figure 6. The reverse behavior is observed for previous years. In the mountainous areas of the south-east, ET is decreased, mainly in March, consistent with the smaller LAI in Figure 6. The impact of the assimilation on drainage is smaller in 2018 than for previous years because very dry conditions prevailed in 2018 and drainage is small in dry conditions. The same contrasting patterns in 2018 as for ET are observed for carbon fluxes (Figure 75).

Overall, Figure 76 shows that LAI and RZSM increments are rather small with respect to previous years for both Western Europe and Murray-Darling basin.

Over the Murray-Darling basin, RZSM increments (either positive or negative values) after July 2015 are more pronounced than from 2010 to July 2015 (Figure 76). This coincides with the very large increase in the number of ASCAT observations used in the SWI algorithm, related to the use of METOP-B data in addition to METOP-A data. Over this area, the number of observations used in the SWI can be multiplied by a factor of 3 or more (Figure 86). Such a very large change in the observational framework impacts the LDAS pre-processing phase. In particular, the CDF-matching step may be affected by statistical uncertainties as this step is performed before the arrival of METOP-B data.

9.2 TRANSITION BETWEEN SPOT-VGT AND PROBA-V

The impact on analyzed LAI of transitioning from SPOT-VGT to PROBA-V is rather small (Figure 77). However, PROBA-V scores are nearly systematically better than those for SPOT-VGT over the Murray-Darling basin from January to May.

For SA (Figure 78), a very large increase in bias is observed for PROBA-V, of about 0.02 and 0.04 for Western Europe and for the Murray-Darling basin, respectively. All scores for SA can differ during the period when snow can affect SA over Western Europe, from

December to March. These discrepancies could be caused by differences in snow occurrence during the SPOT-VGT and PROBA-V periods rather than by differences in sensors. Over the Murray-Darling basin, the SA SDD and correlation scores are nearly systematically better for PROBA-V.

It must be noticed that changes in LAI and SA scores over the Murray-Darling basin could also be influenced by the marked trend in LAI and SA from 2010 to 2018 (Figure 9 and Figure 23, respectively).

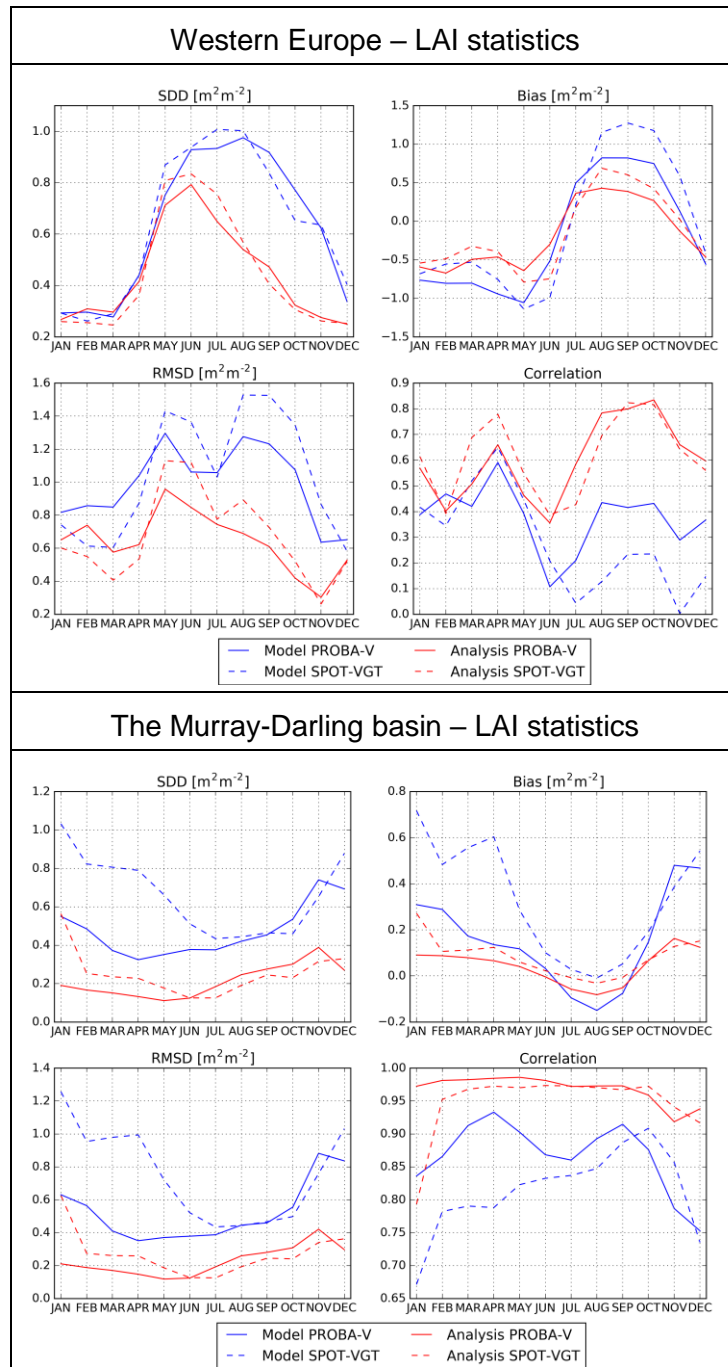


Figure 77: LAI scores for the time periods of SPOT-VGT observations over Western Europe (top) (2010-2013, dashed lines) and the Murray-Darling basin (bottom) (2010-2013, dashed lines) and of PROBA-V observations (2015-2018, solid lines). Model performances are in blue and analysis performances are in red w.r.t. the appropriate observations. [NB: 2014 was not considered since it was the year of transition between the two instruments].

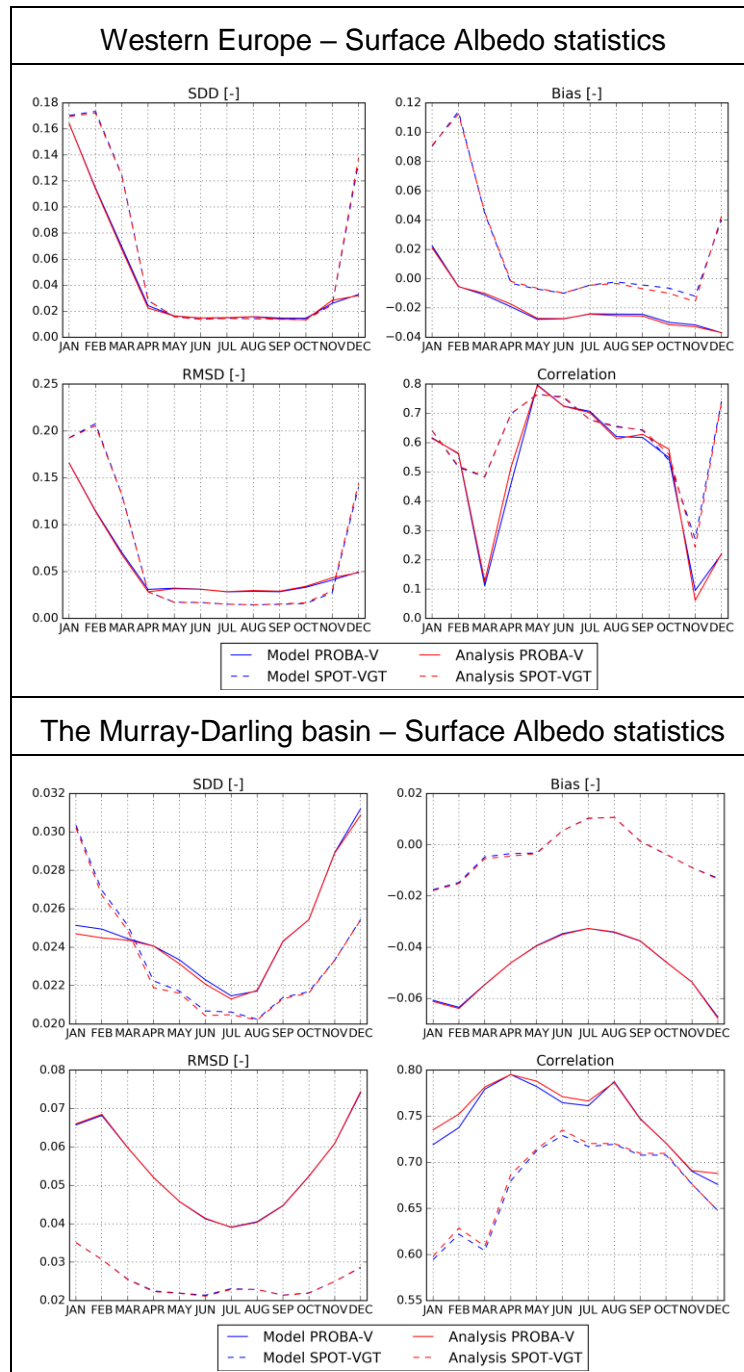


Figure 78: SA scores for the time periods of SPOT-VGT observations over Western Europe (top) (2010-2013, dashed lines) and the Murray-Darling basin (bottom) (2010-2013, dashed lines) and of PROBA-V observations (2015-2018, solid lines). Model performances are in blue and analysis performances are in red w.r.t. the appropriate observations. [NB: 2014 was not considered since it was the year of transition between the two instruments].

9.3 LAI VERSION 1 (GEOV1) vs. LAI VERSION 2 (GEOV2)

A comparison between the GEOV2-RT6 and the GEOV1 NRT 1km x 1km LAI products was performed. The GEOV2-RT6 is a final consolidated as created by the LAI algorithm version 2 [CGLOPS1_ATBD_LAI1km-V2]. On the other hand, GEOV1 corresponds to the version 1 of algorithm, produced in NRT [GIOGL1_ATBD_LAI1km-V1]. Over Western Europe (Figure 79) the GEOV2 and GEOV1 RMSD scores are very similar in 2018, for both model and analysis simulations. These scores in 2018 are better than for previous years. For previous years, the GEOV1 RMSD presents better values than the GEOV2 RMSD.

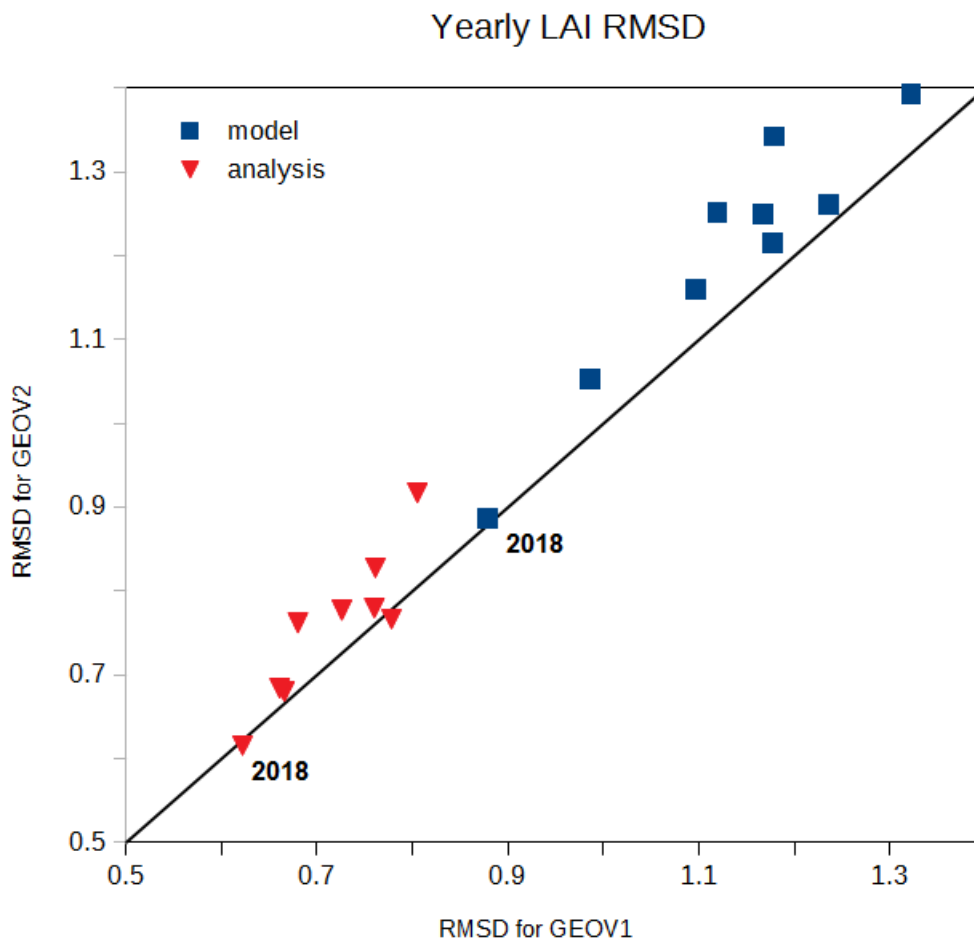


Figure 79: LAI GEOV2 vs. GEOV1 yearly RMSD score over Western Europe for each year from 2010 to 2018. Year 2018 is indicated.

Similar results are found over the Murray-Darling basin (Figure 80) but, contrary to Western Europe, GEOV1 and GEOV2 RMSD scores are very close for all years, not only for 2018.

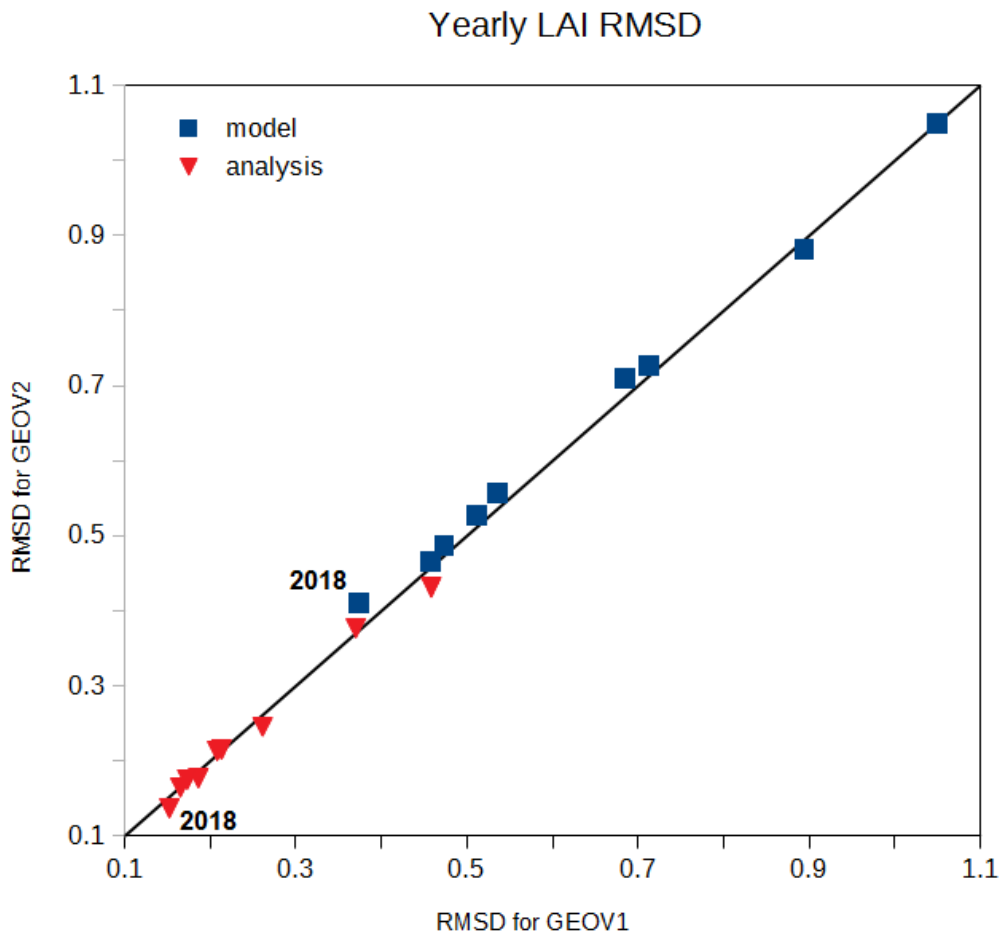


Figure 80: LAI GEOV2 vs. GEOV1 yearly RMSD score over the Murray-Darling basin for each year from 2010 to 2018. Year 2018 is indicated.

9.4 ACCURACY ASSESSMENT

Using LDAS analysis simulations, it is possible to assess the accuracy of the observations by computing the RMSD and the relative RMSD and compare them to the user requirements of the products (e.g. GCOS accuracy requirements, based on RMSD). This was made for LAI and FAPAR over Western Europe (Figure 81) and over the Murray-Darling basin (Figure 82). If the analysis simulation is considered as the “truth”, or at least the “reference”, RMSD between the observations and the analysis values can be used as an indicator of the observations accuracy. GCOS requirements are defined as (see GCOS document N°154, December 2011, on https://library.wmo.int/opac/doc_num.php?explnum_id=3710):

- LAI accuracy: max (20%,0.5)
- FAPAR accuracy: max (10%,0.05)

RMSD or relative RMSD values lower than the GCOS accuracy thresholds indicate that GCOS accuracy requirements are met. However, higher values do not mean that GCOS accuracy requirements are not met as RMSD incorporates model errors in addition to satellite product errors. In this case, one could consider that GCOS requirements may not be made.

RMSD values are considered for low LAI and FAPAR values (≤ 2.5 and ≤ 0.5 , respectively).

Relative RMSD values are considered for high LAI and FAPAR values (> 2.5 and > 0.5 , respectively).

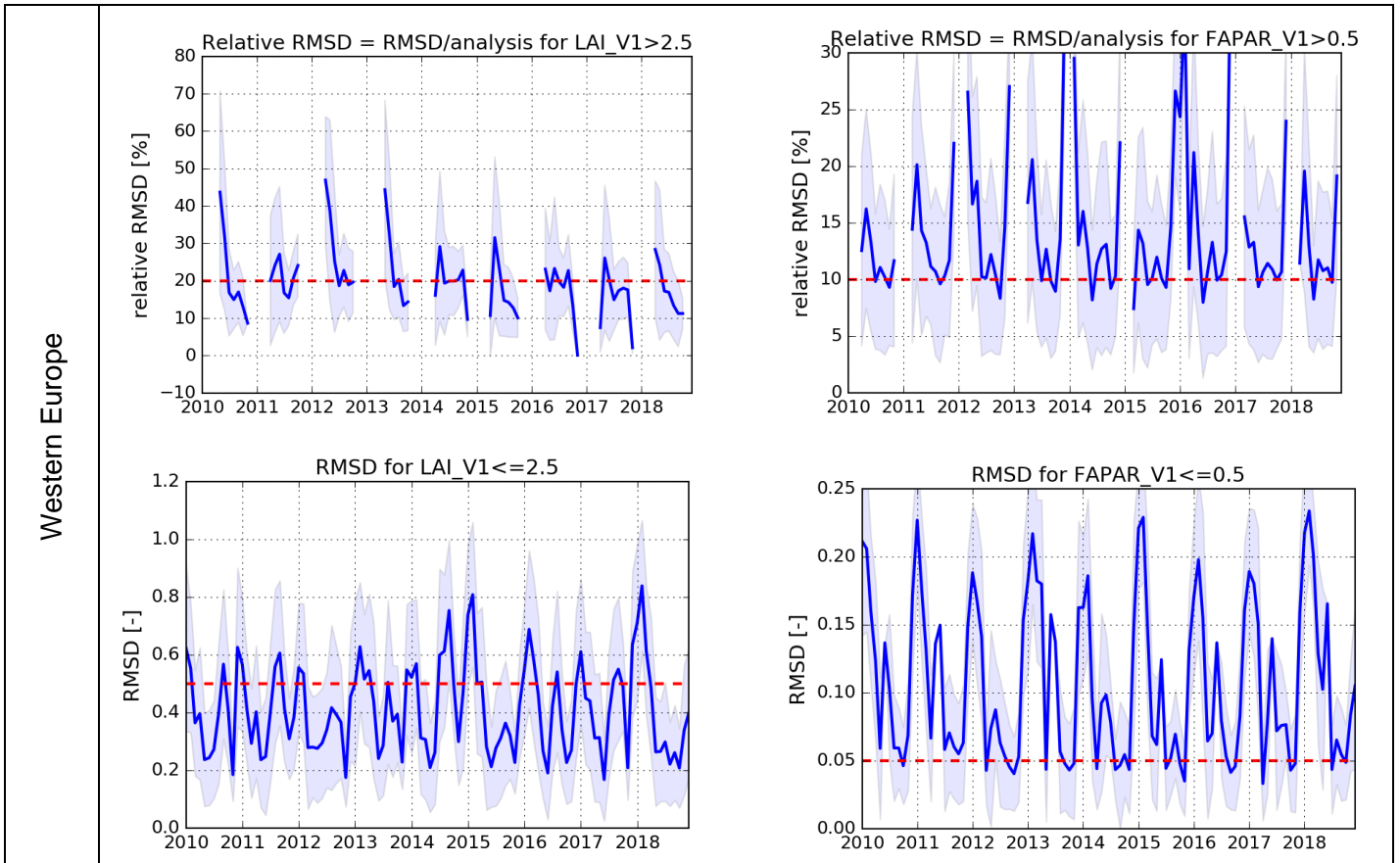


Figure 81: Relative analysis RMSD (RMSD divided by value) (top) and analysis RMSD (bottom) of LAI (left) and FAPAR (right) on average over Western Europe. Dashed red line indicates the target accuracies: max(20%,0.5) for LAI and max(10%,0.05) for FAPAR. Shaded areas indicate 1 standard deviation.

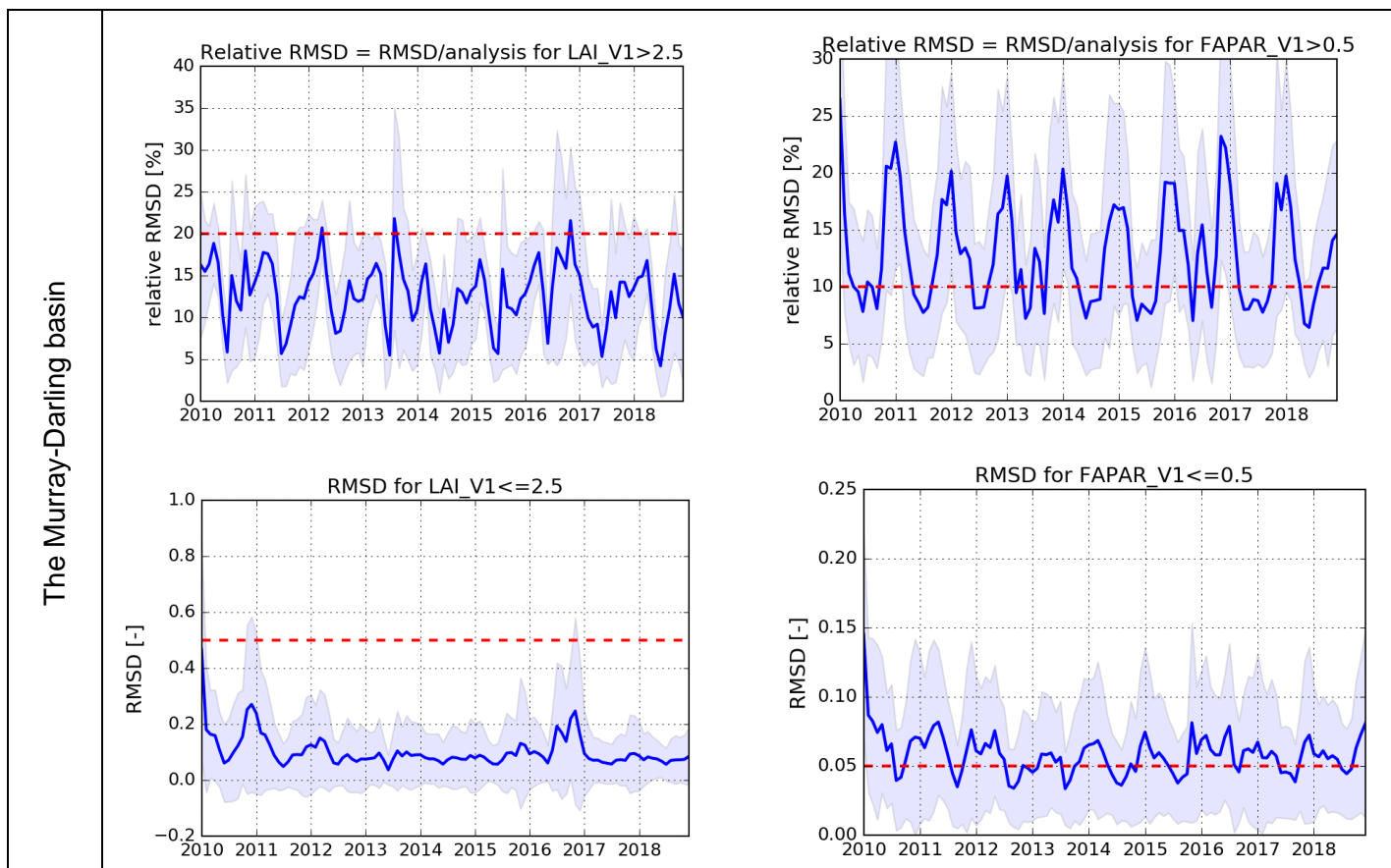


Figure 82: Relative analysis RMSD (RMSD divided by value) (top) and analysis RMSD (bottom) of LAI (left) and FAPAR (right) on average over the Murray-Darling basin. Dashed red line indicates the target accuracies: max(20%,0.5) for LAI and max(10%,0.05) for FAPAR. Shaded areas indicate 1 standard deviation.

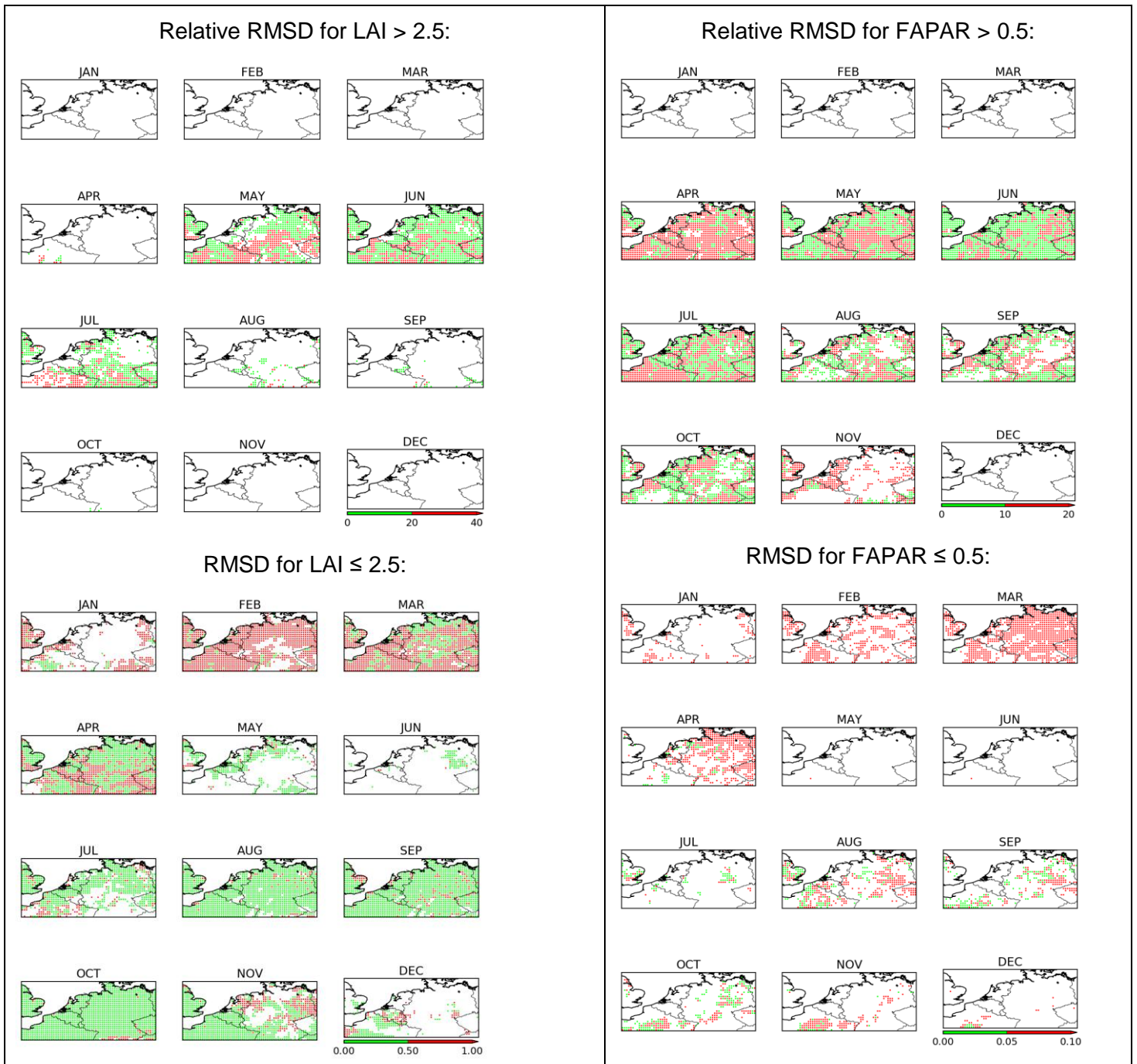


Figure 83: Maps over Western Europe showing (in green) where GCOS accuracy requirements could be met (LAI: max(20%,0.5), FAPAR: max(10%,0.05)) or may have not be met (in red) for 2018.

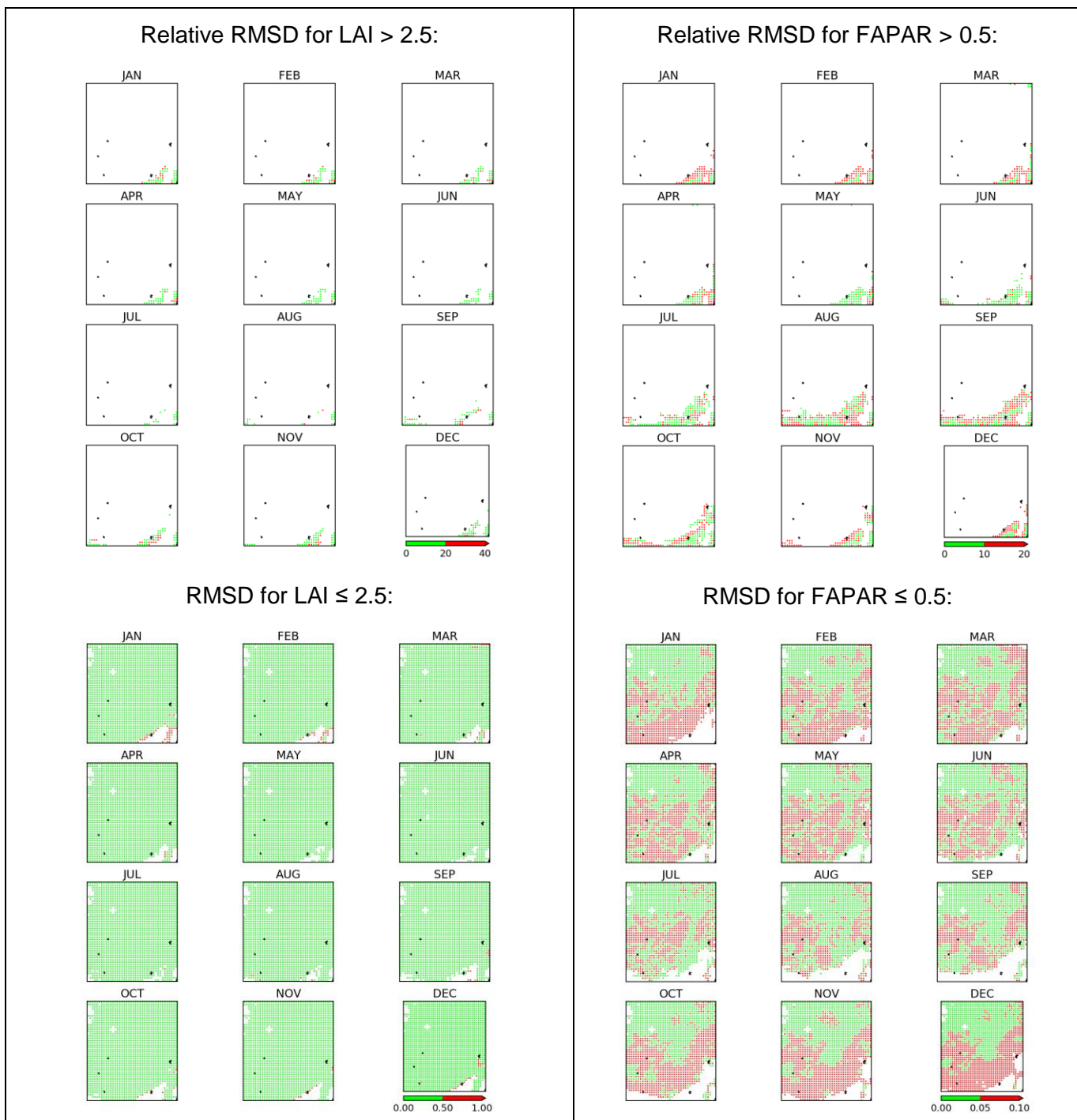


Figure 84: Maps over the Murray-Darling basin showing (in green) where GCOS accuracy requirements could be met (LAI: max(20%,0.5), FAPAR: max(10%,0.05)) or may have not be met (in red) for 2018.

On Figure 83, maps of LAI and FAPAR accuracy for 2018 show that accuracy of high values of LAI is similar to the accuracy of high values of FAPAR in May and June over Western Europe. For low product values, the GCOS accuracy criterion is met much more often for LAI than for FAPAR. The latter finding is further illustrated in Figure 81: while the mean RMSD for $LAI \leq 2.5$ is nearly always smaller than 0.5, the mean RMSD for $FAPAR \leq 0.5$ is nearly always larger than 0.5.

Over the Murray-Darling basin, Figures 82 and 84 shows that low LAI values are generally more accurate than low FAPAR values, consistent with what is observed over Western Europe. The highest LAI and FAPAR values are observed in September-October (Figure 4 and Figure 14, respectively). Figure 84 shows that fractional areas of accurate high LAI and FAPAR values are more or less equivalent over the Murray-Darling basin as a whole. However, Figure 82 shows that the mean LAI relative RMSD is often smaller than the 20% threshold. This is not the case for high FAPAR values, with mean relative RMSD values often larger than 10%.

9.5 NUMBER OF OBSERVATIONS

The following maps show the number of dates per year when observations are available for assimilation for the SWI-001 product only. Until 20 July 2015, only METOP-A observations were available. Now both METOP-A and METOP-B are operating and more observations are available. This difference in the number of available observations can introduce some errors in the interpretation of the statistics because they might not be representative of the same area. Over Western Europe (Figure 85), it should not have a big impact because all the region is uniformly covered twice more. However, over the Murray-Darling basin (Figure 86), some parts are covered more than twice, especially at the eastern part of the domain, where areas were completely missing before 2015. More weight being now given to areas where the CDF-matching was based on relatively few data, we recommend to interpret the LDAS statistics (section 9.1) with caution.

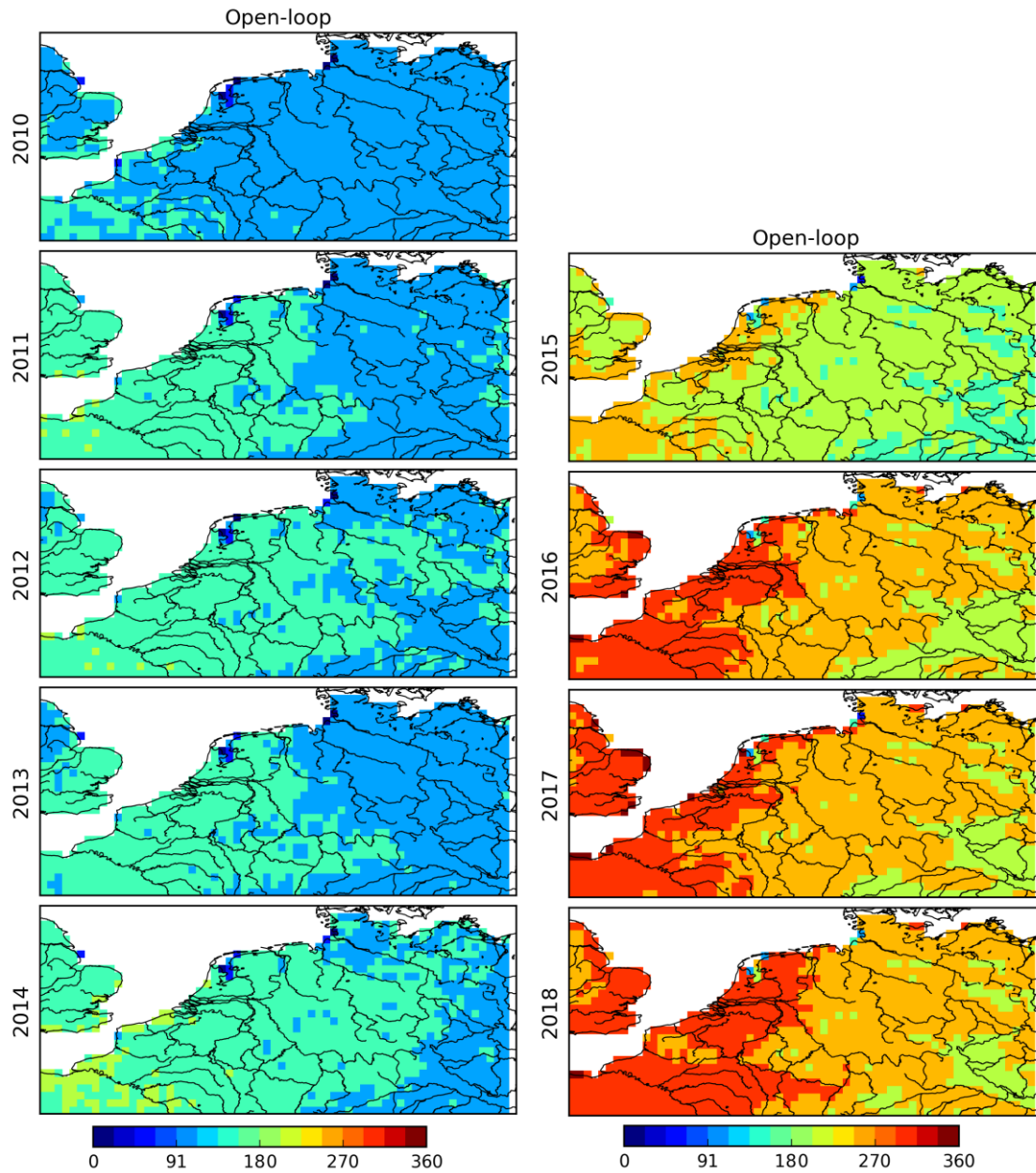


Figure 85: Annual number of SWI-001 observations available over Western Europe (only METOP-A until July 20, 2015; after July 21, 2015 both METOP-A and B are used)

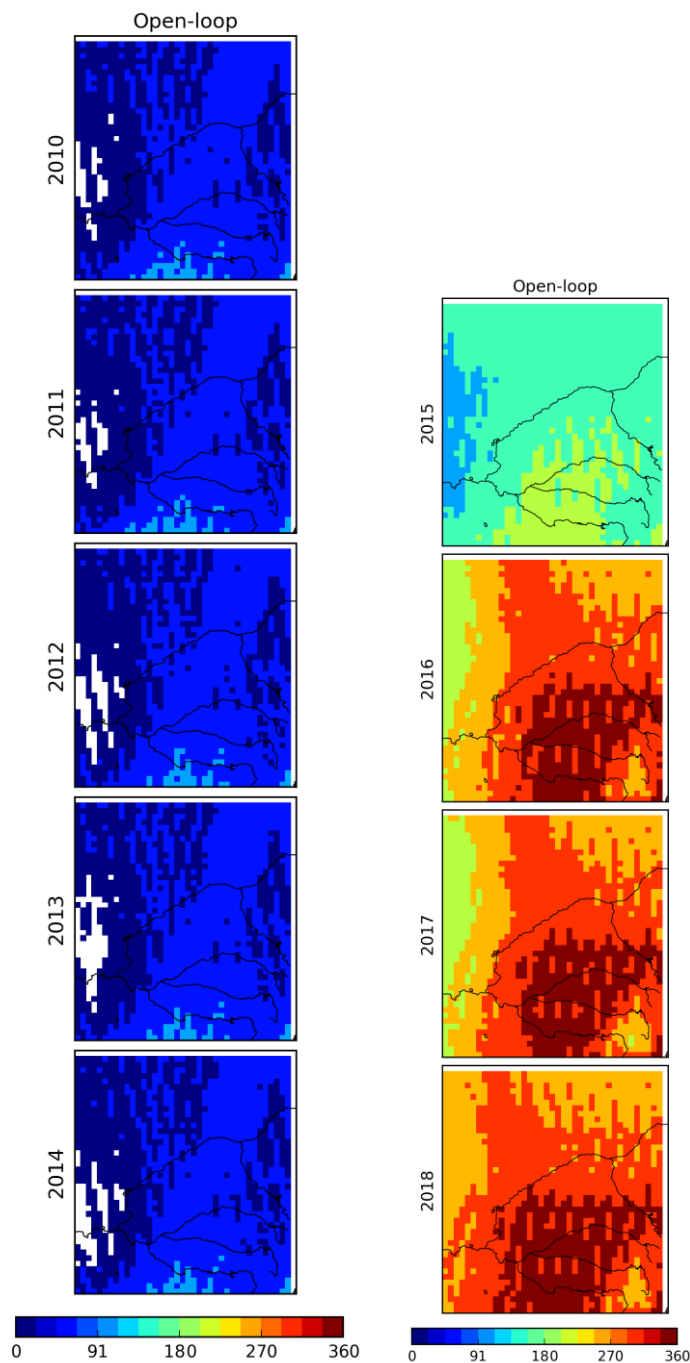


Figure 86: Annual number of SWI-001 observations available over the Murray-Darling basin (only METOP-A until July 20, 2015; after July 21, 2015 both METOP-A and B are used)

10 CONCLUSIONS

This document summarizes the results of the cross-cutting quality monitoring of the Copernicus Global Land Service for the period from 1st January 2018 to 31th December 2018. The SA product derived from PROBA-V data was available for the first time and was included in this annual report. Both LAI and SWI-001 products were integrated into the ISBA-A-gs LSM using a LDAS platform over Western Europe and over the Murray-Darling basin. An extensive analysis of the LAI, FAPAR, SA, SWI-001, and LST products was performed. Scores were obtained monthly (Figure 10, Figure 11, Figure 17, Figure 18, Figure 24, Figure 25, Figure 38, Figure 39, Figure 58, Figure 59, Figure 60, Figure 61) for 2018 and for previous years (the period from 2010 to 2017).

For **LAI**, over both Western Europe and the Murray-Darling basin, the scores tend to present better values during the dry spells of 2018 than during previous years from 2010 to 2017. The RMSD scores of GEOV2-RT6 and GEOV1 are comparable in 2018. The impact on analyzed LAI of transitioning from SPOT-VGT to PROBA-V is small. Over Western Europe, the seasonality of the LAI bias is caused by a delayed peak LAI date in the model simulations, and GEOV2-RT6 tends to present larger RMSD values than GEOV1 from 2010 to 2017.

For **FAPAR**, over both Western Europe and the Murray-Darling basin, the scores tend to present slightly better values during the dry spells of 2018 than during previous years from 2010 to 2017. The largest values of analyzed FAPAR RMSD and bias are observed at wintertime over Western Europe. Being a radiation variable, low winter FAPAR is quite sensitive to illumination conditions and to soil directional assumptions at mid-latitudes (Claverie et al., 2013).

For **SA**, a striking result is that a very large increase in the mean bias value is observed after the transition from SPOT-VGT to PROBA-V, of about 0.02 and 0.04 for Western Europe and for the Murray-Darling basin, respectively. There is a clear discontinuity in the SA time series, not observed for LAI nor for FAPAR. Contrary to LAI and FAPAR, the SA scores in 2018 do not always present better values than during the 2010-2017 reference period of time. Finally, the number of available observations is smaller than for LAI and FAPAR.

For **SWI-001**, the impact of the seasonal SSM CDF-matching performed prior the assimilation is particularly striking for Western Europe. Without a seasonal CDF-matching, the original SSM information would be misleading over Western Europe. Contrary to LAI and FAPAR products SSM scores in 2018 do not present significantly better values than for previous years from 2010 to 2017 and the analyzed SSM does not present a reinforcement of the drought signal over Western Europe with respect to the modelled SSM.

For **LST**, the model tends to underestimate LST at daytime and to overestimate LST at dawn. The mean monthly cold bias observed at noon is particularly large (down to -11°C) at summertime over the Murray-Darling basin in 2018. Over the Murray-Darling basin, the mean yearly bias is about -8°C in 2018 (a dry year), against -4°C in 2010 (a wet year). This result shows that daytime LST biases are more pronounced in dry conditions. Possible causes of the spatial, diurnal and seasonal patterns of the LST bias are hot-spot phenomenon (more sunlit than shaded elements are seen by the satellite), biases in the incoming solar and infrared radiation data used to force the model. When the assimilation significantly reduces the simulated LAI, the LST noon bias is slightly reduced in the analysis, for both Western Europe and the Murray-Darling basin. Also, the assimilation tends to improve the temporal correlation of the simulated and observed LST. This shows the consistency of the observed LST with the observed LAI.

LDAS analyses were also used to assess the accuracy of LAI and FAPAR observations, with respect to GCOS requirements. Using the analysis RMSD score as a proxy to assess the LAI and FAPAR products accuracies, it is showed that small values of LAI observations tend to meet the GCOS requirements more often than large values of LAI observations and of FAPAR observations, for both Western Europe and the Murray-Darling basin. Overall, low FAPAR values present more uncertainties than low LAI values.

11 REFERENCES

Albergel, C., S. Munier, D. J. Leroux, H. Dewaele, D. Fairbairn, A. L. Barbu, E. Gelati, W. Dorigo, S. Faroux, C. Meurey, P. Le Moigne, B. Decharme, J.-F. Mahfouf, J.-C. Calvet: Sequential assimilation of satellite-derived vegetation and soil moisture products using SURFEX_v8.0: LDAS-Monde assessment over the Euro-Mediterranean area, *Geosci. Model Dev.*, *Geosci. Model Dev.*, 10, 3889–3912, <https://doi.org/10.5194/gmd-10-3889-2017>, 2017.

Barbu, A., J.-C. Calvet, J.-F. Mahfouf, C. Albergel, S. Lafont, “Assimilation of soil wetness Index and Leaf Area Index into the ISBA-A-gs land surface model: grassland case study”, *Biogeosciences*, 8, 1971-1986, <https://doi.org/10.5194/bg-8-1971-2011>, 2011.

Barbu, A.L., J.-C. Calvet, J.-F. Mahfouf, and S. Lafont: Integrating ASCAT surface soil moisture and GEOV1 leaf area index into the SURFEX modelling platform: a land data assimilation application over Western Europe, *Hydrol. Earth Syst.*, 18, 173–192, <https://doi.org/10.5194/hess-18-173-2014>, 2014.

Carrer D., J.-L. Roujean, S. Lafont, J.-C. Calvet, A. Boone, B. Decharme, C. Delire, and J.-P. Gastellu-Etchegorry: A canopy radiative transfer scheme with explicit FAPAR for the interactive vegetation model ISBA-A-gs: impact on carbon fluxes, *J. Geophys. Res. Biogeosci.*, 118, <https://doi.org/10.1002/jgrg.20070>, 2013.

Carrer D., C. Meurey, X. Ceamanos, J.-L. Roujean, J.-C. Calvet, and S. Liu: Dynamic mapping of snow-free vegetation and bare soil albedos at global 1 km scale from 10-year analysis of MODIS satellite products, *Remote Sens. Environ.*, 140, 420-432, <https://doi.org/10.1016/j.rse.2013.08.041>, 2014.

Claverie M., E. F. Vermote, M. Weiss, F. Baret, O. Hagolle, and V. Demarez: Validation of coarse spatial resolution LAI and FAPAR time series over cropland in southwest Western Europe, *Remote Sens. Environ.*, 139, 216-230, <https://doi.org/10.1016/j.rse.2013.07.027>, 2013.

Ermida, S. L., Trigo, I. F., DaCamara, C. C., and Pires, A. C.: A methodology to simulate LST directional effects based on parametric models and landscape properties, *Remote Sens.*, 10, 1114, <https://www.doi.org/10.3390/rs10071114>, 2018.

Faroux, S., A. T. Kaptué Tchuenté, J.-L. Roujean, V. Masson, E. Martin, and P. Le Moigne: ECOCLIMAP-II/Europe: a twofold database of ecosystems and surface parameters at 1 km resolution based on satellite information for use in land surface, meteorological and climate models, *Geosci. Model Dev.*, 6, 563–582, <https://doi.org/10.5194/gmd-6-563-2013>, 2013.

Hersbach H. and D. Dee: “ERA-5 reanalysis is in production”. ECMWF newsletter, number 147, Spring 2016, p.7, 2016

(<https://www.ecmwf.int/sites/default/files/elibrary/2016/16299-newsletter-no147-spring-2016.pdf>).

Urraca, R., T. Huld, A. Gracia-Amillo, F.J. Martinez-de-Pison, F. Kaspar, and A. Sanz-Garcia : Evaluation of global horizontal irradiance estimates from ERA5 and COSMO-REA6 reanalyses using ground and satellite-based data, Sol. Energy, 164, 339-354, <https://doi.org/10.1016/j.solener.2018.02.059>, 2018.